Fall 12-22-2010

Field Effect and Magnetically Induced Capacitive Tuning in Hole Doped La1-xSRXMnO3

Zsolt Marton
University of Pennsylvania, martonzs@alumni.upenn.edu

Field Effect and Magnetically Induced Capacitive Tuning in Hole Doped La1-xSRXMnO3

Abstract
Electrostatic modulation of interface conduction between semiconductors and insulating oxides is the foundation of semiconductor technology. This field effect concept can be applied on complex oxides, such as high temperature superconductors and colossal magnetoresistive manganites, in order to create new electronic and magnetic phases. Competition and coexistence of multiple nanoscale phases make them exciting to study around phase transitions. This study on hole doped La1-xSrxMnO3 systems has a two-fold purpose.

One is the demonstration of the field effect on La1-xSrxMnO3 (x = 0.125, 0.2, 0.3, 0.5) thin films. It is an important step towards electrostatic control of material properties; however, a challenging task because of their charge carrier densities of 0.01-1 hole/unit cell, a few orders of magnitude larger than in doped semiconductors. Control by linear dielectrics needs huge, constantly applied bias. Energy efficient tuning with low voltages requires highly polar ferroelectric. Pb(Zr0.2Ti0.8)O3 was chosen, whose remanence provides 0.5 charge carrier/unit cell on the manganite/ferroelectric interface.

La1-xSrxMnO3/Pb(Zr0.2Ti0.8)O3 heterostructures were synthesized by pulsed laser epitaxy and remarkable conduction modifications were observed in the La1-xSrxMnO3. This can be a strong foundation of a new tool to research electronic oxides.

The second purpose of this work is to utilize the phase separation in manganites. There has been extensive research on multiferroic materials, in which dielectric and magnetic responses are controlled by magnetic and electric field, respectively. In order to demonstrate magnetically tuned capacitance, insulating La7/8Sr1/8MnO3 was studied. Drastic capacitance change in magnetic field was shown through a phase transitions and explained in the framework of electronic phase separation. It makes this material eligible for high frequency magnetoelectric applications.

Modulating charge carriers, mobility and magnetism in magnetic oxides, superconductors and superlattices has a great impact on the emerging field of oxide electronics. These compounds overcome the scaling limitations of conventional semiconductors; using low operation voltage oxide ferroelectrics lowers energy consumption. This thesis shows that changing fundamental physical properties of complex oxides on the atomic scale is possible by ferroelectric field effect. This technique is proposed as a tool to study thin films, artificially stacked structures and to induce and optimize novel phases and phenomena.

Degree Type
Dissertation

Degree Name
Doctor of Philosophy (PhD)

Graduate Group
Materials Science & Engineering

FIELD EFFECT AND MAGNETICALLY INDUCED CAPACITIVE TUNING IN HOLE DOPED $La_{1-x}Sr_xMnO_3$

Zsolt Marton

A DISSERTATION

in

Materials Science and Engineering

Presented to the Faculties of the University of Pennsylvania

in

Partial Fulfillment of the Requirements for the

Degree of Doctor of Philosophy

2010

Supervisor of Dissertation

_____

Takeshi Egami
Adjunct Professor

Graduate Group Chairperson

_____

Ju Li
Associate Professor

Dissertation Committee

Charles Graham	I-Wei Chen	Jay Kikkawa
Professor Emeritus	Professor	Associate Professor

To my Mother

and all those in my heart

ACKNOWLEDGMENT

First of all I would like to express my deepest appreciation to my adviser, Professor Takeshi Egami, who has always supported me and my research. Valuable conversations with him lifted me up and kept me going throughout all these years. Thank you for your patience as well!

Dr. Ho Nyung Lee deserves many thanks for teaching me, among many things, the essentials of quality oxide film growth, allowing me to work with him.

I would like to give thanks to my dissertation defense committee: Professors I-Wei Chen ,. Charles Graham and Jay Kikkawa (in alphabethical order), for going through the program with me and helping me grow an independent researcher.

I am grateful for the Egami group's members for helpful opinions and the comfortable atmosphere they provided during my research. I do not want to go "personal" but let me highlight Dr. Wojtek Dmowski, Dr. Konstantin Lokshin I got to work with on some projects. Dr. Rinat F. Mamin, visitor scientist with whom I worked on later published projects, should be mentioned in this section.

My greatest gratitude to Dr. Hans M. Christen and his Thin Films and Nanostructures Group at Oak Ridge National Laboratory. Let me name some of those with whom I interacted on a daily basis which meant an incredible emotional support, more than they would ever think: Dr. Gyula Eres, Dr. Charlee Bennett, Dr. Dae Ho Kim,

Dr. Hyunsik Kim, Dr. Sung-Suk Ambrose Seo, and Dr. Taekjib (TJ) Choi. The friendly and highly professional working environment, in which I conducted most of my

dissertation research, will always have an impact on my scientific growth. As “civilians” they were always supportive friends outside the lab.

People from other groups in the same Laboratory need to be thanked for scientific discussions and sometimes more than that: Dr. Brian C. Sales, Dr. Rongying Jin, Dr.Shiliang Li and Dr. Thomas Zacharia Ward. I got to taste the world of oxide growth by molecular beam epitaxy, which definitely broadened my knowledge and experience, even if that work is not included. For this reason I would like to mention here Dr. Rodney A. McKee as well as Frederick J. Walker. The two years I spent in their lab will always be remembered.

Now that I am getting more and more emotional while thinking of my support network, let me dedicate a paragraph to those people who used to shape me as a young student and will always be a huge part of what I will become in Life: my Hungarian professors in Debrecen - Dr. Gábor Erdélyi and Dr. Judit Darai - as well as my German mentor in Kiel – Prof. Dr. Franz Faupel. They realized my eagerness and helped me to start the quest for an international career.

The gratefullness I owe to the following people is anything but easy to describe. Long-time friends of mine in no particular order – Tamás Gál, Rita and John Mathew, Cinzia Metallo, Ferenc Stercel, Gabriella Kornberger, Zohreh Keshavarz and Annamária Nagy – have seen me falling into the deep and getting back on the horse over and over again for so many years. I am glad you stayed with me and hope for a way to return the sacrifice.

I appreciate the unmeasurable support, endless and kind conversations, daily coffee breaks, and Saturday night get-togethers I have got with Lídia & Norbert Podhorszki, Roselyne Barreto Tchoua, Emese Peintler-Kriván, Balázs Sipos, Krisztián Horváth,

Vilmos Kertész, Marcos de Lucca Moreira Gomes, Nicole Labbé and Nicolas Olivier André. Without them my life in Knoxville, TN would have been hard to imagine…and live, actually.

Sarah Seong Min Wu has stood by me ever since we met and put up with all the issues I had as well as those she only thought I had, but I really did not :o). She supported me with unconditional love and without her I would have been bored to death. Here it is, documented! Mina C, you will always have a special place in my heart.

Last, but certainly not least I thank my Mother, the only person who has been there for me from the very beginning and never lost faith in me even in the darkest moments. Ever since I left Hungary, she has been living alone and patiently waiting for me to come and visit her whenever I am able to. I can just guess how hard it was for her throughout all these years and I will do everything in my power to ease her life in the future.

Research sponsored by the LDRD Program of ORNL, managed by UT-Battelle, LLC for the U.S. Department of Energy and by NSF DMR-0404781.

ABSTRACT

FIELD EFFECT AND MAGNETICALLY INDUCED CAPACITIVE TUNING IN HOLE DOPED $La_{1-x}Sr_xMnO_3$

Zsolt Marton

Takeshi Egami

Electrostatic modulation of interface conduction between semiconductors and insulating oxides is the foundation of semiconductor technology. This field effect concept can be applied on complex oxides, such as high temperature superconductors and colossal magnetoresistive manganites, in order to create new electronic and magnetic phases. Competition and coexistence of multiple nanoscale phases make them exciting to study around phase transitions. This study on hole doped $La_{1-x}Sr_xMnO_3$ systems has a two-fold purpose.

One is the demonstration of the field effect on $La_{1-x}Sr_xMnO_3$ (x = 0.125, 0.2, 0.3, 0.5) thin films. It is an important step towards electrostatic control of material properties, however, a challenging task because of their charge carrier densities of 0.01-1 hole/unit cell, a few orders of magnitude larger than in doped semiconductors. Control by linear dielectrics needs huge, constantly applied bias. Energy efficient tuning with low voltages requires highly polar ferroelectric. $Pb(Zr_{0.2}Ti_{0.8})O_3$ was chosen, whose remanence provides 0.5 charge carrier/unit cell on the manganite/ferroelectric interface.

$La_{1-x}Sr_xMnO_3/Pb(Zr_{0.2}Ti_{0.8})O_3$ heterostructures were synthesized by pulsed laser epitaxy and remarkable conduction modifications were observed in the $La_{1-x}Sr_xMnO_3$. This can be a strong foundation of a new tool to research electronic oxides.

The second purpose of this work is to utilize the phase separation in manganites. There has been extensive research on multiferroic materials, in which dielectric and magnetic responses are controlled by magnetic and electric field, respectively. In order to demonstrate magnetically tuned capacitance, insulating $La_{7/8}Sr_{1/8}MnO_3$ was studied. Drastic capacitance change in magnetic field was shown through a phase transitions and explained in the framework of electronic phase separation. It makes this material eligible for high frequency magnetoelectric applications.

Modulating charge carriers, mobility and magnetism in magnetic oxides, superconductors and superlattices has a great impact on the emerging field of oxide electronics. These compounds overcome the scaling limitations of conventional semiconductors; using low operation voltage oxide ferroelectrics lowers energy consumption. This thesis shows that changing fundamental physical properties of complex oxides on the atomic scale is possible by ferroelectric field effect. This technique is proposed as a tool to study thin films, artificially stacked structures and to induce and optimize novel phases and phenomena.

Table of Contents

List of Tables

List of Illustrations

1. Introduction

In the year of 1965, a little while after integrated circuits became booming parts of applied electronics Gordon Moore made his famous statement (Figure 1-1) that the number of electronic devices integrated on unit area increased exponentially.[1] He believed this trend to continue leading to dramatic shrinkage in the device dimensions. In fact, this tendency still holds even today and today's integrated feature size hit the sub-micron range. However, microelectronics industry faces a huge problem in following this trend-line to the future. First, quantum effects in the semiconductor can come into play on the nanometer scale. Furthermore, the insulation between devices breaks down when reaching the thickness of a couple of nanometers degrading the circuit's performance. In order to overcome this problem, new kind of oxides must be deployed.

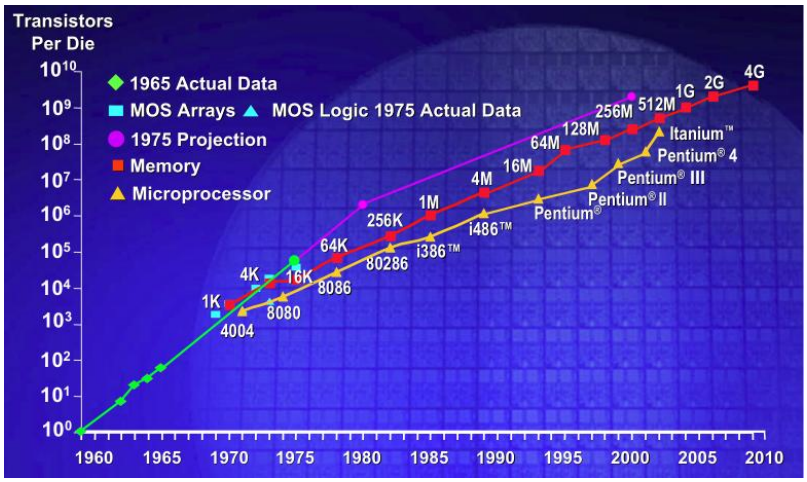

Figure 1-1 Moore's Law in terms of device density

Recent computation technology's most important parts are random access memories (RAM). Their basic units are currently memory cells consisting of a field effect transistor (FET) and a capacitor (1T/1C cells). The capacitor holds the bit state while the FET is

used to read out that information. Packing denser such double-element cells onto a silicon wafer requires smaller lateral dimensions. In order for the capacitors to provide the essential capacitance, the oxide thickness must be smaller. Eventually, it hits the limit of a few nanometers beyond which it breaks down, either by quantum mechanical tunneling or by forming ionic channels. One way to keep up with the same capacitance is to use high-K insulators so that the thickness does not have to be small.

Prospective high-K insulators for this purpose are oxides such as amorphous $HfSi_xO_y$, La_2O_3, $SrTiO_3$, $SrZrO_3$ or $SrHfO_3$ [2,3,4,5,6,7,8]. Although the dielectric properties of these alternative oxides are superior to the conventional ones, they come with new problems.

Table 1-1 Alternative gate oxides from Ref. [9].

	K	Gap (eV)	CB offset (eV)
Si		1.1	
SiO_2	3.9	9	3.2
Si_3N_4	7	5.3	2.4
Al_2O_3	9	8.8	2.8 (not ALD)
Ta_2O_5	22	4.4	0.35
TiO_2	80	3.5	0
$SrTiO_3$	2000	3.2	0
ZrO_2	25	5.8	1.5
HfO_2	25	5.8	1.4
$HfSiO_4$	11	6.5	1.8
La_2O_3	30	6	2.3
Y_2O_3	15	6	2.3
a-$LaAlO_3$	30	5.6	1.8

Their crystal structure is not compatible with that of silicon. Lattice mismatch defects and strong atomic inter-diffusion inhibit good electronic interface. Although successful

attempts have been made to engineer good electronic interface between crystalline perovskite oxide and silicon, the procedure (molecular beam epitaxy) is time-consuming and requires huge apparatus as well as sophisticated conditions.[3] Furthermore, the mobility in such devices – which determines the reading speed of the memory – is reported to be below those in commercial ones.[4] Other issues, when using linear dielectrics, are destructive read-out, slowing down of the memory by the refreshing process, as well as the constant power consumption to keep the memory from discharging.

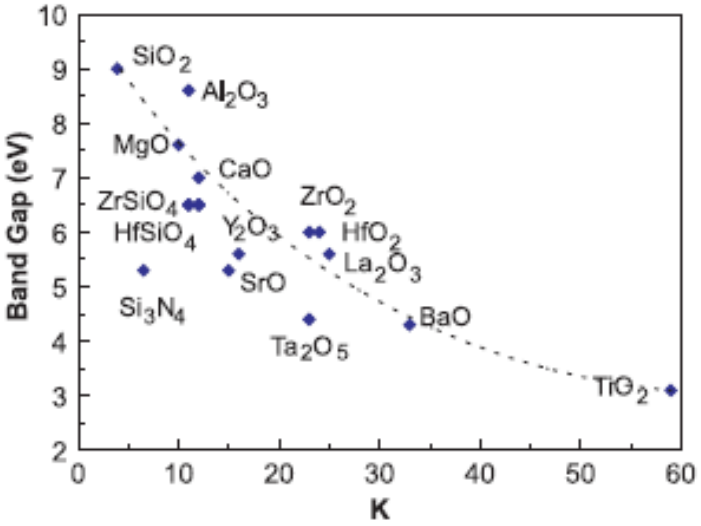

Figure 1-2 Band gap of prospective gate oxides as a function of dielectric constant *K* from Ref. [10].

Switching these dielectrics to ferroelectrics greatly improves the performance of a cell. First, the reading process is not destructive; it can be done by measuring the channel's conducting state. One does not need extra power to keep the bit information when using long retention time ferroelectric. Writing speed is significantly increased, and reading from existing ferroelectric random access memory (FE-RAM) cells is as fast as reading

modern dynamic RAMs of the same feature size. The main goal of the recent FE-RAM research is to replace 1T/1C structures by 1T configuration. It requires the ferroelectric to be integrated as a gate oxide. Many attempts have been made to achieve this goal, mostly by using thin buffer oxides between the PZT and Si to prevent inter-diffusion.[11]

Another approach is to incorporate perovskite oxide semiconductors, already matching the new insulators, as metal-oxide-semiconductor field effect transistor (MOSFET) channels. The idea of doping perovskite transition metal oxides through the field effect has been around for about four decades. In the early 60's, ferroelectric oxides were already used to change the critical temperature of superconductors.[12,13,14] Functional transition metal oxides, such as the high T_c superconductor cuprates and colossal magnetoresistive manganites, have large charge carrier concentrations of ~10^{21}-10^{23} cm^{-3}. To modulate their doping level significantly we need ferroelectrics with huge polarization, such as $Pb(Zr_{0.2}Ti_{0.8})O_3$ (PZT). The concentration mentioned above translates to a polarization of 10-100 $\mu C/cm^2$.[15] It is not easy to reach this upper limit but some groups are now successful in synthesizing good films,[16,17] which may provide improved electronic interface quality. Since these correlated electron systems show drastic change in the conduction state by chemical doping, they are promising candidates for channel materials in ferroelectric memory devices.

Other than the functionality, the concept of field effect offers a flexible and efficient template to map out material phases, explore fine details and discover new or enhanced properties in phase transition regimes. Certain bulk materials segregate or decompose, but can be stabilized by epitaxial strain and manipulated electrostatically.

This dissertation focuses on such all-perovskite field effect structures and other functionalities of manganites, in general. I summarized a set of works, which studied electronic phase separated single crystalline bulk and thin film manganites. After the introduction, I give a brief overview on the physics of mixed valent manganites, their complex but very rich and useful properties in Chapter 2.

Chapter 3 is depicting the experimental facilities and methods I used to carry out the sample synthesis and characterization of single crystalline thin films. It gives an overview on pulsed laser epitaxy and several characterization techniques necessary to obtain high quality samples and results.

Chapter 4 studies numerous pulsed laser ablation parameters and their impact on material properties via the example of the undoped $LaMnO_3$.This way of starting up was necessary to get familiar with the sensitivity of thin film quality for the different growth parameters such as growth pressure, laser energy density on the target etc. The observation of how important fine-tuning of growth conditions was very important in synthesizing highly epitaxial single crystalline thin films for field effect studies.

Chapter 5 describes the initial steps I made to demonstrate ferroelectric field effect in doped manganite thin films, where charge carrier modulation is a real challenge due to very short screening length. I tried various methods and compositions to overcome this barrier and partially succeeded in showing significant change in the manganites electronic and magnetic response presumably caused by field effect. Further experiments to confirm it are still needed.

References

[1] G.E. Moore, Electronics **38** (8), (1965).

[2] C. Rossel, B. Mereu, C. Marchiori, D. Caimi, M. Sousa, A. Guiller, H. Siegwart, R. Germann, J.P. Locquet, J. Fompeyrine, D.J. Webb, C. Dieker, and J.W. Seo, Appl. Phys. Lett. **89**, 053506 (2006).

[3] R.A. McKee, F.J. Walker, and M.F. Chrisholm, Phys. Rev. Lett. **81**, 3014 (1998).

[4] K. Eisenbeiser, J.M. Finder, and Z. Yu, et al., Appl. Phys. Lett. **76** (10), 1324 (2000).

[5] G. Wilk and R. Wallace, Appl. Phys. Lett. **74**, 2854 (1999).

[6] J.Q. He, C.L. Jia, V. Vaithyanathan, D.G. Schlom, J. Schubert, A. Gerber, H.H. Kolhstedt, and R.H. Wang, J. Appl. Phys. **97**, 104921 (2005).

[7] B.J. Kennedy C.J. Howard, and B.C. Chakoumakos, Phys. Rev. B **60**, 2972 (1999).

[8] N. Jin-Aun, N. Sugii, K. Kakushima, P. Ahmet, K. Tsutsui, T. Hattori, and H. Iwai, IEICE Electronics Express, **3** (13), 316 (2006).

[9] J. Robertson, Eur. Phys. J. Appl. Phys. **28**, 265–291 (2004).

[10] J. Robertson, J. Vac. Sci. Technol. B **18**, 1785 (2000).

[11] D. Cai, P. Li, S. Zhang, Y. Zhai, A. Ruan, Y. Ou, Y. Chen, and D. Wu Appl. Phys. Lett. **90**, 153513 (2007); T.P. Juan, C. Chang, and Y. Lee, IEEE Electron Device Letters 27 (4), (2006).

[12] R.E. Glover and M.D. Sherill, Phys. Rev. Lett. **5**, 248 (1960)

[13] T.G. Berlincourt, Phys. Lett. 29A, **308** (1969)

[14] H.L. Stadler, Phys. Rev. Lett. **14**, 979 (1965)

[15] C.H. Ahn, A. Bhattacharya, M. Di Ventra, J.N. Eckstein, C. Daniel Frisbie, M.E. Gershenson, A.M. Goldman, I.H. Inoue, J. Mannhart, A.J. Millis, A.F. Morpurgo, D. Natelson, and J. Triscone, Rev. Mod. Phys. **78**, 1185 (2006)

[16] M. Lisca, L. Pintilie, M. Alexe, and C.M. Teodorescu, Appl. Surf. Sci. **252**, 4549 (2006)

[17] H.N. Lee, S.M. Nakhmanson, M.F. Chisholm, H.M. Christen, K.M. Rabe, and D. Vanderbilt, Phys. Rev. Lett. **98**, 217602 (2007)

2. Background

Doped manganites have been known since 1950 through Jonker's and van Santen's work.[1] They reported on ferromagnetism in chemically mixed crystals of $LaMnO_3$-$CaMnO_3$, $LaMnO_3$-$SrMnO_3$ and $LaMnO_3$-$BaMnO_3$. This discovery led to numerous experimental studies which led to the observation of a rich list of coexisting magnetic and electronic phases in $La_{1-x}Ca_xMnO_3$ and $La_{1-x}Sr_xMnO_3$ in the entire doping level range.[2] Later theoretical works tried to explain these unusual phenomena by introducing the concept of double exchange by Zener[3], as well as Anderson and Hasegawa[4], de Gennes.[5]

Recently these materials have become the focus of intense research activities because of reasons related to possible applications. External magnetic field influences the electronic transport properties of most perovskite manganites. In certain doping and temperature ranges, they exhibit colossal magnetoresistive (CMR) behavior: in applied magnetic field the electronic resistivity changes by orders of magnitude, because magnetic order seems to enhance conductivity. Furthermore, the CMR compounds undergo a metal-to-insulator transition, which is a quite broad transition and will be discussed later in terms of percolation theory.

Very large CMR constants were found in epitaxial thin films of chemically doped manganites at room temperature, which also boosted active research on these materials.[6] It makes them very attractive for industrial applications except that the CMR has to occur at room temperature where magnetic detection is needed, whereas it is observed at the moment only at low temperatures.

A clear and unified explanation of physical mechanisms leading to CMR effect has not been given yet. One of the best descriptions recently proposed is based on nano- or micron scale electronic phase separation. This picture involves the coexistence of at least two different magnetic/electronic phases, such as paramagnetic insulator and ferromagnetic metallic. Their competition and percolation determines the basic properties of the compound.[7,8,9,10,11,12,13] An exact physical picture of these physical phenomena would be applicable onto other systems, such as high temperature superconductors, where electron correlations and strong interactions between charge, spin, orbital and lattice degrees of freedom play a significant role.[14] The other phenomenon making manganites fascinating is the almost complete spin polarization in the CMR composition range.[15]

In this chapter I am giving a brief introduction on structural, magnetic and electronic properties of manganites in general as well as the most contemporary description to explain the physics behind the rich phase diagrams. Since it is a quite broad topic and cannot be fully covered in this chapter, to learn more about correlated electron systems the reader is advised to consult extensive reviews available today.[16,17,18,19,20]

2.1 Crystal Structure of Manganites

Manganites of chemical formula of $AMnO_3$ form lattices, which are mostly slightly modified perovskite structures (Figure 2-1). The A cation, which is Lanthanum in our case, is located in the corners of a cube, while the manganese ion is surrounded by an oxygen octahedron. These octahedra are usually sharing corners in the manganites this dissertation focuses on.

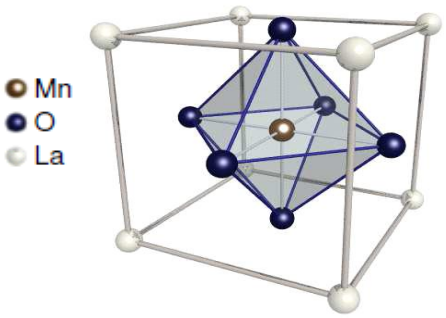

Figure 2-1 Cubic perovskite structure of $AMnO_3$ manganates.

These octahedra can undergo Jahn-Teller distortion, which perturb relative orientations of electronic orbitals as well as the octahedra themselves. This way the lattice structure can change from cubic to orthorhombic or rhombohedral. This perturbation in the crystal structure is related to the sizes of the ions, and can be characterized through the tolerance factor defined like this:

$$f = \frac{1}{\sqrt{2}} \frac{r_{Mn} + r_O}{r_A + r_O} \tag{2-1}$$

The tolerance factor determines the crystal structure in doped manganites as explained in Figure 2-2.

For tolerance factor 1 we get a perfect cubic lattice with a Mn-O-Mn bond angle of 180º. When lowering *f*, the structure turns into rhombohedral. Tilting the octahedral also leads to bending Mn-O-Mn bond angle, which plays a huge role in resulting magnetism and electronic transport, as it will be discussed later on.

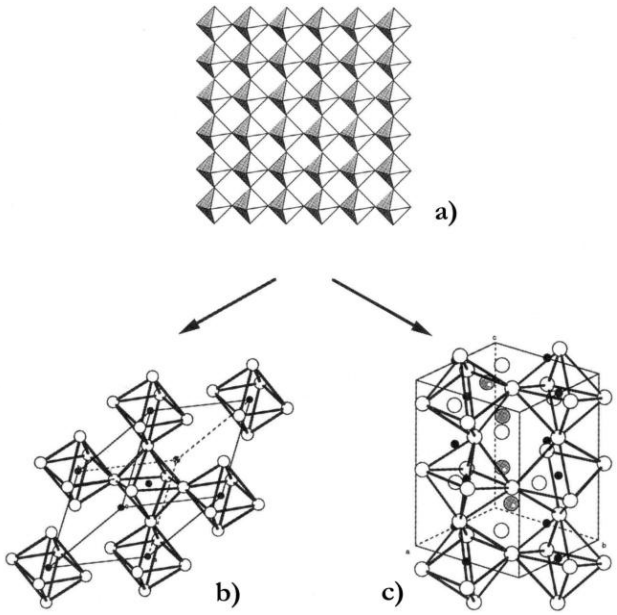

Figure 2-2 Crystal structure for different tolerance factors. (a) Simple cubic in case there is no distortion present in the crystal. For 0.96 < f < 1.00 the resulting crystal structure is rhombohedral (b), while f < 0.96 gives orthorhombic lattice (adopted from Ref.[16]).

The tolerance factor can be easily changed by chemical doping. It has a great impact on manganites' physics. The normally La^{3+} ions are replaced by divalent ions such as Ca^{2+}, Ba^{2+} or Sr^{2+}. The doping ions have different ionic radii influencing the tolerance factor and so magnetic and electronic properties of the mixed valence systems. The lattice distortion induced by doping is relatively small in the case of manganites under study in this work, so I normally used the pseudo-cubic nomenclature for structural characterization.

2.2 Electronic Structure on Manganites

2.2.1 The parent compound: $LaMnO_3$

In order to understand the electronic and magnetic correlation along the entire mixed valent phase diagram, the parent compound needs fundamental understanding. Lanthanum ions form a rather strong bond with the oxygen ions in the La-O plane due to the huge electron affinity of the O^{2-} species. That is why they can be treated as inert spacer between the MnO_6 octahedra and in most cases the La-O planes are irrelevant when considering the electronic structure or magnetism in mixed valent manganites.

In the undoped composition, manganese ions have the $[Ar]3d^4$ structure resulting in Mn^{3+} valence. Without any ligand shell around it, the Mn^{3+} ion has one electron and five degenerate orbital states available (see Figure 2-3). As soon as it is surrounded by an oxygen octahedron, the electrostatic field of the oxygen ions, so-called crystal field, splits the degenerate states of the *d* electron. There are three lower energy degenerate orbitals called t_{2g} (d_{xy}, d_{xz}, d_{yz}) pointing in-between the oxygen p orbitals, while the remaining two higher energy orbitals (e_g) have direct overlap with the oxygen *2p* ones. They are marked as $d_{z^2-r^2}$ and $d_{x^2-y^2}$. The energy difference is easy to understand, since the two e_g orbitals face the oxygen electronic orbitals and feel the strong Coulombic repulsion, making it less desirable for electron on the manganese site. The energy difference between the t_{2g} and e_g states is called the crystal field splitting energy (Δ_{CF} = 10Dq) and is about the order of 1eV.[16] The on-site Hund's coupling energy, on the other hand, is more than the crystal field splitting. It leads to strong coupling between the spins of the core t_{2g}

electrons and the e_g electron and eventually spin polarized e_g electrons mentioned above. The situation is schematically shown later by Figure 2-4.

2.2.2 Jahn-Teller Effect

If an e_g orbital is occupied by an electron, we observe a fascinating phenomenon called Jahn-Teller distortion or effect. The degenerate *3d* orbitals split when put in a crystal field. In the case of octahedral coordination, the one orbital pointing to the z-direction (d_z^2-r^2) will be the lower energy choice. As soon as the electron occupies that orbital, the e_g electron interacts with the oxygen $2p_z$ electrons and pushes the upper and displaces the upper and lower oxygen ion like depicted in Figure 2-4. This way the Coulombic energy is lowered by building up a strain field. This is called the Jahn-Teller distortion.

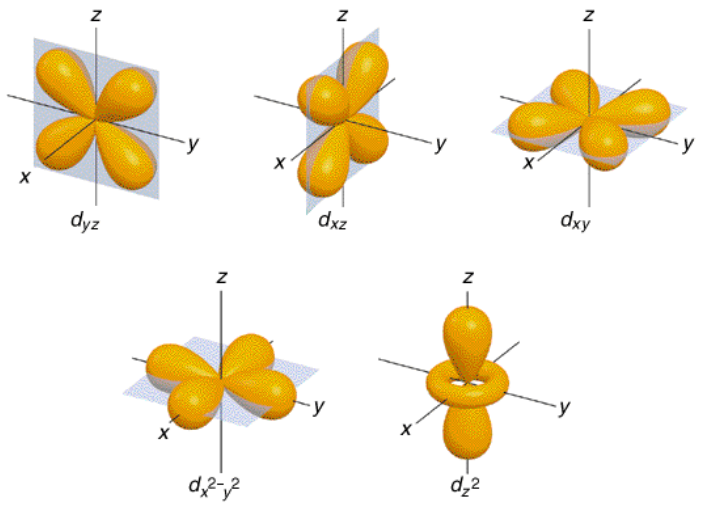

Figure 2-3 Angular component of the manganese ionic orbitals in octahedral crystal field.

The effect also influences the t_{2g} levels because of obvious symmetry breaking reasons. d_{xz} and d_{yz} levels have the same energy but lower than in the case of undisturbed *3d* ion, while the d_{xy} orbital is getting higher in terms of energy, since the oxygen ions in the *xy* plane are getting closer. Interesting fact, though, that the net energy of the Jahn-Teller distorted orbital configuration does not change.[21]

The resulting strain field cooperatively distorts the whole lattice. The distorted octahedral self-organize in the *xy* plane in a zigzag way. This collective Jahn-Teller effect can give rise to either rhombohedral or orthorhombic structure. This strongly localized strain field realized by purely electronic reasons is called a Jahn-Teller polaron.[22] The explanation of the strong localization is easy to see. Once the e_g electron wants to hop to a neighboring site, the whole strain field has to be displaced, which costs tremendous amount of energy.

It can be seen, that as soon as we dope the parent compound by 2+ valence ions, we dope holes in the system and destroy the e_g electrons as and the Jahn-Teller polaron. The doped holes become delocalized as a result of missing strain field trapping them. Doping introduces delocalization and eventually electronic conduction.

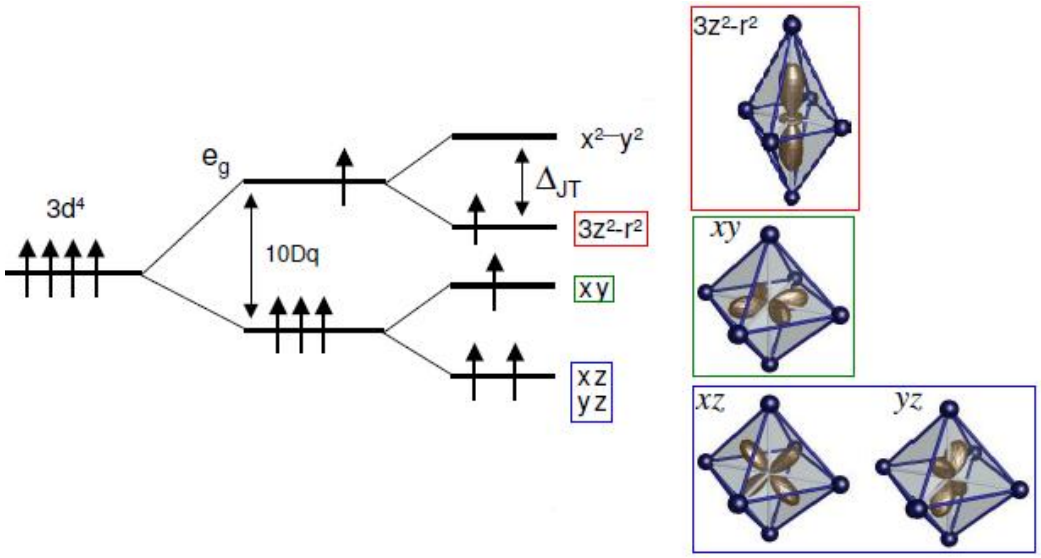

Figure 2-4 Energy level splitting of 3d electrons due to octahedral crystal field and Jahn-Teller distortion.

2.2.3 Exchange Mechanisms

The parent $LaMnO_3$ is an antiferromagnetic insulator below the Néel temperature of about 140K. Above that it is paramagnetic. Ferromagnetic correlations can be induced by chemical doping. When doping, the electron stoichiometry looks like this

$$La_{1-x}^{3+}Sr_x^{2+}Mn_{1-x}^{3+}Mn_x^{4+}O_3^{2-} \tag{2-2}$$

The mixed valence feature has a great influence on magnetic and electronic conductive properties of manganites, as mentioned before. After about 8 percent hole doping ferromagnetic correlations set in and beyond x = 0.17 electronic conduction starts. To qualitatively explain the rich phase diagram of doped manganites, the concept of superexchange and double exchange needs introducing. Well detailed and quantitative descriptions of the exchange interactions can be found in several publications.[3,4,5,23]

In order to explain the magnetic structure, we only need to consider the spin alignments on the manganese ions. La^{3+}, Sr^{2+} and O^{2-} have the noble gas configuration and that is why they exhibit no magnetic moment. Also, *3d* transition metals in cubic environment display zero net orbital moment. As a consequence, it is enough to discuss the spin moments on the manganese ions to describe magnetism. These are composed of $S(Mn^{3+}) = 2$ and $S(Mn^{4+}) = 3/2$.

For electronic conduction, only the e_g electrons count since the t_{2g} levels are way below the Fermi level and they are strongly localized due to the crystal field splitting. Indirect superexchange and double exchange interactions are necessary to explain the magnetic correlations and conductions states in mixed valent manganites. Since the manganese ions are fairly far away from each other, the oxygen *2p* orbitals are necessary to involve in the description. During the electronic transport the spins of the conduction electrons are to be kept unchanged since spin flipping is energetically not favorable.

2.2.3.1 Superexchange

Superexchange models direct exchange interaction between Mn^{3+} ions disregarding the O^{2-} in between. In this picture kinetic energy, characterized by the hopping amplitude $t > 0$ and potential energy (U) are used. The hopping integral says how delocalized the electron is, while $U > 0$ is the Coulombic energy mostly depicting the repulsion between two on-site electrons.

The superexchange relation can be derived from second order perturbation theory [21], which provides the coupling energy J in terms of t and U as follows:

$$J \propto -\frac{t^2}{U} \tag{2-3}$$

Qualitatively, the oxygen ions can be disregarded, when discussing the superexchange interaction (Figure 2-5). Two neighboring $d_{z^2-r^2}$ orbitals pointing toward each other are considered. The degenerate nature is already assumed due to Jahn-Teller effect. In case the e_g electrons' spin orientation is antiparallel, then virtual hopping is forbidden by the Pauli principle, so there is no energy gain. However, when spins are aligned parallel, virtual hopping can occur and energy is gained via delocalization. It comes with antiferromagnetic correlation due to strong Hund's coupling to the t_{2g} electrons on the manganese ion the electron hops onto.

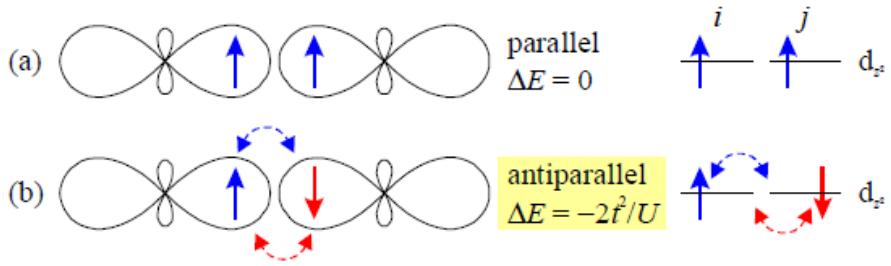

Figure 2-5 Schematic of the superexchange relation between two non-degenerate $d_{z^2-r^2}$ orbitals with parallel (a) and antiparallel (b) spin orientation.

Superexchange is, on the other hand, a really simple description and often not enough to explain certain phenomena. A much more refined picture is provided by the so-called Goodenough-Kanamori-Anderson (GKA) rules.[24,25] It takes into account several orbital orientations and electronic occupations of orbitals. These rules give a satisfactory and

easy-to-understand explanation for the parent compounds on both ends of the $LaMnO_3$-$SrMnO_3$ phase diagram.

Applying these rules, one can easily explain the observed ferromagnetic coupling in the *ab* plane of $LaMnO_3$ as well as the out-of-plane anti-ferromagnetic interaction (A-type antiferromagnet). The same way can be explained the G-type anti-ferromagnetism in $SrMnO_3$, where every single neighboring manganese ion is anti-ferromagnetically coupled to each other.

2.2.3.2 Double Exchange

When holes are introduced in the system by replacing La ions by Sr/Ca ions, the magnetic interaction can be well described by the double exchange model. It explains the appearance of ferromagnetism and the delocalization/conduction in doped compounds. It also provides with a simple but effective explanation on how negative colossal magnetoresistance occurs in certain composition regions.

The setup is very similar to that of the superexchange; however one starts out with different valences: Mn^{4+}-O-Mn^{3+}. This fact clearly influences the hopping process, since there is no repulsing on-site Coulombic interaction on the other ion. Now all the energy terms should be taken into account.

The first I discuss is, where there is an e_g electron on a Mn^{3+}, whose spin is aligned with the t_{2g} spins. It can hop via the oxygen and arrive in an unoccupied e_g orbital if the Mn^{4+} has the parallel t_{2g} spins as depicted in Figure 2-6 (a). This way the electron lowers

it net energy by the kinetic energy amount due to delocalization and also the lack of on-site Coulombic interaction favors this exchange.

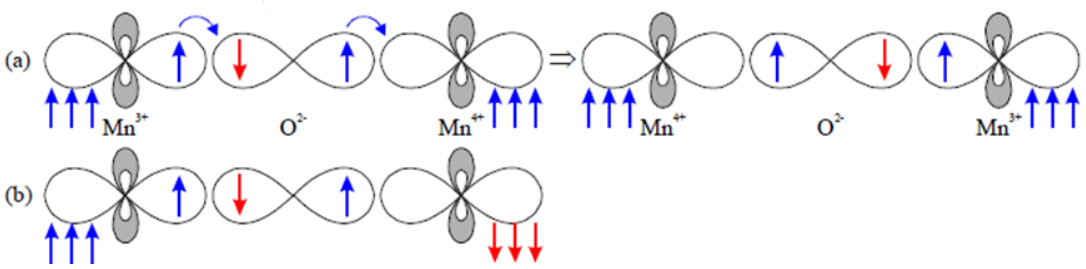

Figure 2-6 Schematic presentation of the double exchange mechanism. In the case of parallel core spin alignment (a), electrons can hop between Mn ions via the O^{2-} *2p* orbital. However, antiparallel spins lead to localization (b).

Figure 2-6(b) shows the other possibility, when the Mn^{4+} t_{2g} spins are aligned antiparallel with respect to those of the Mn^{3+}. If the electron wanted to hop onto the neighboring Mn site, it should overcome a relatively large Hund's coupling energy. It is plain to see, that in a mixed valent situation ferromagnetic and delocalized states are energetically favorable and they eventually win over the localized anti-ferromagnetic order. It explains the ferromagnetic metallic phase observed at certain doping levels in CMR manganites. So one can see that the e_g electrons form a band, whose width W is proportional to the hopping integral t.[22]

From the double exchange model comes a really fascinating consequence. Since the delocalized electron interacts with the t_{2g} electrons via Hund's coupling, the conduction electrons turn out to be 100% spin polarized in the ground state. This was also confirmed experimentally by photoemission spectroscopy.[15]

In case one is curious about thermal excitation, the hopping integral t becomes a function of the angle θ_{ij} between the nearest neighbor core spins.

$$t_{eff} = t\frac{\theta_{ij}}{2} \tag{2-4}$$

As it shows, a maximum conduction is gained when the core spins are ferromagnetically aligned, while ideally zero, if the spins are antiparallel. At higher temperatures, upon heating, the spins are randomly aligned due to thermal excitations. This way the ferromagnetism as well as good electric conduction is suppressed. This metal-to-insulator transition occurs at the Curie temperature; however it is a quite broad transition on the temperature scale (a couple of tens of degrees). In this context, colossal magnetoresistance can be explained by a fairly simple picture. An external magnetic field forces local spins to align parallel to the external field and so increase the electron hopping integral, *i.e.* conductivity, due to the double exchange mechanism. Since at low temperature the spins are already aligned ferromagnetically, an external field does not have a huge effect, ergo the magnetoresistance is lower. In the transition region, the material is in a critical state, where ferromagnetism is all over the crystal, but no percolation happens. Percolation is triggered by external magnetic field, which suddenly flips the conduction state into metallic and so leads to insulator-to-metal transition. At higher temperature the external field is not enough to overcome the thermal excitations, so the effect remains minor. CMR peaks at the metal-insulator transition.

Even if the double exchange mechanism describes the correlation between magnetism and electric conductivity very well, it has limitations, which should be resolved by introducing a further concept of electronic phase separation.

2.2.4 The Phase Diagram of $La_{1-x}Sr_xMnO_3$

This subsection will introduce the fairly rich phase diagram of $La_{1-x}Sr_xMnO_3$ (see Figure 2-7). The parent compound, $LaMnO_3$, is an A-type antiferromagnetic insulator below its Néel temperature of around 140K. It has orbital ordered, ferromagnetically coupled *ab* planes coupled antiferromagnetically to the neighboring *ab* planes. It can be described by the superexchange interaction discussed above.

When doped, a low temperature ferromagnetic but insulating phase sets in above $x \sim 0.1$ doping level. This phase, which survives up to $x \sim 0.17$, cannot be modeled by a simple double exchange interaction, since electronic conduction starts only above $x = 0.17$ despite the ferromagnetic correlation. This magnetic-electronic switching is accompanied by an orthorhombic-to-rhombohedral transition as well.

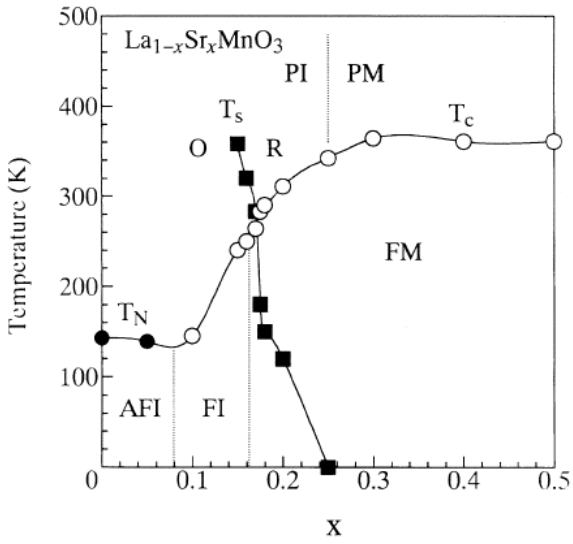

Figure 2-7 Part of the rich structural, magnetic and electronic phase diagram of $La_{1-x}Sr_xMnO_3$ on the lanthanum rich side ($x \leq 0.5$). Orthorhombic (O) and rhombohedral (R) crystal structures serve as lattice basis for A-type antiferromagnetic and ferromagnetic insulator (AFI/FI), ferromagnetic metallic (FM) as well as high temperature paramagnetic insulator(PI) and metallic (PM) phases [16].

After the critical 0.17 doping, T_c increases monotonically to 370K at x = 0.3. Apparently, the number of Mn^{4+} ions grows and it lets the double exchange win over superexchange. On the other hand, this low T ferromagnetic insulator-to-metal transition coincides with a structural transition, so the abrupt change in the tolerance factor cannot be excluded from the possible explanations.

Even if most parts of the phase diagram can be explained by the competition between the two exchange mechanisms, some regions are still puzzling and cannot be fitted into this schematic picture. Such question is why the CMR effect peaks in the rhombohedral FM region at that particular doping, and not in the tetragonal range, where the doping is even more and it is still FM.[19] Obviously, the exchange mechanisms promoted above are not sufficient to explain the ferromagnetic insulator or the anti-ferromagnetic metallic

behaviors at doping levels $x > 0.5$. Also paramagnetic insulator states were detected in the FM doping region. There was transition temperature shift of about 20K observed due to isotope-effect in $La_{0.8}Ca_{0.2}MnO_{3+y}$, when ^{18}O replaced the conventional oxygen isotope.[26]

In the following, the model of electronic phase separation will be introduced, which will become relevant to explain certain experimental results in this thesis later such as colossal magnetocapacitance in low doped manganite single crystals and the possibly larger screening length in high charge carrier density LSMO films.

2.2.5 Electronic Phase Separation

In order to explain colossal magnetoresistance in electronically homogeneous doped manganites seems to be impossible. Explanations of CMR based on pure exchange mechanisms and Anderson localization, as well as the paramagnetic insulator state described only by a gas of small polarons [27] should be further developed.

The missing part of the puzzle is the concept of electronic phase separation. In this picture, coexistence and competition of two or more electronic and magnetic phases is assumed. The size clusters of different electronic/magnetic nature is mostly on the nanoscale [28], but can be even larger [29].

This model allows us to understand the phase diagram as well as the CMR effect [30] and is in good agreement with numerous experimental observations.[7,8,9,10] That is why scanning probe microscopy studies find regions with different conductivity under the transition temperature, whose relative fractions can be varied by external magnetic field. These clusters with dissimilar conductivity and magnetism will percolate and lead to the

formation of a new phase upon cooling or applied magnetic field, such as metal-insulator transition.

Electronic phase separation (see Figure 2-8) plays an important role in comprehending not only manganites, but other correlated electron systems, such as high temperature superconductivity.[27] Nice reviews on this picture can be found in Ref. [31] and Ref. [27], for example.

(a) (b)

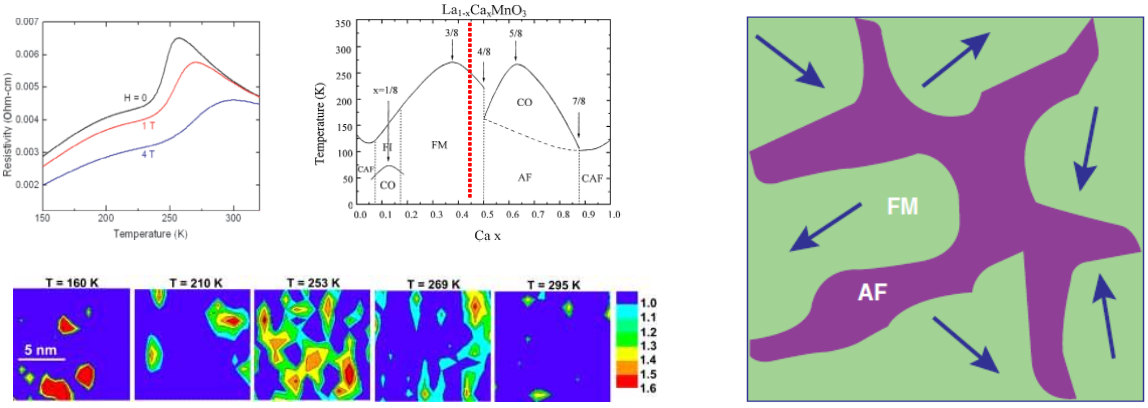

Figure 2-8 Electronic phase separation in manganites has been observed by several experimental techniques, like scanning electron nano-diffraction (a), for example [28]. (b) This schematic concept is a powerful tool for theoreticians as well [14] to study material properties of correlated electron systems.

2.3 Polarons

Polarons are immobile electrons with the strain field they create around themselves.[22] Polarons were always neglected when considering the metallic ground states of manganites, since the mixed valent nature and the double exchange mechanism ensures complete delocalization and polarons entirely disappear.[16] However, above a certain T_c polarons form again, and charge carriers form Jahn-Teller distortion, become localized due to the polaron's very high ~ 1 eV binding energy.

This effect is especially important for polaron hopping driven transport in narrow band gap manganites like $La_{1-x}Ca_xMnO_3$ or $Pr_{1-x}Ca_xMnO_3$.[32] Some experiments show that polarons in metallic phases are not to neglect. For instance in charge ordered compositions, like $La_{0.75}Ca_{0.25}MnO_3$ in Ref. [33], which are free of elastic stress and electronically completely homogeneous. Even in such a homogenous form they show a big CMR effect.[34] It means that in these cases, even electronic phase separation is not satisfactory to explain the materials behavior. The important role played by polarons were demonstrated through anisotropic charge density wave measurements done below and above the Curie temperature of x = ¼ charge ordered composition.[33] These experiments show that polaronic effects are not only relevant for the high temperature paramagnetic insulating states but also in the metallic phases. A quite wide overview is given on this topic in Ref. [35].

References

[1] G.H. Jonker and J.H. van Santen, Physica **XVI**, 599 (1950).

[2] E. Wollan and W. Koehler, Phys. Rev. **100**, 545 (1955).

[3] C. Zener, Phys. Rev. **82**, 403 (1951).

[4] P.W. Anderson and H. Hasegawa, Phys. Rev. **100**, 675 (1955).

[5] P.-G. de Gennes, Phys. Rev. **118**, 141 (1960).

[6] R. von Helmolt, J. Wecker, B. Holzapfel, L. Schultz and K. Samwer, Phys. Rev. Lett. **71**, 2331 (1993).

[7] T. Becker, C. Streng, Y. Luo, V. Moshnyaga, B. Damaschke, N. Shannon and K. Samwer, Phys. Rev. Lett. **89**, 237203 (2002).

[8] M. Fäth, S. Freisem, A.A. Menovsky, Y. Tomioka, J. Aarts and J. A. Mydosh, Science **285**, 1540 (1999).

[9] M. Uehara, S. Mori, C.H. Chen and S.-W. Cheong, Nature **399**, 560 (1999).

[10] Ch. Renner, G. Aeppli, B.-G. Kim, Yeong-Ah Soh and S.-W. Cheong, Nature **416**, 518 (2002).

[11] S. Yunoki, A. Moreo and E. Dagotto, Phys. Rev. Lett. **81**, 5612 (1998).

[12] M. Mayr, A. Moreo, J.A. Vergés, J. Arispe, A. Feiguin and E. Dagotto, Phys. Rev. Lett. **86**, 135 (2001).

[13] J. Burgy, M. Mayr, V. Martin-Mayor, A. Moreo and E. Dagotto, Phys. Rev. Lett. **87**, 277202 (2001).

[14] E. Dagotto, Science **309**, 257 (2005).

[15] J.-H. Park, E. Vescovo, H.-J. Kim, C. Kwon, R. Ramesh and T. Venkatesan, Nature **392**, 794 (1998)

[16] Y. Tokura, Colossal Magnetoresistive Oxides (Advances in Condensed Matter Science), Gordon and Breach Science Publishers, (2000).

[17] J.M.D. Coey, M. Viret and S. v. Molnár,Adv. Phys. **48**, 167 (1999).

[18] E. Dagotto, Nanoscale Phase Separation and Colossal Magnetoresistance, Springer Verlag, Berlin (2002).

[19] E. Dagotto, T. Hotta and A. Moreo, Phys. Rep. **344**, 1 (2001).

[20] V. Moshnyaga and K. Samwer, Handbook of magnetism and advanced magnetic materials, Volume 5: Spintronics and magnetoelectronics, John Wiley & sons (2007).

[21] S. Blundell, Magnetism in Condensed Matter, Oxford University Press, (2003).

[22] Ch. Kittel, Introduction to Solid State Physics, (2004).

[23] J.B. Goodenough, Phys. Rev. **100**, 564 (1955).

[24] J.B. Goodenough, Magnetism and Chemical Bonds, Interscience Publishers, New York (1963).

[25] D.I. Khomskii and G.A. Sawatzky, Sol. State Comm. **102**, 87 (1997).

[26] G.-M. Zhao, K. Conder, H. Keller, K.H. Müller, Nature **381**, 676 (1996).

[27] E. Dagotto, New Journal of Physics **7**, 67 (2005).

[28] J. Tao, D. Niebieskikwiat, M. Varela, W. Luo, M. A. Schofield, Y. Zhu, M. B. Salamon, J. M. Zuo, S. T. Pantelides, and S. J. Pennycook, Phys. Rev. Lett. **103**, 097202 (2009).

[29] T. Z. Ward, J. D. Budai, Z. Gai, J. Z. Tischler, Lifeng Yin and J. Shen, Nature Physics **5**, 885 (2009).

[30] A. Moreo, S. Yunoki and E. Dagotto, Science **283**, 2034 (1999).

[31] N. Mathur and P. Littlewood, Physics Today **56**, 25 (2003).

[32] W. Westhäuser, S. Schramm, J. Hoffmann and Ch. Jooss, Eur. Phy. J. B **53**, 323 (2006).

[33] L. Sudheendra, V. Moshnyaga, E. D. Mishina, B. Damaschke, Th. Rasing and K. Samwer, Phys. Rev. B **75**, 172407 (2007).

[34] V. Moshnyaga, L. Sudheendra, O. I. Lebedev, S. A. Köster, K. Gehrke, O. Shapoval, A. Belenchuk, B. Damaschke, G. van Tendeloo and K. Samwer, Phys. Rev. Lett. **97**, 107205 (2006).

[35] L. Sudheendra, V. Moshnyaga and K. Samwer, Contemp. Phys.**48**, 349 (2007).

3. Methodology

All the oxide thin films in this dissertation were synthesized on atomically flat (001) $SrTiO_3$ and $NdGaO_3$ substrates by pulsed laser deposition. This chapter presents the substrate preparation. Most of the samples went through a set of basic characterization methods which will be introduced here as well. High resolution (minimum step size 0.0001°) four-circle X-ray diffraction was used to measure thickness by X-ray reflectivity, in- and out of plane lattice constants which were translated into strain. Rocking curves on substrate and film peaks delivered information about the degree of crystallinity. Atomic force microscopy verified surface roughness or possibly the growth mode (island, layer-by-layer) of the oxide layers. Piezoresponse force microscope, a modified AFM, was used to image ferroelectric polarization.

Depending on the purpose of the samples, they underwent magnetic measurements as a function of temperature and applied magnetic field in a superconducting quantum interference device. Electronic transport properties were investigated by a physical properties measurement system. In order to do the electric characterization, usually device structures needed patterning by photolithography and etching, putting metallic contacts onto samples by radio frequency (RF) sputtering (Pt electrodes), e-beam or thermal evaporation (Cr/Ti + Au).

3.1 Substrate Preparation

One of the most frequently used substrates in this dissertation was (001) oriented $SrTiO_3$ single crystals. They are perovskite type, highly crystalline substrates provided by

CrysTec GmbH or Sinkosha Co., Ltd. (miscut tolerance < 0.05°, grown by the Verneuil process). Its cubic lattice constant a = 3.905 Å is close to most of the thin films' I grew. However one needs to keep in mind that STO undergoes a structural phase transition at around 105 K. It sometimes showed up in electronic transport measurement as a small kink.

STO is a series of SrO and TiO_2 atomic planes. As received, the STO substrate surfaces are quite rough (because of rough polishing agent grain size) and chemically disordered due to SrO segregation.[1] The chemically mixed and uneven surface needed to be flat and single terminated in order to keep good mechanical and chemical interface properties. The single TiO_2 terminated, atomically flat STO surfaces were prepared according to Ref. [2]. The substrates were etched in 1:10 aqueous solution of NH_4F buffered HF for 30seconds. This process is supposed to etch away the excess SrO from the surface. Then they were rinsed in flowing de-ionized water for about 1 minute and dried by pure, pressurized N_2 gas flow. A typical annealing process takes 1 hour at 1050-1100°C in air. This process offers quite reproducible results on substrate slides cut from the same STO wafer; however it often happens that the preparation procedure needs to be altered depending on preliminary surface images, as Figure 3-1 depicts.

Besides surface quality, crystallinity of the substrates has a big influence on the thin film growth. One has to ensure that mosaicity (the rocking angle, in degrees, in both the vertical and the horizontal directions) is kept as low as possible. I inspected every single substrate by X-ray diffraction, e.g. rocking curve scans (see section 3.3.1 for more details) to carefully select the most suitable ones for epitaxial growth.

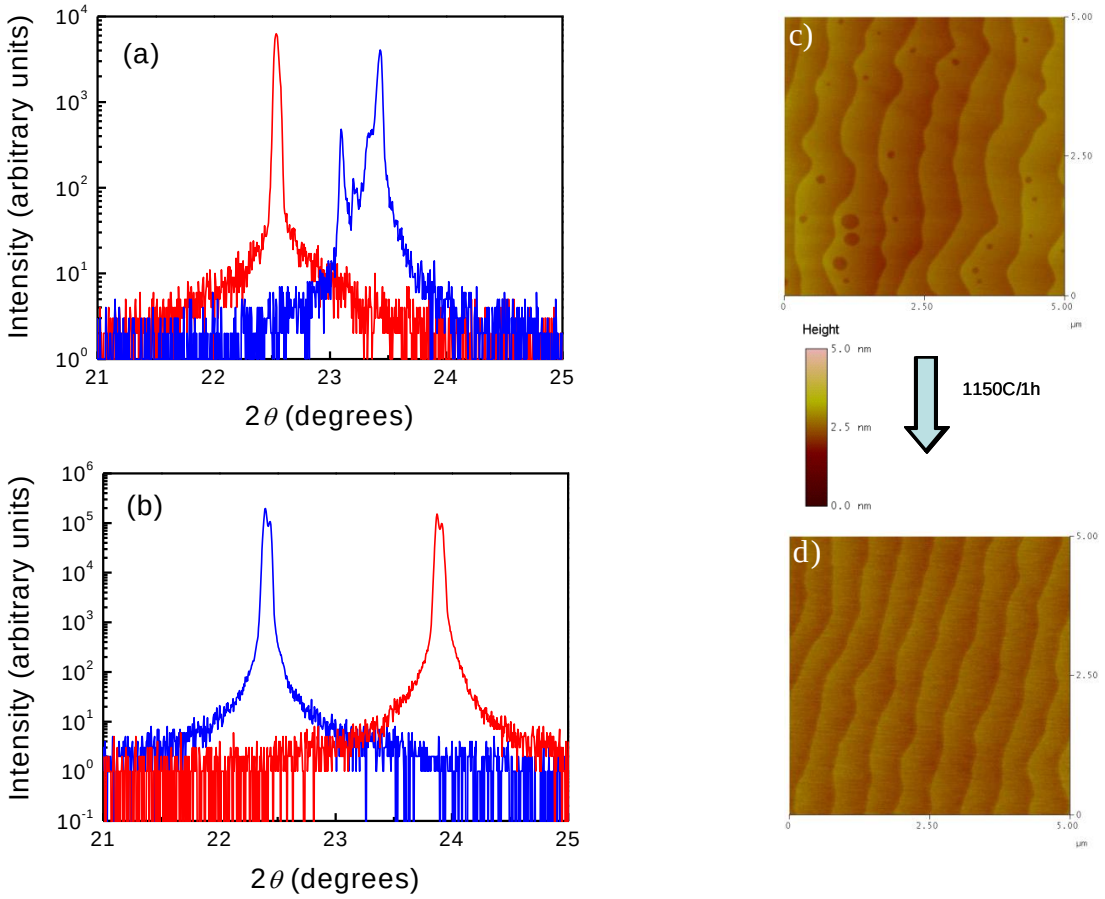

Figure 3-1 Multiple rocking curve peaks imply bad [blue line on (a)] while single ones good [both lines on (b)] crystallinity. The rocking curve scans were taken on STO (002) peak at the azimuth angle $\phi = 0°$ (red) and $\phi = 90°$ (blue). Atomic force microscope (see section 3.3.2) images (5µm × 5µm) were recorded on previously etched then annealed (c) and re-annealed (d) substrates. The latter showed improvement in surface quality.

3.2 Thin Film Deposition by Pulsed Laser Deposition (PLD)

Thin film form of materials has been the subject of intriguing research for almost a half of a century. Integrated circuit technology boosted interest in inventing and developing thin film deposition techniques which provide us with high crystalline quality thin films on numerous substrates. Large scale and highly cost effective deposition techniques are mainly used by academic research as well as private sector R&D departments.

There are various methods out there aiming at supplying thin layers of materials. The most widely used are thermal and electron-beam (E-beam) evaporation, sputtering techniques, plasma-enhanced and low pressure chemical vapor deposition (PECVD, LPCVD), molecular beam epitaxy (MBE) and pulsed laser deposition Table 3.1. In this doctoral research, I used pulsed laser deposition as the tool to produce superior crystalline quality functional oxide thin films, heterostructures, and multilayers on various oxide substrates. This method is quite versatile: many materials can be grown in a number of background gases and pressures. It is a fast, clean, highly energetic (eV) and relatively inexpensive growth technique. In addition, it is easily scalable for potential mass production (Table 3.1).

Table 3.1 The most common thin film deposition techniques and their typical parameters.

Process / Material	Material	Grain Size	Deposition Rate	Substrate Temperature	Cost
Thermal evaporation	Metals / low melting point materials	10-100 nm	1-20 Å/s	50-100 ˚C	Very low
E-beam Evaporation	Metals / dielectrics	10-100 nm	10—100 Å/s	50-100 ˚C	High
Sputtering	Metals / dielectrics	~ 10 nm	1-100 Å/s	~ 200 ˚C	High
PECVD	Dielectrics	10-100 nm	10-100 Å/s	200-300 ˚C	Very high
LPCVD	Dielectrics	1-10 nm	10-100 Å/s	600-1200 ˚C	Very high
MBE	Metals / dielectrics	1nm- 1 cm	1-10 ML*/min	600-1000 ˚C	Very High
PLD	Metals / dielectrics	1 nm–1 cm	0.5-50 ML*/s	500-800 ˚C	Low

*ML stands for monolayer

PLD has been around for quite some years. It is one of the leading techniques to deposit highly epitaxial thin films. After Albert Einstein proposed the concept of stimulated emission, it took more than 40 years to construct the first optical maser utilizing ruby at that time. Early works on laser-solid interactions[3] resulted in the first solid thin film depositions in 1965.[4] The initial films grown by PLD did not produce significant break-through, since they were inferior to those obtained via other deposition techniques, such as chemical vapor deposition (CVD) or molecular beam epitaxy (MBE). After about twenty years PLD was used to grow the first film of the new high temperature superconducting material $YBa_2Cu_3O_{7+\delta}$ (YBCO).[5] This event started the renaissance of PLD. Ever since, high quality metallic, ceramic oxide and oxide multilayers (for a review see for example Ref. [6]), nitride films as well as carbon nanotubes[7] have been grown by PLD.

In a nutshell, PLD basically shines energetic and focused laser beam onto a target material which has exactly the composition as the demanded thin layer (for a nice review see [8]). The substrate is mounted on a heater facing the target. As the laser pulses hit the target, the ablated material flies onto the pre-heated substrate and crystallizes (Figure 3-2). In the case of oxide deposition, the cation stoichiometry is often secured by the target; however oxygen has to be supplied externally. PLD is extremely sensitive to many growth parameters such as laser energy density on the target (later referred to as fluence)[9], growth pressure, background gas, substrate temperature, target-substrate distance, even the oxygen flow's direction and relative position with respect to the target.

The basic setup of our PLD station starts out with a KrF (λ = 248 nm) excimer laser. It is guided to the deposition chamber by using different laser lenses and mirrors. Where the actual growth happens is a relatively small vacuum chamber with a quartz viewport on one side allowing the laser beam to penetrate, since its transmission at this wavelength is about 90-95%[10] and it is transparent in the visible range as well. A rotating carousel accommodates a maximum of 4 target holders. This feature allows us quick ability to switch between targets and so to create heterostructures, superlattices or simply mix multiple materials like a (quasi) co-deposition. Most of the substrates I used are 5mm×5mm which is small enough to keep the film thickness uniform as far as the substrate is about 5-8cm away from the target.

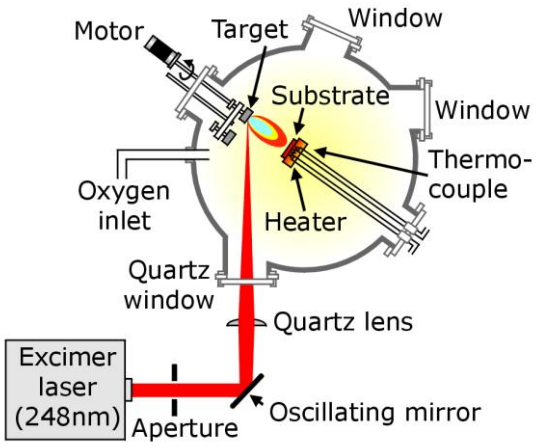

Figure 3-2 Basic pulsed laser deposition setup.

In contrast to the simple hardware setup, PLD is a very complex process. There are four fundamental stages one can distinguish:

a) Laser-target interaction

When focused pulsed excimer laser beam (KrF; λ = 248nm) is shone onto the target with tunable energy at a given repetition rate (typically 5-10 Hz), the laser beam interacts with the target resulting in highly energetic (10-100 keV) plume of ionized species ablated from the target. Above the necessary energy flux density (fluence) and short pulse duration, the target element quickly heat up to their evaporation temperature. Due to the part of the absorbed heat, bonds break inside the target material, and create strongly ionized plasma (plume). Using the right laser fluence (for most of the oxides it is 1-2 J/cm^2), the plume has the target's stoichiometry. The plasma dissociates from the target surface towards the substrate. The ablation mechanism consists of many complex physical phenomena such as thermal ($\hbar\nu < E_b$) and electronic excitations ($\hbar\nu > E_g$, $E_{exciton}$) as well as bond breaking ($\hbar\nu > E_b$).

b) Plume dynamics, gas phase transport

The emitted plasma moves towards the substrate according to the laws of gas-dynamic and shows the forward peaking ~cos(θ) behavior sketched in Figure 3-3. Singh reported[11, 12] that the spatial thickness varied as a function of cos(θ). The spot size of the laser and the plasma temperature has significant effects on the deposited film uniformity. The target-to-substrate distance is another parameter one can control the angular spread of the ablated materials with. The dynamics and composition of the plume are themselves active research topics.[13,14] The plume is highly and multiply ionized set of extremely fast species. It expands adiabatically with a supersonic speed.

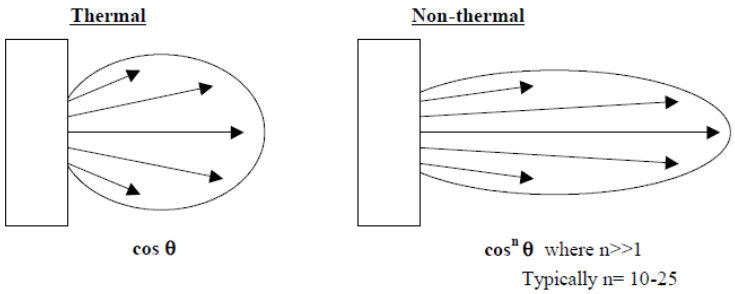

Figure 3-3 Angular dependence of the plume assuming different ablation models.

c) Nucleation and growth of a thin film

The ejected hot and ionized species arrive at the substrate surface and may cause numerous types of damage. These energetic clusters sputter a portion of the surface atoms and a collision layer is formed between the plume and the sputtered atom flow. The film starts growing as soon as a certain thermal equilibrium is reached. The reactive plume

gets deposited onto the heated substrate (for oxides typical growth temperatures are 500-800^{o}C) where it mostly crystallizes immediately.[15]

As mentioned before, PLD opens up a great deal of growth parameter space. In order to optimize the right growth conditions, all those parameters have to be taken into account. In reality, one normally varies the growth pressure, laser fluence and substrate temperature to find the optimum way of growing. An epitaxial film is defined "optimal", if it has a high degree of crystallinity (see section 3.3.1) and certain structural, magnetic and/or transport properties reproduces the bulk ones in the thick film limit (Figure 3-4).

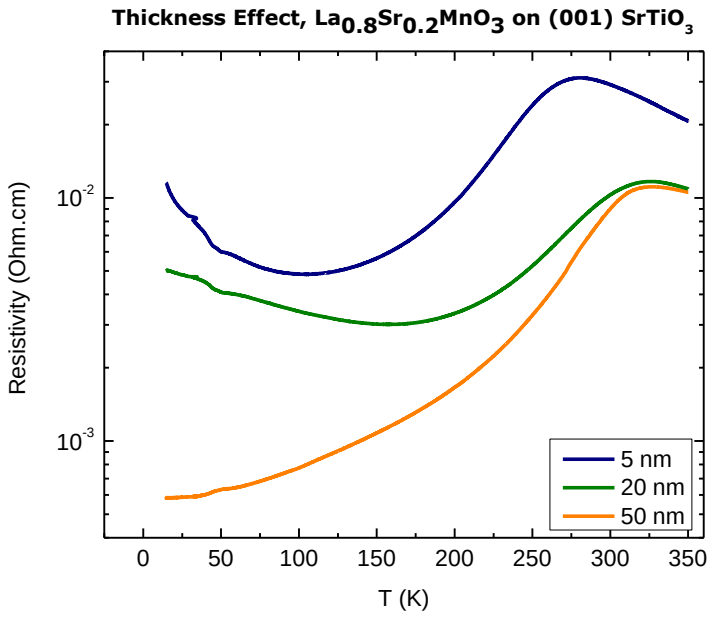

Figure 3-4 Thickness dependence of metal-insulator transition temperature in $La_{0.8}Sr_{0.2}MnO_3$ thin films grown on (001) $SrTiO_3$.

3.3 Thin Film Characterization

3.3.1 Structural characterization

X-ray diffraction (XRD) is a common non-destructive experimental method to structurally characterize materials; in this work mainly thin films. It is a powerful tool to study strain, coherency, multiple structural phases, texture etc. Many properties of complex oxide thin films, such as magnetism and conduction, are correlated with structural features like strain and bond length.[16,17,18]

XRD is a scattering technique. X-rays are generated by an accelerated electron beam bombarding a certain anode material. In our case, it was copper anode with nickel filter (anodes and Kβ filters listed on Table 3.2); the accelerating voltage is 30-45 keV. The copper anode emits photons with a characteristic wavelength of 1.54 Å. These waves are reflected by atomic planes of the thin film and substrate according to Bragg's law. The spacing between the reflecting planes can be derived from Bragg's law as:

$$d_{hkl} = \frac{a_0}{\sqrt{h^2 + k^2 + l^2}} \tag{3-1}$$

Here (*hkl*) denote the Miller indices of the reflecting planes, a_0 is the lattice parameter while d_{hkl} is the interplanar distance, which is in close relationship with the scattering angles one observes total reflections.

Table 3.2 X-ray generating anodes with the corresponding wavelengths and Kβ filters.

Anode	(kV)	Wavelength (Å)	Kβ-Filter
Mo	20.7	$K\alpha_1$: 0,70926 $K\alpha_2$: 0,71354 $K\beta_1$: 0,63225	Zr 0,08mm
Cu	9.0	$K\alpha_1$: 1,5405 $K\alpha_2$: 1,54434 $K\beta_1$: 1,39217	Ni 0,015mm
Co	7.7	$K\alpha_1$: 1,78890 $K\alpha_2$: 1,79279 $K\beta_1$: 1,62073	Fe 0,012mm
Fe	7.1	$K\alpha_1$: 1,93597 $K\alpha_2$: 1,93991 $K\beta_1$: 1,75654	Mn 0,011mm

The same law can be formulated in reciprocal space. If $\boldsymbol{k_0}$ is the incident and $\boldsymbol{k}$ is the diffracted beam's wave vector, a constructive diffraction pattern happens in case

$$\vec{k} - \vec{k}_0 = \vec{G} \tag{3-2}$$

$\boldsymbol{G}$ is a reciprocal lattice vector of the substrate / film. Bragg's law is illustrated in Figure 3-5).

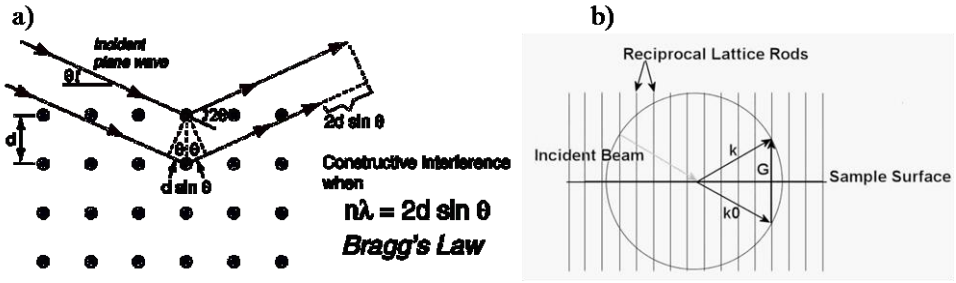

Figure 3-5 Illustration of Bragg's Law in real (a) and reciprocal space (b).

Using this law and XRD one can map a set of reflecting planes in the film depending on the experimental setup and orientations. Using certain databases one can identify extra (mostly undesired) phases or the strained/relaxed thin film's crystal symmetry (see Figure 3-6).

To structurally characterize the films I grew, I used an X'Pert Pro X-ray high resolution four-circle diffractometer by Philips. It uses Cu Kα radiation to probe the layers. Slits were utilized to reduce the beam size. The incoming X-ray interacts with the sample, mostly epitaxial thin films, bi- or multilayers, and gets reflected into a semiconductor detector.

There are some special setup features thin film XRD requires. First, reflection geometry is used instead of transmission which is illustrated on Figure 3-6. The reason is the substrate is much thicker (on the order of millimeters) than the films. Therefore, the background coming from it would completely suppress the film peaks.

The basic thin film characterization include the determination of in-plane and out-of-plane lattice constants, degree of crystallinity/disorder by rocking curve scans on thin film peaks, confirmation of superlattice periods and find out thickness by glancing incident X-ray reflectivity (Figure 3-6).

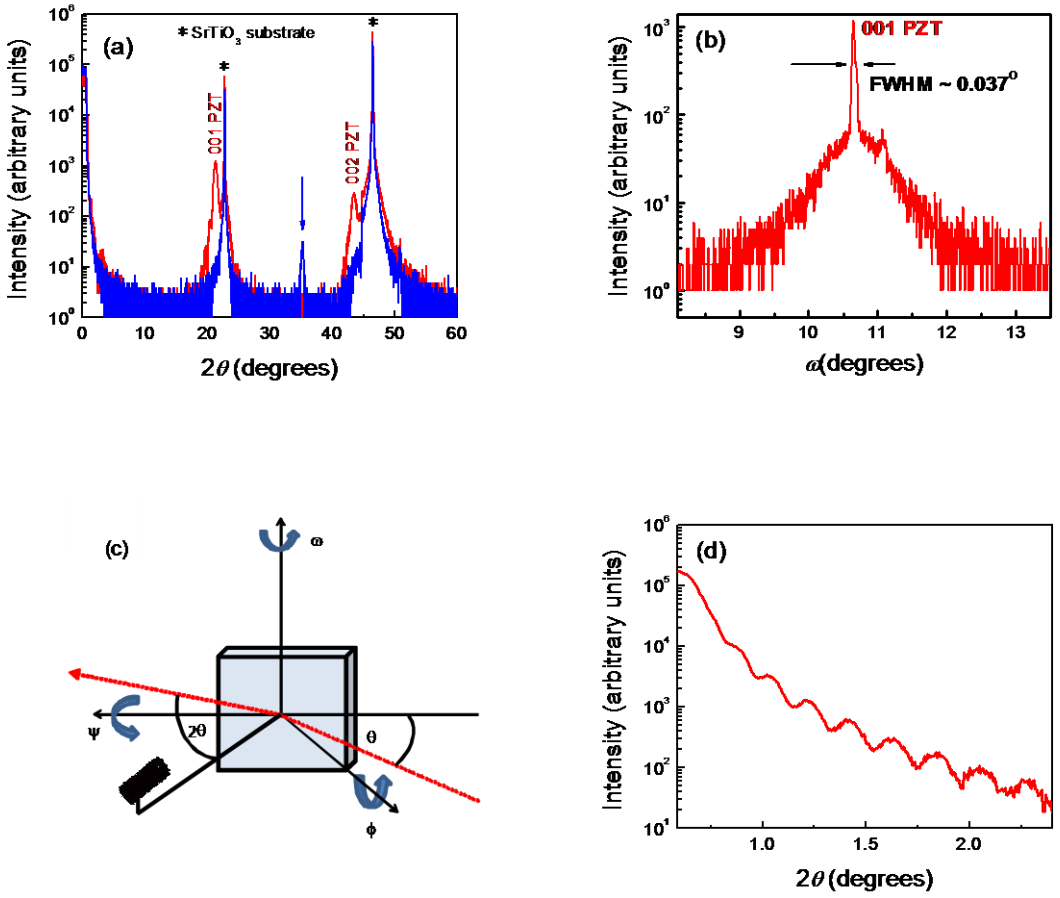

Figure 3-6 Illustration of the four-circle diffraction setup with the angles I used (c). θ-2θ scans (a) of two, nominally 30 nm thick PZT films on (001) STO reveal a nice perovskite (red) and an undesired pyrochlore growth. The perovskite (002) thin film peak reveals high degree of crystallinity through sharp rocking curve of 0.037° (b), which is comparable to the substrate. (d) shows clear thickness fringes coming from a 55 nm thick $LaMnO_3$ thin film.

Another useful feature this machine has to offer is reciprocal space mapping (Figure 3-7). It is utilized to get information about the film's and the substrate's relative orientation, ergo the degree of epitaxy. This is a measurement using a set of θ-2θ scans as changing the ω angle. The data set can be converted to reciprocal space co-ordinates by

$$s_x = \frac{q_x}{2\pi} = \frac{1}{\lambda}\{\cos\omega - \cos(2\theta - \omega)\}$$
$$s_z = \frac{q_z}{2\pi} = \frac{1}{\lambda}\{\sin\omega - \sin(2\theta - \omega)\} \quad (3\text{-}3)$$

With these maps one can calculate in-plane and out-of-plane lattice parameters as well as judge the degree of epitaxy, strain or relaxation in the film.

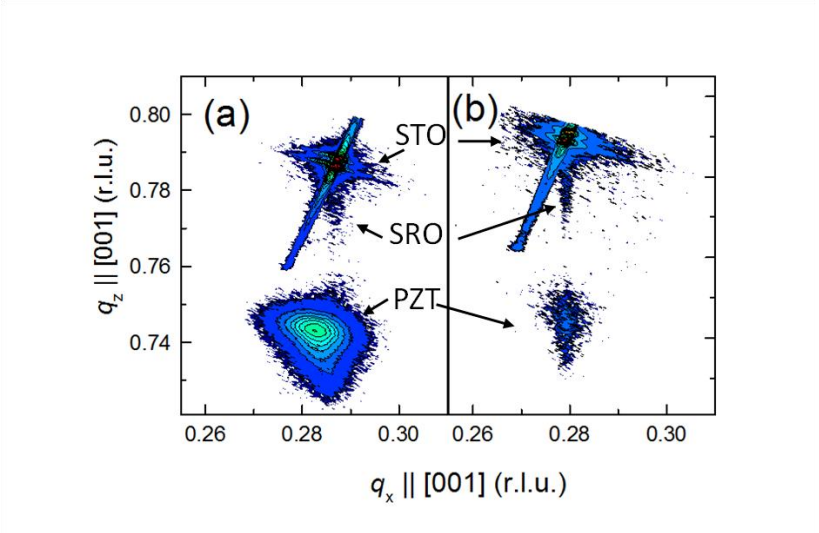

Figure 3-7 Reciprocal space maps of a thicker (100nm), partially relaxed PZT film, compared to a thinner (30nm), well-strained one. Both were grown on 5nm $SrRuO_3$ / (001) $SrTiO_3$.

3.3.2 Scanning Probe Microscopy

Atomic force microscopy (AFM) (See Figure 3-8) is a powerful scanning tool to probe surface quality.

Binnig and Rohrer's invention,[19] the atomic force microscope was constructed of a diamond shard glued to a piece of gold foil. The diamond tip contacted the surface, and used the van der Waals forces to image surfaces. Detection of the cantilever's vertical movement was done with a second tip. Today's AFM cantilevers can be down-sized to microns while the tip curvature measures a couple of nanometers.

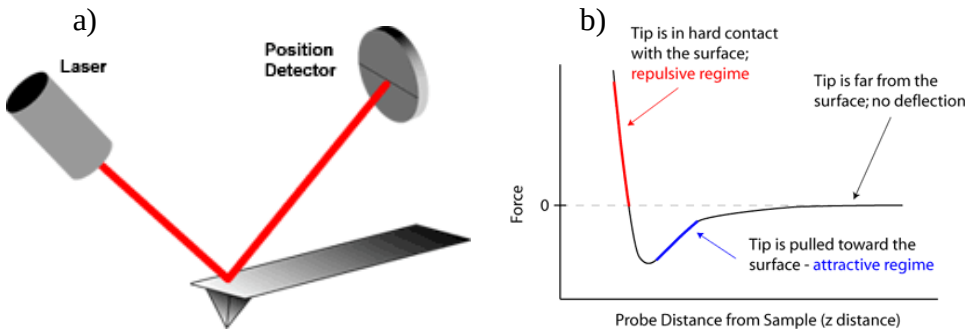

Figure 3-8 Atomic force microscopy operating principles.

The basic setup consists of a reflecting cantilever, a laser source and a photodiode As the cantilever is lowered to the surface, it bends according to the interaction between the tip, and sample. As a result the cantilever deforms and deflects. This deflection is detected by set of photodiodes looking at the reflected laser light by the cantilever. The photodiodes' signal can be transmitted to a computer for further data processing.

AFMs have several imaging modes depending on the quantity and the nature of interaction one uses to image (Table 3.3).

Table 3.3 Atomic force microscopy imaging modes

Lateral Force Microscopy (LFM) • measures frictional forces on a surface	***Noncontact mode*** • Oscillating stiff cantilever not touching the sample surface. • Forces on the order of pN.
"tapping mode" AFM • A stiff cantilever oscillating closer to the sample than in noncontact mode. Part of the oscillation extends into the repulsive regime, so the tip intermittently "taps" the surface.	***Force Modulation*** • Oscillating at a high frequency and pushed into the repulsive regime. • The slope of the force-distance curve is measured which is correlated to the sample's elasticity. • The data can be acquired along with topography, which allows comparison of both height and material properties.
Phase Imaging • The phase shift of the oscillating cantilever relative to the driving signal is measured. • The phase shift can be used to differentiate areas on a sample with such differing properties as friction, adhesion, and viscoelasticity.	

For our topographic studies (Figure 3-9) I used an "advanced noncontact" mode called **tapping (dynamic force) mode**, in order to preserve the tip. In this mode a stiff cantilever oscillates close to the sample, (unlike in the case of contact mode) partially in the repulsive regime .A kHz range oscillation amplitude greater than 20 nm is induced by a piezoelectric crystal. The cantilever's resonant frequency is kept constant while the change in either the amplitude/ resonant frequency/phase detected and interpreted as different surface features or surface specific quantities. We used AFM technique to

ensure substrates' surface qualities (see Figure 3-1), atomic step heights, terrace widths as well as film smoothness and growths modes (Figure 3-9)

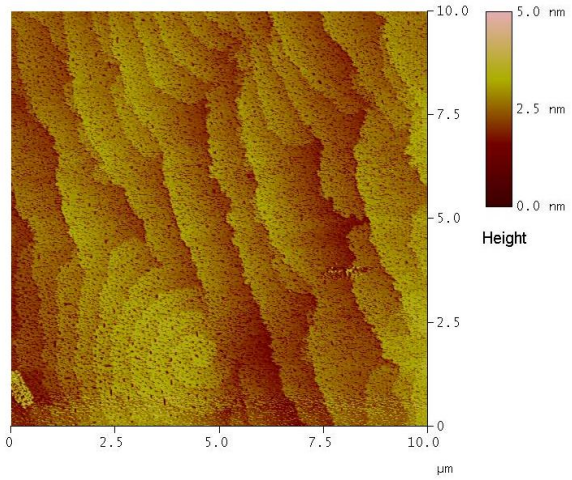

Figure 3-9 60nm $SrRuO_3$ on (001) $SrTiO_3$ substrate. A screw dislocation is captured possibly originating from the substrate inherited by the film. The scan area is 10µm × 10µm

The **piezoresponse force microscopy** (PFM) configuration consists of a modified AFM with a lock-in amplifier as depicted in Figure 3-10. A set of materials, such as piezoelectrics, can produce certain electromechanical response which can be detected by a stiff and biased AFM cantilever (see for example [20]). Due to the applied *AC* potential difference between the scanning tip and the sample surface, the piezoelectric sample will be locally deformed which results in tip deflection depending on the piezoelectric constant.

The coupling between an external electric field and the induced strain in the material is described by a third rank piezoelectric tensor. Its d_{33} component becomes relevant if a (001) oriented film is scanned by a conventional vertical PFM.

The applied bias of

$$V_{tip} = V_{dc} + V_{ac}\cos(\omega t) \tag{3-4}$$

results in a strain which leads to the tip's deflection described by

$$z = z_{dc} + A(\omega, V_{ac}, V_{dc})\cos(\omega t + \varphi) \tag{3-5}$$

If the driving voltage is running far below the contact resonance frequency of the tip, the expression becomes

$$z = d_{33}V_{dc} + d_{33}V_{ac}\cos(\omega t + \varphi) \tag{3-6}$$

It shows that the oscillation amplitude is a measure of the vertical piezoelectric constant while the phase determines the underlying polarization direction.

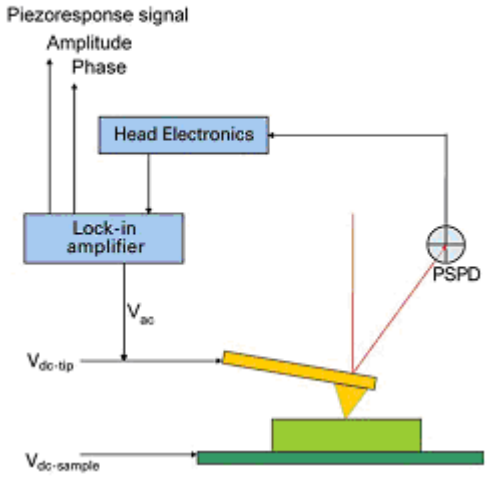

Figure 3-10 Basic setup of a piezoforce microscope.

The first and second harmonics can be extracted with the lock-in amplifier and utilized to map local vertical piezoelectric response of the sample. In order to get reliable signal, this technique requires samples with quite large d_{33}. One can even exploit the small *dc* voltage superposed onto the *ac* bias to gain information on local hysteresis loops.[20]

3.3.3 Magnetic and Transport Characterization

Magnetic properties of thin films, bi-layers and superlattices were measured by superconducting quantum interference devices (SQUID). Quantum Design's MPMS XL offered a wide range of temperature and magnetic field coverage to explore magnetic moments as a function of temperature (5-350K) and external magnetic field (1-7 Tesla). Since mostly thin film structures were tested, extreme sensitivity is a must so that the limited thin film signal can be extracted on the top of a usually large substrate background moment.

The dc-SQUID I used consists of two Josephson junctions, which are connected parallel in a superconducting loop. The junctions reduce the critical current of the loop with respect to the superconducting parts. The wave functions in the two superconducting regions are related by a phase factor only. This way, if there is a changing magnetic flux going through the loop, the voltage drop across the junctions will be integer multiples of $\Phi_0 = h/2e = 2 \times 10^{-7} G\ cm^2$ magnetic flux quantum. Keeping a constant (super-) current passing through the junctions, the voltage will be periodic in Φ with a step of Φ_0 (Figure 3-11).

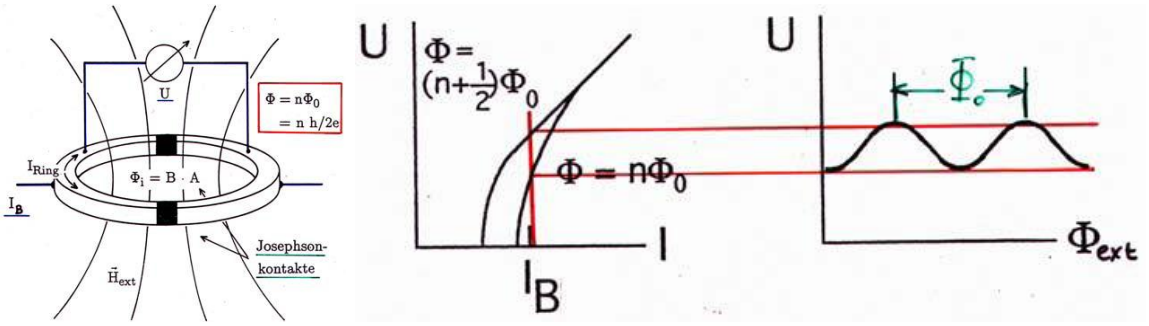

Figure 3-11 The concept of SQUID is based on a pair of Josephson junctions. In a constant current mode voltage oscillations are counted to measure the magnetic moment in Φ_0 units.

As the sample is pushed through the coil the SQUID takes several voltage points along the sample travel. Even if an external magnetic field is applied, for example to measure *M(H)* loops, the field is homogeneous enough not to alter the signal coming from the sample. The voltage-position data are fitted by a simple dipole model going through a coil. Sometimes the signal coming from the film needs to be enhanced by a small applied magnetic field. Depending on the material 100-2000 Oe field is low enough (1000 Oe in Figure 3-12, which is less than the saturation magnetization) to have clear signal. Samples were measured in the temperature range of 2–350 K. The largest field available was 7 Tesla.

Most correlated electron oxide systems display numerous electronic phases which are often related to the magnetism. Those phases usually show up at low temperatures or in applied magnetic field. The Quantum Design Physical Properties Measurement System (PPMS) model 6000 enabled us to investigate DC electronic transport properties like conductivity and charge carrier density as a function of temperature, magnetic field or magnetic field direction by using a sample rotator. The maximum magnetic field

applicable was 14T. The usual temperature range was 5 – 400 K the instrument can reach in standard mode while it can be cooled down to about 0.5 K using the He-3 option.

Figure 3-12 shows *M(T)* and *M(H)* data taken by SQUID (red lines) while *R(T)* by PPMS measurement monitors metal-to-insulator transition in a 50 nm thick $La_{0.8}Sr_{0.2}O_3$ film grown on (001) STO substrate (blue line). Conduction and magnetism are strongly coupled in manganites and it is nicely visualized by the close transition temperatures.

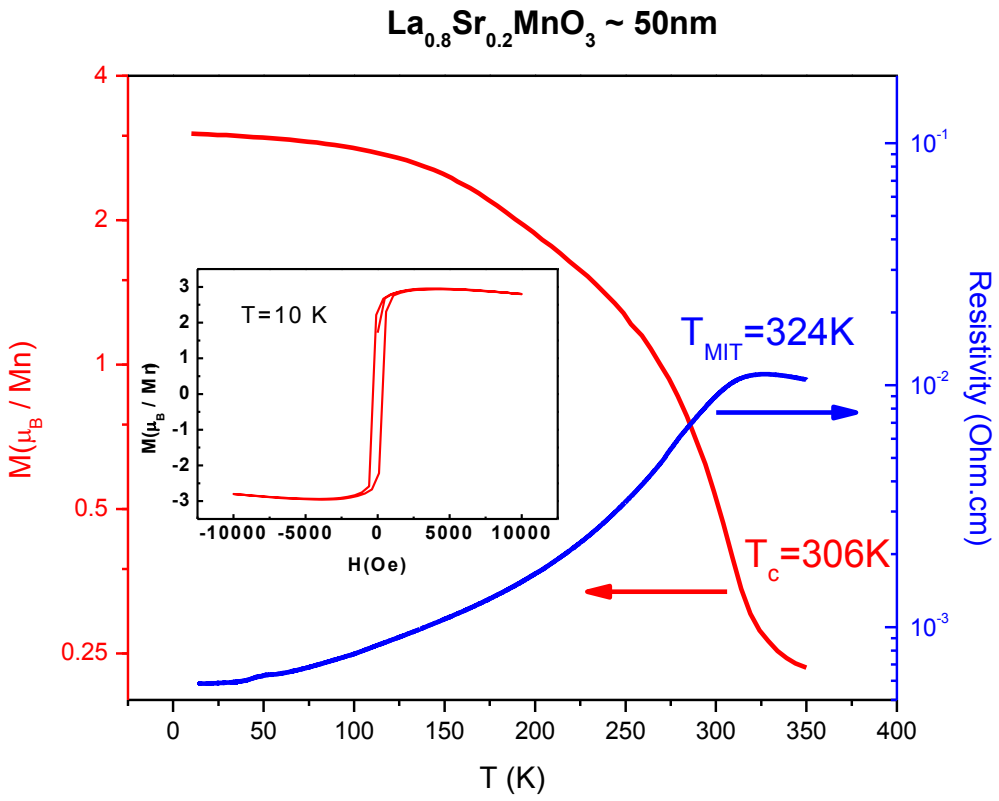

Figure 3-12 Metal-insulator transition (MIT) and ferromagnetic-paramagnetic transition measured by PPMS and SQUID, respectively. The inset show a sharp ferromagnetic *M(H)* loop at low temperature.

3.3.4 Photolithography, Etching and Metallization

I used different measurement geometries throughout this work to get the desired information on electronic transport properties. Sometimes $La_{1-x}Sr_xMnO_3$ devices were needed to define on a ~ 100-500 μm scale. The fastest available method to define spatially confined structures was photolithography. I spin coated the samples by a positive photoresist (PR) polymer (S1813 by Microposit) using 5000 RPM for 1 minute. After pre-baking at 120°C for another minute, I placed the sample on a wafer aligner station by Hybrid Technology Inc. The aligner used a 350W UV lamp (λ = 365 nm). The PR coated samples were illuminated by UV light for 9-13s depending on film thickness, index of refraction of the film and/or the substrate. A one minute post-baking at 120°C was followed by the development process. I used CD-26 developer by Microposit for about 1-2 minutes. Depending on the purpose, the micro-devices were either defined by etching or ready for the next metallization procedure.

The photoresist layer reacts with the UV light. A photolithography mask is applied to define the demanded geometry. It is basically a glass slide coated with a certain metal which absorbs UV light. After illumination and post-exposure bake the developer reacts with the illuminated and now soluble parts of the PR layer leaving a well-defined pattern (illustrated on Figure 3-13).

Etching LSMO thin films were done by a HCl : HNO_3 : H_2O = 1 : 1 :1(volume fraction) solution. The high concentration of HCl led to active Cl_2 gas evaporation, which started etching the sample when approaching the etchant. Due to this phenomenon and the extremely quick etch rate, the mixture had to be diluted with water 1:4. The etching rate (finally about 12 nm/s) was carefully monitored by using AFM on the border

between the etched and pristine parts of the film. This etchant turned out to be selective, not bothering the usually underlying STO substrate or PZT film. The same effect can be reached by using KI solution.

The metallization was done by different methods. Platinum and gold were mostly *RF*-sputtered. Earlier electron-beam and thermal evaporation techniques supplied Cr/Ti adhesive layer between the oxide and the top gold electrode.

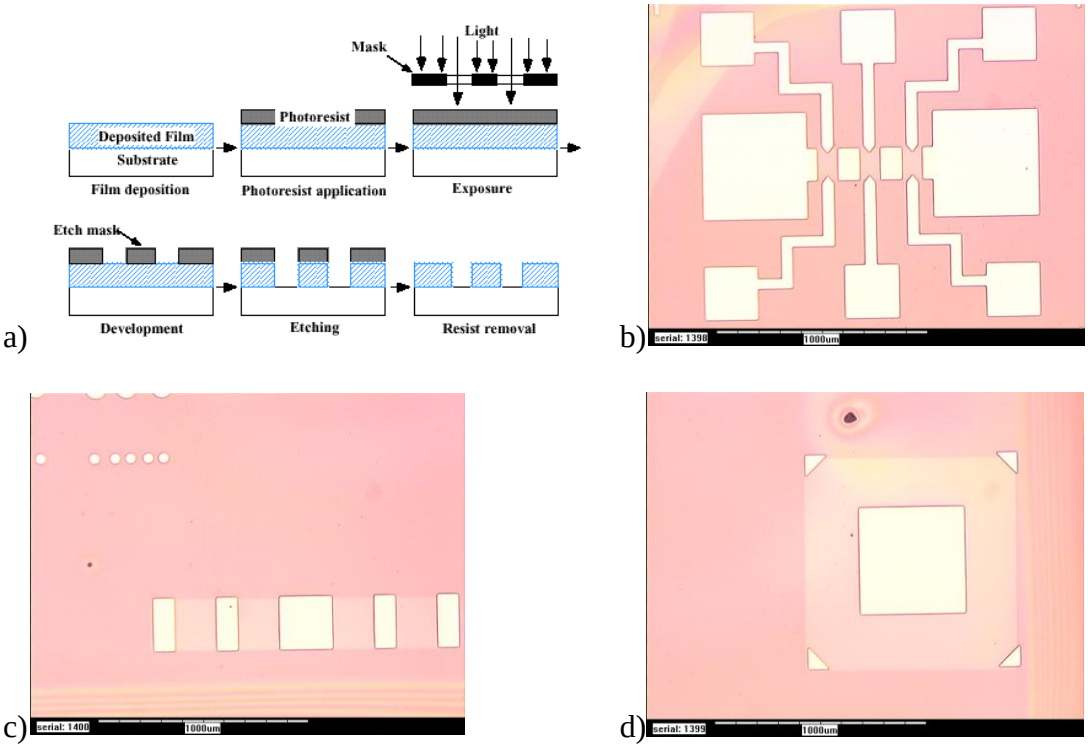

Figure 3-13 Basics of optical photolithography (a) and some examples of the devices used. Hall bar (b), 4-point probe (c) and van der Pauw device (d) with top (gate) electrodes enabling transport measurements under external bias.

References

[1] V.E. Henrich, and P.A. Cox, *The Surface Science of Metal Oxides*, Cambridge University Press, Cambridge, 1994.

[2] M. Kawasaki, *et al.*, *Science* **266**, 1540 (1994).

[3] F. Breech, L. Cross, Appl. Spectrosc. **16**, 59 (1962).

[4] H.M. Smith, A.F. Turner, Appl. Opt. **4,** 147 (1965).

[5] D. Dijkamp, T. Venkatesan, X.D. Wu, S.A. Shaheen, N. Jisrawi, Y.H. Min-Lee, W.L. McLean, M. Croft, Appl. Phys. Lett. **51**, 619 (1987)

[6] J. Shen, Z. Gai, J. Kirschner, Surface Science Reports **52**, 163 (2004).

[7] H. M. Christen, A. A. Puretzky, H. Cui, K. Belay, P. H. Fleming,D. B. Geohegan, and D. H. Lowndes, Nano Lett. 4(10), 1939 (2004).

[8] H. M. Christen and G. Eres, J. Phys.: Condens. Matter. **20**, 264005 (2008).

[9] T. Ohnishi, M. Lippmaa, T. Yamamoto, S. Meguro, and H. Koinuma, Appl. Phys. Lett. **87**, 241919 (2005).

[10] D. J. Krajnovich, I. K. Pour, A. C. Tam, W. P. Leung, and M. V. Kulkarni, Optics Letters **18**(6), 453 (1993).

[11] Singh, R.K., O.W. Holland, and J. Narayan, Journal of Applied Physics **68**(1), 233 (1990).

[12] Singh, R.K. and J. Narayan, Physical Review B. **41**, 8843 (1990).

[13] D. B. Geohegan and A. A. Puretzky, Appl. Phys. Lett. **67**, 197 (1995).

[14] S. S. Harilal, C. V. Bindhu, M. S. Tillack, F. Najmabadi, and A. C. Gaeris, J. Appl. Phys. **93**, 2380 (2003).

[15] Eres, G., et al., Applied Physics Letters **80**(18), 3379 (2002).

[16] A. J. Millis, T. Darling, and A. Migliori, J. Appl. Phys. **83**, 1588 (1998).

[17] P. Murugavel, J. H. Lee, Jong-Gul Yoon, T. W. Noh, J.-S. Chung, M. Heu, and S. Yoon, Appl. Phys. Lett. **82**, 1908 (2003).

[18] K. H. Ahn, T. Lookman and A. R. Bishop, Nature **428**, 401 (2004).

[19] Binnig, G., C.F. Quate, and C. Gerber, Physical Review Letters **56**, 930 (1986).

[20] Gruverman, A., O. Auciello, and H. Tokumoto, Applied Physics Letters **69**(21), 3191 (1996).

4. Control of Stoichiometry in $LaMnO_3$ Thin Films

This chapter is about the extensive and systematical structural, magnetic, optical and transport study on $LaMnO_3$ (LMO) thin films grown on $SrTiO_3$ (STO). While the stoichiometric LMO is an insulating antiferromagnet, they tend be ferromagnetic insulators when grown as thin films. By exploring the majority of growth parameters, it was found that the bulk-like electronic and magnetic phases can be stabilized by growing thin films under reducing atmospheres and by using more energetic laser processes. Since oxides are prone to reduce the oxygen content and to alter the cation ratio under such growth conditions, it suggests that the cation and/or oxygen stoichiometries in LMO films can be modified by properly controlling the growth parameters.

4.1 Introduction

Perovskite oxides are fascinating materials exhibiting many intriguing physical properties. Especially, in strongly correlated electron oxides, interactions between charge, spin, and lattice degrees of freedom are complex, and various order parameters compete against each other, resulting in a complex phase diagram.[1,2] Among them, rare-earth manganites (RMnO$_3$) and their chemically doped derivatives are the most widely studied perovskites due to many useful properties and behaviors, including the colossal magnetoresistance[3] and magnetoelectric coupling.[4,5] Since strongly correlated electrons in RMnO$_3$ generate a large variety of competing ground states in bulk, incorporating them

in heterostructures provides with additional opportunities for creating novel phenomena at interfaces. Therefore, synthesizing them in thin film form offers additional degree of freedom. Furthermore these oxides' structures can be engineered by, for example, epitaxial strain and multilayering for manipulating and enhancing their properties. Despite the huge potential mentioned above, the clear understanding of the physical properties of $LaMnO_3$ - based heterostructures has been challenged by the difficulty in achieving the bulk-like magnetic ground state, i.e., A-type antiferromagnetism (AFM), in LMO thin films. Most LMO thin films, regardless of the growth method, exhibit ferromagnetic (FM) insulating behaviors. Therefore, exploring the intrinsic properties of interface-engineered heterostructures using LMO is hindered by the uncertainty of magnetic ground state, although there are many interesting modifications of physical properties by interfacing materials with dissimilar electronic and magnetic configurations.[6,7,8,9,10,11,12]

LMO has the structure of a rhombohedral perovskite with corner sharing MnO_6 octahedra.[13] The partially occupied 3d electron spins order at $T_N \approx 140$ K resulting in a layered (A-type) AFM ground state as illustrated in Figure 4-1. Its ability to accommodate excess oxygen with good ionic conductivity makes it a promising candidate for solid oxide fuel cell cathodes.[14] While bulk and thin film forms of doped manganites ($La_{1-x}A_xMnO_3$) have attracted a lot of attention due to their intriguing properties, i.e. colossal magnetoresistance (CMR). Artificially stacked multilayers based on recent advances in atomic-scale synthesis of correlated electron oxides are of particular interest due to the potential for inducing new unprecedented material classes by manipulating spin and charge alignments across the interface.

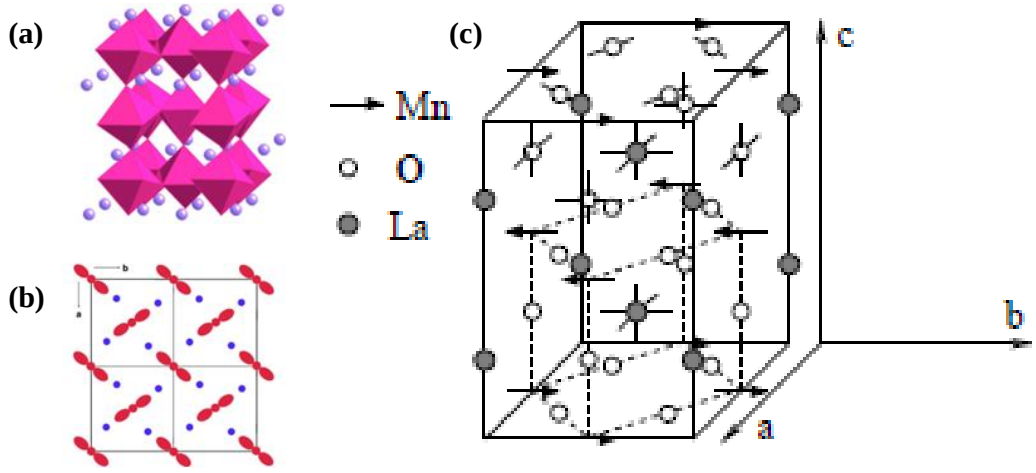

Figure 4-1 $LaMnO_3$ is built of MnO_6 corner-sharing and tilted octahedra separated by La ions (a). $d_{x^2-r^2}$/ $d_{y^2-r^2}$ orbitals are ordered in the *ab* plane in a checker-board pattern (b) (Ref. [15]) leading to in-plane ferromagnetism and antiferromagnetic coupling between *ab* planes (c) (Ref. [16]).

However, growing epitaxial thin films with the AFM ground state is always challenged by the difficulty in achieving the right stoichiometry. It was found that thin films grown in high oxygen pressures show mostly FM behaviors in their as grown state, but still remain as insulators contradicting to some reported results[17]. Such off-stoichiometry has been found to originate from La and Mn vacancies that result in excessive oxygen[18] and from La deficiency.[19] Moreover, the epitaxial strain induced by the lattice mismatch between the film and the substrate also can be a reason for the FM state.[20]

4.2 Pressure Dependent Study

4.2.1 Sample Preparation and Crystal Structure

In order to get rid of excess oxygen, a series of 60 nm epitaxial $LaMnO_3$ thin films was grown on atomically flat (001) $SrTiO_3$ single crystal substrates (cubic, a = 3.905 Å) by pulsed laser deposition (PLD) using a KrF (λ = 248 nm) excimer laser. The thickness was carefully chosen such that the films remain strained but still provide good signal for the characterization measurement. The substrates were etched before deposition with buffered HF solution to ensure a single TiO_2-terminated surface (see Section 3.1 for details). The growths were done at 600 °C in oxygen pressures of 0.01-400 mTorr, which were optimized based on full width at half maximum in X-ray diffraction (XRD) rocking curve ω scans. The film quality is demonstrated by diffraction and AFM measurements in Figure 4-2. The lack of extra film peaks between two main substrate peaks is the sign of single phase films. Rocking curves are always less than 0.05°.

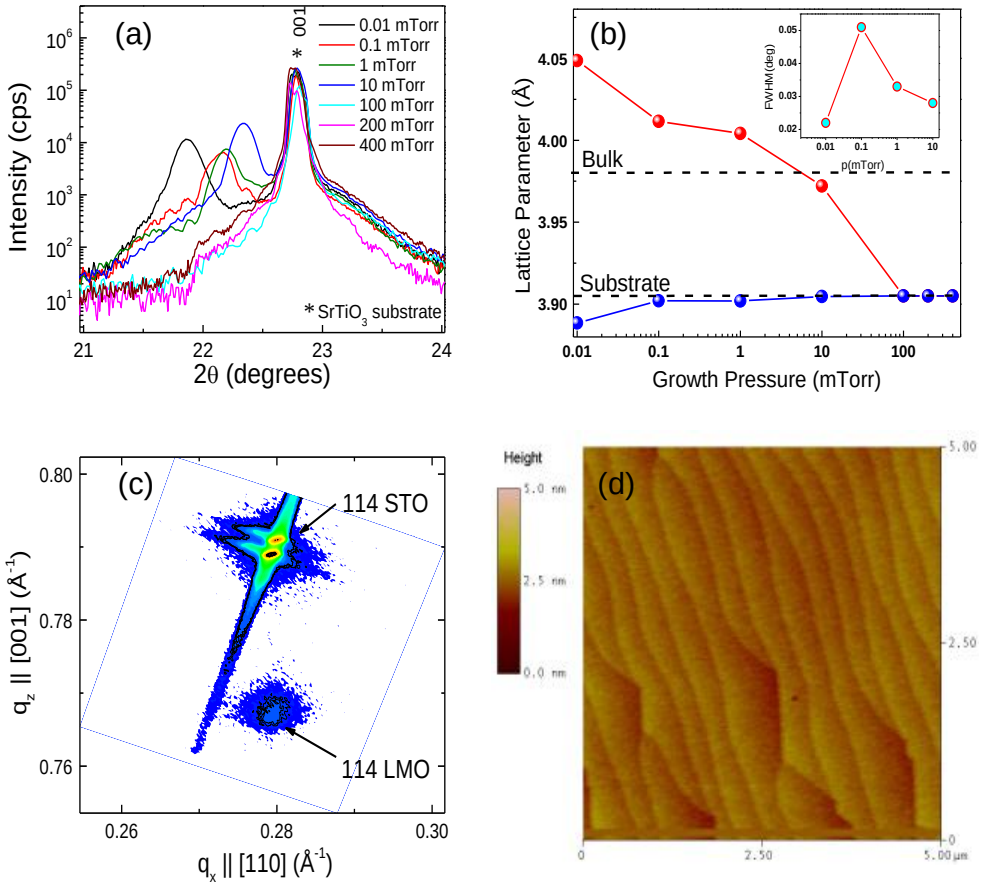

Figure 4-2 (a) θ-2θ scans (a) on 60 nm LMO films grown in various oxygen pressures show collapsing lattice as the pressure increases (b). The degree of crystallinity, depicted by the inset, proves superior crystallinity. The RSM on the 0.1 mTorr growth (c) illustrates fully strained, epitaxial layer. The AFM image on the same sample demonstrates perfect flatness (d) (Marton, unpublished).

As the oxygen pressure is increase in the growth chamber while growing, the lattice collapses gradually, which indicates more and more tilted oxygen octahedra. At the low pressure end and the lattice constant is clearly much more than it is expected (*cf.* bulk value on Figure 4-2 (b)). It is likely, that the low pressure induced oxygen vacancies induce cation vacancies to compensate electronic charges in the structure. It is important

to know, though, which cation's stoichiometry is altered, so that the off-stoichiometry can be later fixed. It was shown, that oxygen off-stoichiometry in bulk was accommodated as cation vacancies.[21,22] As such, the composition can be written as $La_xMn_xO_3$, with

$$x = \frac{3}{3+\delta} \tag{4-1}$$

This nomenclature means that excess oxygen leads to cation vacancy while oxygen deficient LMO is a good host of extra cations.

4.2.2 Magnetism and Electronic Transport

Let us accept that the perovskite structure topologically unable to accommodate excess oxygen and over oxygenation can result in $LaMn_xO_3$ or La_xMnO_3 phases. In fact, these two kinds of deviations behave differently as far as magnetic transition temperatures are concerned. Losing manganese ions means that the number of the magnetic interactions' centers is lowered. Therefore, T_C goes down. However, lanthanum deficiency leads to raising T_C which can be explained by the opening Mn-O-Mn angles or hole doping (see Figure 4-3).

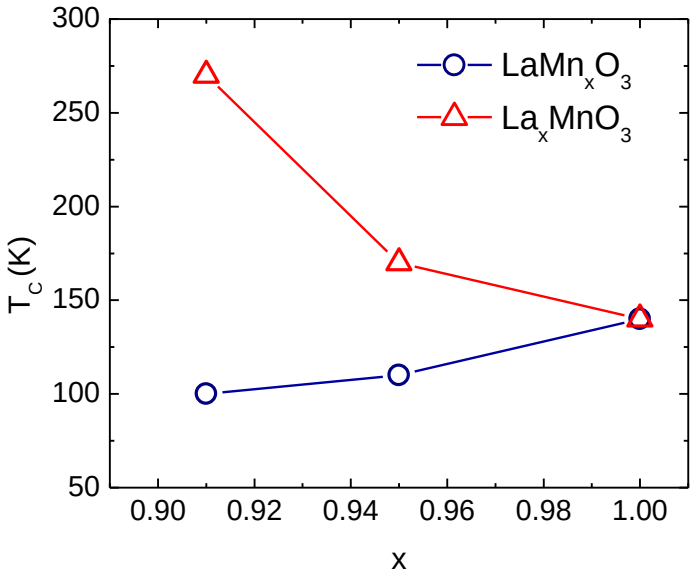

Figure 4-3 Magnetic transition temperatures of bulk LMO crystals with varying cation stoichiometries (adopted from Ref. [23]).

Since magnetism and electronic transport are very much coupled in most doped transition metal oxides; I carried out a systematic study on these properties as a function of growth pressure. The idea was to get δ in (4-1) as close to zero as possible this way to improve cation stoichiometry as well as arriving at true ferromagnetic *ab* planes.

I tested the set of samples characterized above (Figure 4-2) in a Quantum Design Magnetic Properties Measurement System (Section 3.3.3). *M(T)* scans were taken in 2 kOe external field to improve the signal quality. Way below the magnetic transition temperature, at 10 K, I recorded *M(H)* loops to investigate how coercivity depends on reduced oxygen content.

The magnetic hysteresis loops show clear change in shape, remanence and coercive fields as shown in Figure 4-4. It seems like growing in low oxygen pressure is a quite efficient tool to reduce undesired ferromagnetic correlations.

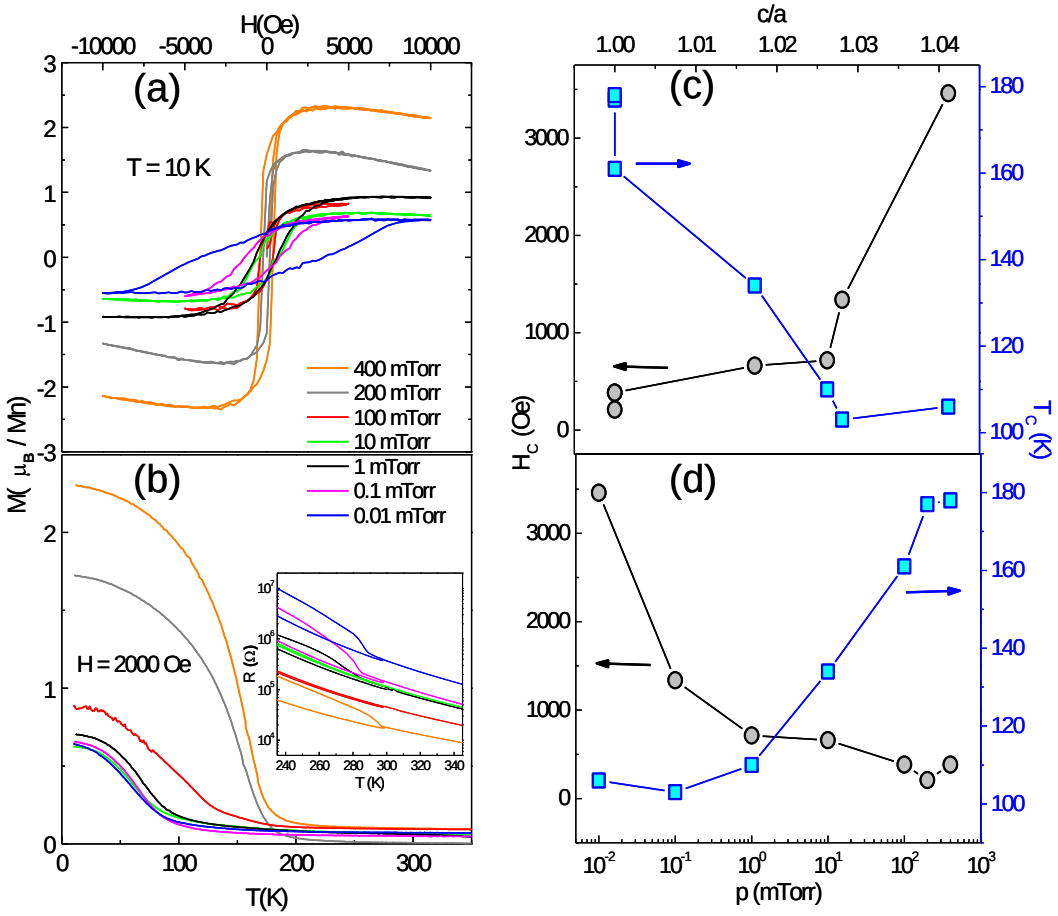

Figure 4-4 Magnetic data taken on 60 nm LMO thin films. *M(H)* loops at 10 K (a) display significant magnetic hardening due to lower growth pressure. Magnetization curves (b) clearly show reduction in the net magnetization and T_c as more oxygen is depleted and a corresponding resistance increases (inset). Coercive field (H_c) and T_c are depicted (c-d) as functions of growth pressure (d) and the corresponding tetragonality (c), *e.g. c/a* (Marton, unpublished).

The low temperature net magnetization is lowered dramatically. T_c and the coercive field H_c behave complementarily in Figure 4-4 (c-d).

The electronic transport data is a little bit puzzling. Resistances in this range indicate that there still is a substantial deviation from the right stoichiometry. Increasing oxygen pressure turns the films more conductive but they all remain semiconductor in nature with the same band gap of about 0.13 eV. It means that oxygen-rich growth atmosphere creates more conducting sites, *e.g.* Mn^{4+}-O-Mn^{3+} links whose number grows with growing pressure but they do not percolate. No semiconductor-to-metal transition is observed. A possible explanation, combining the data above, is that the extra oxygen ions help to create lanthanum-deficient sites. Because of charge neutrality, electrons from the manganese e_g orbits disappear (hole doping) resulting in ferromagnetically ordered and locally conductive sites.

4.2.3 Conclusions

The structure and magnetization of $LaMnO_3$ thin films can be modified by varying the oxygen growth pressure when using PLD. While the lattice seems to be collapsing with increasing pressure, *Tc* grows suppressing the resistivities. Instead, ferromagnetism appears rapidly already at low O_2/Ar ratios. H_c drops with growth pressure and eventually saturates at high O_2 background. There was no metal-to-insulator transition (MIT) observed but hysteresis was detected in the electronic transport data between the heating and cooling cycle probably due to low temperature current heating. The lack of MIT may indicate that the cation off-stoichiometry is small.

4.3 Reduction by Post-Annealing

Independent studies (see for example Ref. [24]) reported that post-annealing of the as-grown LMO films in reducing atmosphere or using low oxygen partial pressures during the growth could make it closer to the stoichiometric composition as well. The effects of forming gas post-deposition annealing on pulsed laser deposition grown $LaMnO_3$ epitaxial thin films was investigated.[33] Structural, magnetic, and optical properties coherently indicate non-stoichiometric ferromagnetic and semiconducting phases for as-grown $LaMnO_3$ films. By annealing in an oxygen-reducing atmosphere, the antiferromagnetic and insulating phases of bulk-like stoichiometric $LaMnO_3$ were recovered. It is shown that non-destructive optical spectroscopy at room temperature is one of the most convenient tools for identifying the phases of $LaMnO_3$ films. The results serve as a prerequisite in studying $LaMnO_3$ based heterostructures grown by pulsed laser deposition.

4.3.1 Sample Preparation and Crystal Structure

In order to further reduce the excess oxygen content (*i.e.* cure the possible cation defects) I fabricated additional LMO epitaxial thin films by PLD on 001 STO single-crystal substrates. These samples were grown at 700°C in 10 mTorr of oxygen; the growth rate was monitored by thickness calibration through X-ray reflectivity. Some of the as-grown films were then post-annealed in a forming gas (4% H + 96% Ar) atmosphere, at 500–900°C for 1–3 hours where it was expected that some oxygen would be extracted from the films.

It was confirmed that the physical properties of the STO substrate remained unchanged upon annealing. It should be noted, however, that the film's physical properties changed abruptly upon annealing above 700°C for longer than one hour. Film thicknesses were about 30 nm, as calculated from the clear thickness fringe reflections of x-ray diffraction (XRD) measurements taken at the synchrotron radiation source (11.2 keV) at the 10C1 beam line of the Pohang Light Source (done by W.S. Choi, Ref. [33]). These also indicated good crystallinity in the films.

Figure 4-5(a)-(b) show XRD θ-2θ scans for the as-deposited and the heat treated LMO films, respectively, to study the structural properties affected by annealing. In Figure 4-5(a) the as-grown film shows a weak 002 reflection that shows up as a shoulder on the 002 substrate peak. Furthermore, the annealed film shows a distinct peak originated from an increased *c*-axis lattice constant. Comparing the peak positions, the LMO film *c*-axis lattice constant showed an increment of about 1% after annealing. Reciprocal space maps around the 114 STO peak of the as-grown and annealed LMO film, respectively, were used to characterize the in-plane strain state.

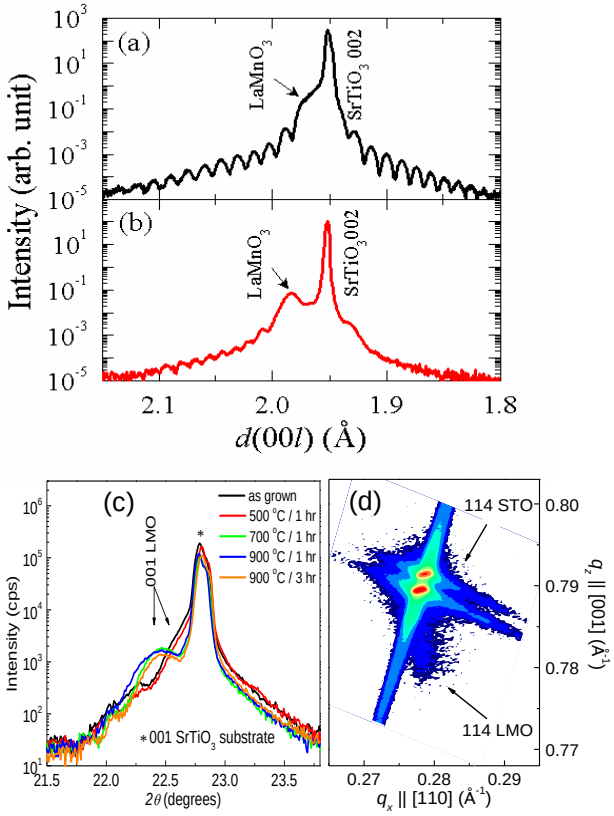

Figure 4-5 Synchrotron scattering on the as-grown (a) and the sample annealed at 900°C for 1 hour in forming gas (b)(from Ref. [33]), compared with in-house X-ray diffraction on all the samples (c). The sample thicknesses were 30 nm. Reciprocal space maps (see for example (d)) indicate perfectly strained films to the STO substrate.

While the as-grown LMO film peak was at l = 4.00 (q_z = 0.79 Å^{-1}), merged into the STO peak, that is why not shown), the annealed LMO film peak showed up at l = 3.96 (translating to q_z = 0.78 Å^{-1}, using eqn. (3-3)), again indicating an increase in the *c*-axis lattice constant. Moreover, the in-plane (*h,k)* component of the peak was fix at *(1,1)* (q_x = 0.278 Å^{-1}), confirming that the in-plane lattices for both the as-grown and the annealed LMO films were coherently strained to the substrate. The unit cell expanded from a

volume of 59.65 Å^3 to 60.59 Å^3 with annealing. The annealed LMO film unit cell volume was fairly close to that of a single-crystal, which can be as large as 60.95 Å^3.[25] This suggests that removal of the oxygen by annealing in forming gas causes expanding LMO film unit cell that eventually approaches the bulk value.

4.3.2 Magnetism and Electronic Transport

Figure 4-6 with the resistivity and magnetization data, I took, as functions of temperature of the as-grown and annealed LMO films show the effects of annealing on both properties of the films. The *M(T)* curve for the as-grown film increased strongly with decreasing temperature below 200 K, which is typical for ferromagnetic ordering.

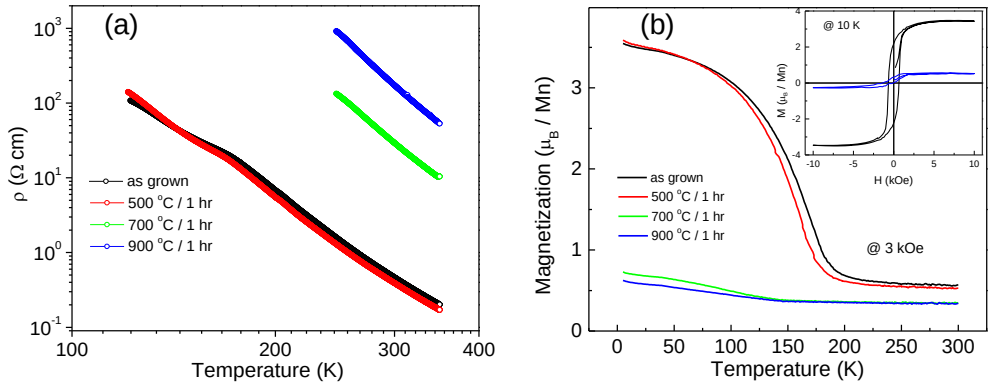

Figure 4-6 Electronic transport (a) and DC magnetization data (b) as functions of temperature. More reducing growth conditions suppress magnetization as well as conductivity (Ref. [33]).

At 10 K, the magnetic moment saturated at 3.5 μ_B/Mn. On the other hand, the *M(T)* curve increased slowly after annealing while the temperature was decreased., and the saturation magnetization was drastically reduced to about 0.5 μ_B/Mn. Moreover, the magnetic set-in

temperature was lowered down to about 145 K. The curvature of the *M(T)* curve indicated weak ferromagnetism below the onset temperature, the suppressed magnetic moment was not compatible with the perfectly ordered Mn^{3+} ion local spin model. The onset temperature was very close to the AFM ordering temperature (~140 K) of the single-crystal LMO.[25]

Magnetic field-dependent magnetization *M(H)* data were taken at low temperature of 10 K, as depicted in the inset of Figure 4-6 (b). The M-H curve also showed drastically reduced magnetization for the annealed film where the ~2.2 μ_B/Mn remnant magnetization decreased to ~0.2 μ_B/Mn upon annealing. While the *M(H)* curve for as-grown film could be explained by the normal FM ground state, the tiny remnant magnetic moment for the annealed film suggested that canted antiferromagnetically coupled spins were the reasons for FM ground state of the film. Such a reduced FM moment has typically been observed in single-crystals with canted AFM spins.[25] The reduced remnant magnetic moment and the reduced transition temperature of the magnetization suggested that the bulk-like AFM ground state was obtained with annealing in an oxygen reducing condition.

The *dc* conductivity data were consistent with previous observations (*c.f.* inset in Figure 4-4 (b)). The resistivity increases upon reducing growth conditions *e.g.* collapsing ferromagnetic correlations. The activation energies remain the same. Moreover, an anomaly was observe around the FM ordering temperature, which is thought to originate from the double exchange interaction (see Section 2.2.3.2 for more details) due to the Mn^{4+}-ions in the pristine film.

4.3.3 Optical Conductivity

σ(ω) was measured on the pristine and heat-treated LMO films at room temperature. For the spectroscopic study of the LMO film electronic structure, near-normal-incident geometry was used, reflectance and transmittance spectra were measured in the energy range of 0.07–5.9 eV at Pohang University by W.S. Choi.[33] Fourier transform infrared spectrometer (Bruker IFS66v/S) and a grating-type spectrophotometer (CARY 5G) at 0.07–1.2 and 0.4–5.9 eV, respectively, were used. The in-plane optical conductivity spectra $\sigma(\omega)$ at 0.3–3.2 eV, where the STO substrate was transparent, were calculated by using an intensity-transfer-matrix method numerical-iteration process.[26]

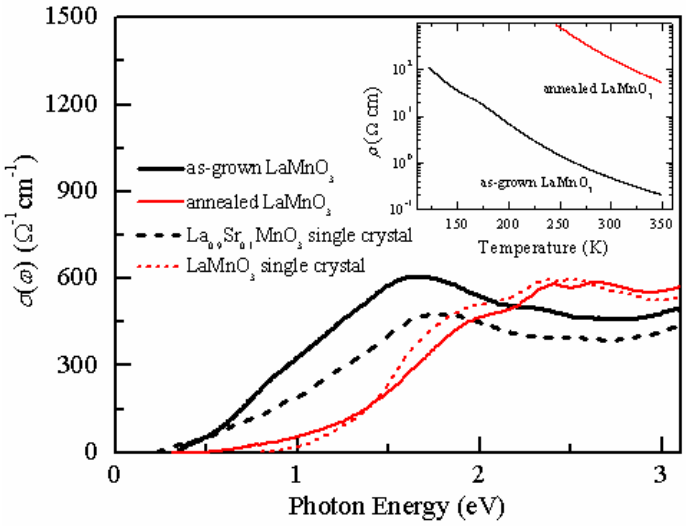

Figure 4-7 (a) $\sigma(\omega)$ for the as-grown (thick black solid line) and annealed (thin red solid line) $LaMnO_3$ films. For comparison, $\sigma(\omega)$ for $La_{0.9}Sr_{0.1}MnO_3$ (thick black dotted line) and $LaMnO_3$ (thin red dotted line) single crystals are also shown. [Ref. 41] The inset shows the temperature dependent resistivity for as-grown (thick black line) and annealed (thin red line) $LaMnO_3$ films. The $\sigma(\omega)$ data were taken by W.S. Choi. This figure was fully adopted from Ref. [33].

For comparison, data reproduced from the literature for LMO and $La_{0.9}Sr_{0.1}MnO_3$ single-crystals are also shown in Figure 4-7.[40] The optical conductivity of pristine and annealed LMO films had similar spectral features to doped (i.e., $La_{0.9}Sr_{0.1}MnO_3$) and undoped LMO single-crystals, respectively. Careful comparison of $\sigma(\omega)$ for the LMO films with single-crystalline phases provided a complementary understanding of the forming gas annealing mechanism that recovered the bulk-like LMO phase.

The same way, the LMO single-crystal, the $\sigma(\omega)$ of the annealed LMO film showed an ω^2-like increase just above the optical gap with a ripple-like shaped peak centered at ~2.3 eV. An upturn at ~3 eV was observed in all of the films and single crystals. It suggested the initiation of the charge-transfer transition from the oxygen to the Mn ions. The ~2.3 eV peak has been previously attributed to the photo-excitation of electrons in the Mn^{3+} ion e_g orbitals in stoichiometric LMO.[27,28] The similarity between the annealed film and LMO single crystal indicated that the annealed film had a stoichiometric phase and that the peak at ~2.3 eV in the film was due to the photo-excitation of the Mn^{3+} ion e_g orbitals.

The $\sigma(\omega)$ of the as-grown LMO film showed three features, which were different from those of the annealed one: a slightly decreased optical gap, a suppression of the ~2.3 eV peak as well as the ripple-like pattern, and a spectral weight increase at ~1.7 eV. The $\sigma(\omega)$ of the hole-doped manganite $La_{0.9}Sr_{0.1}MnO_3$ single-crystal showed similar spectral features.

While the stoichiometric LMO crystal has only Mn^{3+}-ions, Sr-doping introduces Mn^{4+}-ions into the Mn-sublattice. Mn^{4+}-ions have holes in the e_g orbitals, which results in

semiconducting FM coupling between the local spins via double exchange as described in Section 2.2.3.2. Moreover, the holes become polaronic carriers, which lead to the development of a mid-gap state below the optical gap in LMO.[29] The corresponding development of the mid-gap state in the as-grown LMO film suggested the presence of Mn^{4+}-ions in the film, probably due to cation vacancies induced during the highly energetic PLD process.

From the similarity of $\sigma(\omega)$ in the as-grown LMO film to that of the $La_{0.9}Sr_{0.1}MnO_3$ single-crystal, the amount of cation vacancies in the film was estimated and the phase of the as-grown film was identified. In the $La_{0.9}Sr_{0.1}MnO_3$ single crystal, 10% of the Mn^{3+}-ions became Mn^{4+}-ions to match the chemical valence. According to the relationship $(La^{3+}_{1-x}[\ ]_x)(Mn^{3+}_{1-7x}Mn^{4+}_{6x}[\ ]_x)O_3^{-2}$, x should be 1/60 to induce a 10% transition to Mn^{4+}-ions. This indicates that assuming there are both La and Mn vacancies, about 1.67% of the unit cells should contain cation vacancies. It has previously been reported that when the value of x is larger than about 0.03, the LMO single-crystal has a transition from orthorhombic to rhombohedral, and the spin ordering becomes entirely FM.[25] Since $x < 0.03$ in the as-grown LMO film and any possible structural phase transitions can be suppressed by epitaxial strain, it is concluded is that the film could have an orthorhombic structure with a reasonable amount of FM components.

The growing c-axis lattice constant upon annealing can be explained by the valence state of the Mn-ions. Suppose that the as-grown LMO has Mn^{4+} ions along with Mn^{3+} ions. Since Mn^{3+} ions (65 pm) are larger than Mn^{4+} ions (54 pm),[30] the annealed LMO film, consisting primarily of Mn^{3+} ions, should have the larger observed lattice constant.

4.3.4 Conclusions

The XRD, magnetization, and $\sigma(\omega)$ data consistently show that annealing in an oxygen reducing atmosphere is obligatory to reduce the Mn^{4+} ions in as-grown films so as to reproduce bulk-like magnetic and optical properties. Optical spectroscopy has a great advantage as a measurement tool, as well as it can be used simply and quickly at room temperature. Comparison between spectra obtained and the ones in the literature, a quantitative evaluation of the rough estimate of the amount of cation vacancies could be given.

4.4 Growth Control by Laser Fluence

At this point, synthesizing near-stoichiometric $LaMnO_3$ film was almost done, so that reliable magnetic exchange phenomena can be studied when incorporating this oxide in heterostructures or superlattices. However, there was one growth parameter not touched yet but seems to be crucial in many oxide thin film growth processes.

In case of $SrTiO_3$, laser fluence (J) has been reported to be a critical growth parameter strongly modifying the plume dynamics and thus the composition of the plume and the film.[31]

4.4.1 Sample Preparation and Crystal Structure

For this study[32], I grew LMO thin films in various oxygen and forming gas (Ar + 4% H_2) pressures ranging from 2×10^{-6} to 2×10^{-1} Torr at a laser repetition rate of 10 Hz. In

order to explore the influence of laser fluence, I varied the laser energy while keeping the rectangular spot size (3 mm^2) constant. In order to extend the range of the laser fluence (0.1 – 3.5 J/cm^2), a set of quartz plates were used for further attenuating the laser energy on the target surface.

XRD θ-2θ scans confirmed overall single-phase, epitaxial growth of LMO films on (001) STO substrates. While the in-plane lattices of all thin films studied here were commensurately aligned, *i.e.*, fully strained [see reciprocal space maps (RSMs) in Figure 4-8(b-c)], the out-of-plane lattice constant varies dramatically depending on the growth conditions. Figure 1(a) shows examples grown in 10^{-4} Torr of O_2. Increasing laser fluence leads to gradually expanding the lattice in almost all the cases. Such increase in the out-of-plane lattice constant is more pronounced when grown in lower O_2 pressures. However, thin films grown in higher oxygen pressures, *e.g.* 0.2 Torr, show no change in the lattice parameters (Figure 4-9(a)), unlike low pressure grown thin films. In the former case, the film lattices are almost identical to those of the STO substrate, *i.e.* 0.3905 nm.

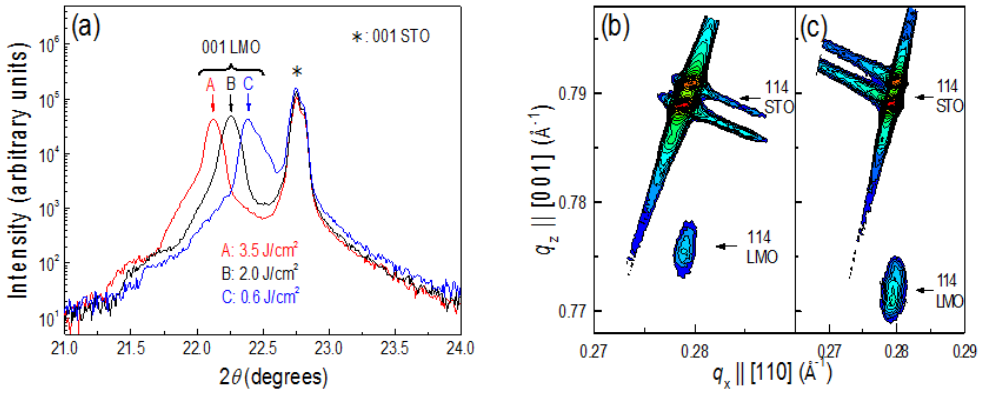

Figure 4-8 (a) XRD θ-2θ scans of $LaMnO_3$ thin films grown on (001) STO substrates in 10^{-4} Torr oxygen. Increasing the laser fluence results in monotonically expanded lattices without influencing their high degree of epitaxy (FWHM ~ 0.04° – 0.06° in ω rocking curve scans). (b-c) Reciprocal space maps of $LaMnO_3$ thin films grown in 10^{-4} Torr O_2 confirm the fully strained in-plane lattices, coherent with the substrate ones. Note in the maps that the reciprocal lattices are labeled based on the scattering vector length set equally to the reciprocal lattice unit $\lambda/2d$. The laser fluences used are 0.9 (b) and 2.0 J/cm^2 (c) [32].

PLD is known to be an energetic process as the plume energy can be on the order of 10-100 eV. Moreover, the interaction of laser plume with the background gas can influence the kinetics and chemistry of the plume. Therefore, in order to check whether the change in the lattice size is related with oxygen content or is due to the highly energetic PLD process, thin films in a reducing atmosphere were also grown, *i.e.* forming gas, under various laser fluences and background pressures.

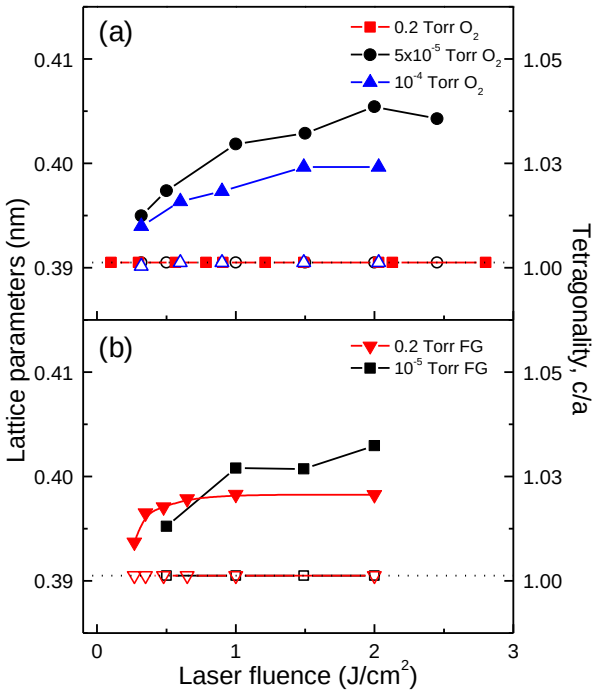

Figure 4-9 In-plane (open symbols) and out-of-plane (solid symbols) lattice constants of $LaMnO_3$ films grown in (a) oxygen and (b) forming gas (FG). Note that, in (a), both *a* and *c* lattice constants of the $LaMnO_3$ film grown in 0.2 Torr are identical [32].

Interestingly, as shown in Figure 4-9(b), the use of a high pressure forming gas results in largely expanded lattices.

Since the growth in such a high pressure, *e.g.* 0.2 Torr, could reduce the plume energy, *i.e.* kinetic energy of ablated species, by increased interactions with the background gas, the expanded lattice size can be attributed to the reduced amount of oxygen in the film. A similar behavior has been observed in $LaMnO_3$ films annealed *ex situ* in forming gas at high temperatures.[33] This indicates that the reduction of excess oxygen in $LaMnO_3$ films is mainly governed by thermodynamic limitations, while the kinetic effect cannot be still

ignored as the use of lower forming gas pressure resulted in a further increase in the *c*-lattice constant (see Figure 4-9(b)). The kinetic influence on the lattice size change can be mainly found from samples grown in low pressures of both oxygen and forming gas. Evidently, the use of higher laser fluence seems to gradually reduce the oxygen content and/or enhance the cation ratio (La/Mn) in thin films. Likewise, while the *c* lattice parameter of $LaMnO_3$ films grown in high pressure forming gas atmospheres (Figure 4-9(b)) has almost no variation with laser fluence for $J > 0.5$ J/cm^2, the growth with a lower laser fluence ($J < 0.5$ J/cm^2) resulted in a gradual reduction in the *c*-lattice parameter, *e.g.*, the unit cell volume. The reduced unit cell volume (*i.e.* lower oxygen vacancy content) also caused the increased magnetic transition temperature, implying that the use of too low laser fluence can result in the increased cation off-stoichiometry.[31]

4.4.2 Magnetism and Electronic Transport

The magnetic properties, I investigated by SQUID measurements, show that, above certain laser fluence, further increasing of fluence does not alter the magnetic property. The critical fluence depends on the growth pressure and background atmosphere as shown in Figure 4-10 (d). The use of lower laser fluence (i.e. less kinetic laser plume) is undesirable for manganite films due to the difficulty in maintaining the right cation stoichiometry as evidenced from the increase in T_c (see Figure 4-10(d)). This observation seems to be rather counterintuitive as compared to the PLD growth of $SrTiO_3$ under reducing growth condition.[34,35] This discrepancy, however, originates largely due to the fact that $LaMnO_3$ thin films grow with excess oxygen associated with cation off-

stoichiometry while $SrTiO_3$ films are typically oxygen deficient. Therefore, it is presumed that the growth of stoichiometric $LaMnO_3$ requires rather reducing and highly energetic PLD conditions in order to take advantage of high kinetic energy of ablated species. On the other hand, $SrTiO_3$ prefers opposite conditions for the right oxygen stoichiometry. Therefore, although it is not the main claim in this work, it is noted that the growth of $SrTiO_3$ should be done under highly oxidizing and less energetic PLD conditions.

In all cases, fluences larger than 1 J/cm^2 show no change in the magnetic transition temperatures. On the other hand, Figure 4-10(a) depicts the importance of reducing conditions in order to suppress ferromagnetism in the LMO samples (data taken at a fluence of 2 J/cm^2).

Growth in high oxygen pressures results in creation of excess oxygen and so increased cation off-stoichiometry, which produces ferromagnetic correlations. One can see a dramatic decrease in the net magnetic moment after both depleting oxygen and eventually replace it by forming gas during the film growth. This is in good agreement with the results found in doped manganites ($La_{0.7}Sr_{0.3}MnO_3$).[31] In order for readers not to be confused, however, it is worth noting that the dependence of the magnetic transition temperature on oxygen pressure in the undoped manganites should be opposite to the one in doped manganites (e.g. see Fig. 2(a) in Ref. [31]).

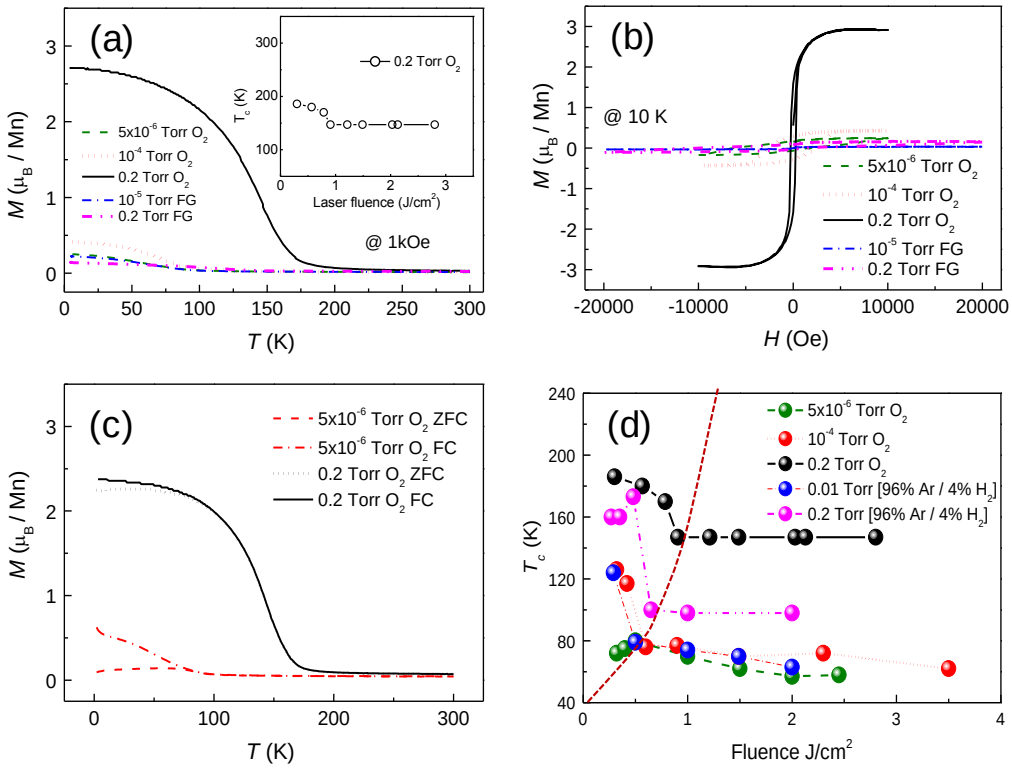

Figure 4-10 Temperature dependence of magnetization of $LaMnO_3$ films grown in O_2 and forming gas (denoted with FG) at different background pressures ranging from 0.2 Torr to 5×10^{-6} Torr at 2 J/cm^2. 1000 Oe external field was used to intensify the signal. The inset in (a) shows T_C of the 0.2 Torr sample while (d) displays the Tc results in the entire fluence range studied. (b) *M(H)* loops demonstrate how more reducing conditions eliminate further the ferromagnetic correlation in the manganite layers (b). Significant opening between zero-field cooled (ZFC) and field cooled (FC) *M(T)* curves signify that antiferromagnetism is present in the samples grown at low pressure O_2 and FG (c). High growth pressure maintains ferromagnetism. (a)-(c) are published in Ref. [32].

The change in cation composition was confirmed by x-ray photoelectron spectroscopy as shown in Table 4-1, which summarizes the quantitative change in cation ratio as a function of oxygen background pressure during the PLD growth.

Table 4-1 Variation of the La/Mn cation ratio measured by XPS as a function of oxygen background pressure during the growth of LMO thin films [32].

P_{O2} (Torr)	La/Mn
5×10^{-6}	0.97
1×10^{-4}	0.92
2×10^{-1}	0.81

The cation ratio mismatch is gradually increased as increasing the oxygen pressure. The trend is in good agreement with magnetization data. *M(H)* loops recorded at 10 K on the samples grown at 2 J/cm^2 clearly confirm that the films grown in a high oxygen pressure (0.2 Torr) are indeed highly FM because missing La ions may dope holes onto Mn sites increasing the Mn^{4+}/Mn^{3+} ratio. On the other hand, the samples grown under the most reducing conditions, *i.e.* low pressure and high fluences, exhibited reduced magnetic moments suggesting that those films may have the bulk-like spin ordering, i.e. A-type AFM, by improving the cation stoichiometry (note that the film grown in 10^{-4} Torr shows a huge coercivity). A similar behavior has been reported in Sr-doped LMO thin films.[36]

In order to find out the nature of the magnetic transition observed, I examined two extreme cases. The temperature dependence of the magnetic moment was measured after

cooling without applied magnetic field (ZFC) and at 2 Tesla (FC). A measuring field of 1000 Oe was used to enhance the magnetic signal (Figure 4-10(c)). The data clearly shows a tremendous difference between the two growth conditions. While the 0.2 Torr sample shows a tiny variance between the two curves at low T, the sample grown in 5×10^{-6} Torr oxygen exhibits a significant difference between ZFC and FC magnetization-temperature scans. Such a deviation is the signature of antiferromagnetic correlation.

The *dc* transport measurements were attempted in order to understand the nature of the electric ground states. Interestingly, all samples measured were highly insulating (> MΩ). Yet no observation of the metallic ground state is intriguing as this system is grown under highly reducing conditions and also offers a similar structure of electronic reconstruction observed in conducting LTO/STO and LAO/STO systems.[37,38] This could be attributed the excess oxygen or worse cation stoichiometry in the LMO films, preventing the interface electronic reconstruction. Moreover, it seems that the excess oxygen might suppress the generation of oxygen vacancies during the growth under high vacuum.[39] Moreover, one can also consider that the La^{3+} deficiency originating from the cation off-stoichiometry may result in more pronounced buckling of the corner sharing oxygen octahedra, preventing the electronic conduction by, e.g. reduced hopping integral.

I was trying to find out what causes the well-defined critical fluence (J_c) above which the magnetic properties do not change. It is well-known that there is an optimum range of laser energy densities on the oxide targets providing full ablation. Naturally, the different species need dissimilar energy to escape the target. As the growth pressure went up, J_c seemed to follow. Since the plume's shape changes a lot with background pressure, it is straightforward to think that the cation off-stoichiometry leading to varying T_c is due to

scattering by the background gas. If it is caused by scattering then either T_c or J_c should scale with an effective scattering cross-section variable. This variable must be proportional to the square of the effective atomic radius (r) of the background gas as well as the number of scattering centers which translates to pressure (p). The result is depicted in Figure 4-11.

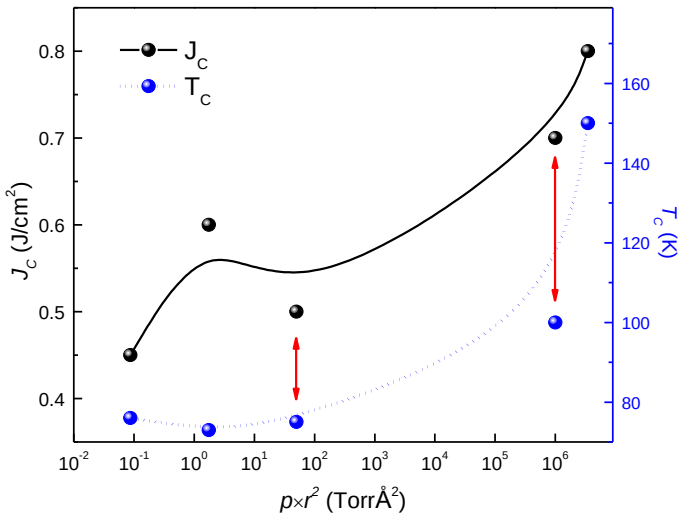

Figure 4-11 Critical fluence and T_c dependence on an effective scattering cross-section. The red arrows point at data taken in forming gas background (Marton, unpublished).

The critical fluence showed no evidence of scaling with the cross-section I defined. However, T_c might show a square dependence which unfortunately cannot be fully supported with the number of data points I have. Future experiments need to be done to completely map out the true reason of J_c and T_c dependence on the growth conditions.

4.4.3 Optical Conductivity

The interpretation of the measured results as the evidence of bulk-like magnetic ground state is also supported by room temperature optical absorption data taken from samples grown at 2 J/cm^2 using a spectrophotometer (Cary5000, Varian). As shown in Figure 4-12, there are two types of spectral details. One of them shows a broad absorption peak at ~1.7 eV (*e.g.*, see the spectrum from the film grown in 0.2 Torr O_2, marked with solid black arrow), and the other has fine structures with peaks appearing at a higher photon energy > 2.0 eV (*e.g.*, 0.2 Torr forming gas, marked with solid magenta arrows).

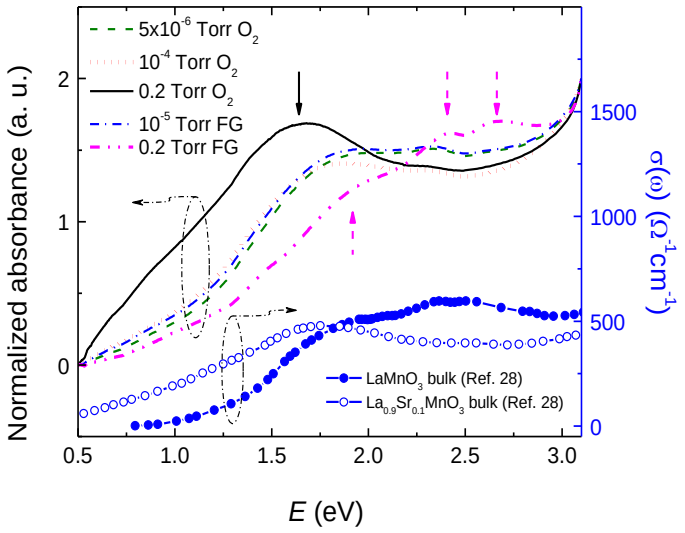

Figure 4-12 Optical absorbance spectra taken at room temperature from Ref. [32]. The broad peak at ~ 1.7 eV (solid black arrow) is the signature of hole doping (Ref.[41]). Samples grown at lower pressure show significant deviation from it. The fine structure at higher photon energies (solid magenta arrows) resembles the behavior of stoichiometric bulk LMO. In the case of lower oxygen and forming gas pressure growth, can see the transition into bulk like quality. The samples were grown using 2 J/cm^2. The data from bulk single crystals [Ref. 41] serve as reference.

The former is characteristic for slightly doped perovskite manganites,[40] originating from a combination of Jahn-Teller polaron hopping and e_g electrons' intraband transitions. Another extreme growth condition tested was the use of high pressure forming gas (0.2 Torr) to deplete as much oxygen as possible. However, it was found that the high pressure forming gas was not as effective as low oxygen and forming gas atmospheres growth to reduce the oxygen content in the films as shown in Figure 4-9(b). Nevertheless, the use of high pressure forming gas results in bulk-like electronic ground state, as confirmed by comparing the characteristic optical absorption spectra (see Figure 4-12) by DC transport (Note that all films are highly insulating). The optical spectrum from the sample grown under high pressure forming gas is very similar to the one from bulk samples reported elsewhere and to the sample annealed in high temperature forming gas.[33,41]

As the growth pressure was further lowered for both oxygen and forming gas, the dominant absorption peak shifts to lower photon energies, revealing a bit different spectral features that have not been reported from bulk counterparts. The new electronic state evidenced by the optical absorption spectra can be a consequence of epitaxial stabilization, for instance, high c/a ratios, which can modify the energies of e_g orbitals altering the absorption spectra. A similar thermodynamic stabilization under low background pressures has been reported for doped manganite thin films.[31] Since no significant magnetic moment was observed from samples grown under low background pressures, it was conclude that undoped $LaMnO_3$ films thermodynamically prefer to be grown under rather low background pressures with higher laser fluence. Moreover, it is

worth pointing out that the absorption spectrum from the film grown in 10^{-4} Torr O_2 is not consistent with the other films. Thus, its spectral feature might be associated with its non-negligible magnetization (see Figure 4-10(b)).

4.4.4 Conclusions

$LaMnO_3$ epitaxial thin films were grown by PLD under various growth conditions. It is found that the growth of $LaMnO_3$ epitaxial thin films with bulk-like magnetic and electrical properties requires highly energetic, reducing conditions such as high laser fluence and low background pressure for improved cation stoichiometry. While the use of high pressure forming gas (0.2 Torr) can be effective in achieving manganite thin films with bulk-like properties, it was found that growing epitaxial films in very low oxygen pressure (~10^{-6} - 10^{-4} Torr) with high laser fluence can further stabilize highly insulating, presumably antiferromagnetic manganite thin films with lower magnetic transition temperature. These results indicate the usefulness of the highly energetic PLD process for stabilizing bulk-like single crystalline $LaMnO_3$ thin films.

4.5 Summary

In this chapter, stoichiometric $LaMnO_3$ single crystalline thin film synthesis was aimed at. This material prefers adopting excess oxygen, which turns the ground state into ferromagnetic insulator. Based on structural (high resolution four-circle X-ray diffraction), magnetic (superconducting quantum interference device), electronic transport (physical properties measurement system), optical absorption

(spectrophotometer) experiments as well as directly measuring the cation compositions (X-ray photoelectron spectroscopy) the oxygen content was successfully reduced. Several methods were tried: post-annealing in forming gas, growing in low pressure oxygen, vacuum and forming gas. Besides significantly suppressing the amount of excess oxygen in the films, the stoichiometric cation content was stabilized by using high laser energy density (fluence) on the target. The critical fluence above which the magnetic transition temperature remains constant may be characteristic for the interaction between the background gas and ablated species. This mechanism, however, needs further studying.

References

[1] Y. Tokura, Colossal Magnetoresistive Oxides, Gordon and Breach Science Publishers, 2000.

[2] E. Dagotto, Nanoscale Phase Separation and Colossal Magnetoresistance, Springer-Verlag Berlin Heidelberg, 2003.

[3] S. Jin , T. H. Tiefel , M. McCormack , R. A. Fastnacht , R. Ramesh , and L. H. Chen, Science 264, 413 (1994).

[4] T. Kimura, T. Goto, H. Shintani, K. Ishizaka, T. Arima, and Y. Tokura, Nature 426, 55 (2003).

[5] N. Hur, S. Park, P. A. Sharma, J. S. Ahn, S. Guha, and S-W. Cheong, Nature **429**, 392 (2004).

[6] K. Ueda, H. Tabata, and T. Kawai, Phys. Rev. B **60**, R12561 (1999).

[7] H. Yamada, Y. Ogawa, Y. Ishii, H. Sato, M. Kawasaki, H. Akoh, and Y. Tokura, Science **305**, 646 (2004).

[8] H. Yamada, M. Kawasaki, T. Lottemoser, T. Arima, and Y. Tokura, Appl. Phys. Lett. **89**, 052506 (2006).

[9] A. Bhattacharya et al., Phys. Rev. Lett. **100**, 257203 (2008).

[10] B. R. K. Nanda and S. Satpathy, Phys. Rev. B **78**, 054427 (2008); ibid 79, 054428 (2009).

[11] S. Dong, R. Yu, S. Yunoki, G. Alvarez, J.-M. Liu, and E. Dagotto, Phys. Rev. B **78**, 201102(R) (2008).

[12] S. Smadici et al., Phys. Rev. Lett. **99**, 196404 (2007).

[13] J. B. Goodenough, A. Wold, R. J. Arnitt and N. Menyuk, Phys. Rev. **124**, 373 (1961).

[14] T. Kenjo, and M. Nishiya, Solid State Ion. **57**, 295–302 (1992).

[15] T. Chatterji,1,2 F. Fauth, B. Ouladdiaf, P. Mandal, and B. Ghosh, Phys. Rev. B **68**, 052406 (2003).

[16] M. Cestelli Guidi, et al.,Phys. Rev. B **64**, 064414 (2001).

[17] P. Murugavel et al., Appl. Phys. Lett. **82**, 1908 (2003).

[18] K. Nakamura and K. Ogawa, J. Solid State Chem. **163**, 65 (2002).

[19] K. Nakamura, J. Solid State Chem. **173**, 299 (2003).

[20] C. Aruta, M. Angeloni, G. Balestrino, N. G. Boggio, P. G. Medaglia, A. Tebano, B. Davidson, M. Baldini, D. Di Castro, P. Postorino, P. Dore, J. Appl. Phys. **100**, 023910 (2006).

[21] J. H. Kuo, H. U. Anderson and D. M. Sparlin, J. Solid State Chem. **83**, 52 (1989).

[22] J. A. M. van Roosmalen and E. H. P. Cordfunke, J. Solid State Chem. **110**, 100 (1994).

[23] J. Töpfer and J. B. Goodenough, Chem. Mater. **9**(6), 1467 (1997).

[24] H. S. Kim and H. M. Christen, J. Phys.: Condens. Matter. **22**, 146007 (2010).

[25] C. Ritter, M. R. Ibarra, J. M. D. Teresa, P. A. Algarabel, C. Marquina, J. Blasco, J. Garc, S. Oseroff and S.-W. Cheong, Phys. Rev. B **56**, 8902 (1997).

[26] H. S. Choi, J. S. Ahn, W. Jo and T. W. Noh, J. Kor. Phys. Soc. **28**, 636 (1995).

[27] M. W. Kim, P. Murugavel, S. Parashar, J. S. Lee and T. W. Noh, New J. Phys. **6**, 156 (2004).

[28] K. Myung-Whun, J. Kor. Phys. Soc. **53**, 3365 (2008).

[29] J. H. Jung, K. H. Kim, T. W. Noh, E. J. Choi and J. Yu, Phys.Rev. B **57**, R11043 (1998).

[30] R.D. Shannon and C. T. Prewitt, Acta Crystallogr. B **25**, 925 (1969).

[31] J. H. Song, T. Susaki, H. Y. Hwang, Adv. Mater. **20**, 2528 (2008).

[32] Z. Marton, S. S. A. Seo, T. Egami, and H. N. Lee, Journal of Crystal Growth, **312**(20), 2923 (2010)

[33] W.S. Choi, Z. Marton, et al, J. Phys. D: Appl. Phys. **42**, 165401 (2009).

[34] T. Ohnishi, M. Lippmaa, T. Yamamoto, S. Meguro, and H. Koinuma, Appl. Phys. Lett. **87**, 241919 (2005).

[35] T. Ohnishi, K. Shibuya, T. Yamamoto, and M. Lippmaa, J. Appl. Lett. **103**, 103703 (2008).

[36] P. Lecoeur, A. Gupta, P. R. Duncombe, G. Q. Gong, and G. Xiao, J. Appl. Phys. **80**, 513 (1996).

[37] A. Ohtomo and H. Y. Hwang, Nature (London) **427**, 423 (2004).

[38] A. Ohtomo, D.A. Muller, J.L. Grazul, and H.Y. Hwang, Nature **419**, 378 (2002).

[39] S. S. A. Seo et al., Appl. Phys. Lett. **95**, 082107 (2009).

[40] J. H. Jung, K. H. Kim, T. W. Noh, E.J. Choi and J. Yu, Phys. Rev. B. **57**, R11043 (1998).

[41] K. Takenaka et al., J. Phys. Soc. Jpn. **68**, 1828 (1999).

5. Ferroelectric Field Effect in Manganite Films

This chapter discusses the effort to electrostatically modulate materials properties, such as magnetism and electronic transport, in strontium doped manganite (LSMO) systems. Ferromagnetic / ferroelectric heterostructures were synthesized on (001) $SrTiO_3$ (STO) substrates and underwent rigorous structural, magnetic, and transport studies. LSMO layers were incorporated in field-effect device structures in order to demonstrate ferroelectric field effect in these complex oxides, which have unusually high charge carrier density introduced by chemical doping. After trying numerous ways and methods, I succeeded in arriving at a huge ferroelectric modulation in ultrathin LSMO films of different doping level. This section of the thesis is a snapshot of an ongoing project offering plenty of possible paths to walk, materials to employ and physics to discover.

5.1 Introduction

Recently, there have been several efforts made to utilize ferroelectric field effect to dope and switch correlated electron systems between states. Successful switching was demonstrated in ultra thin high Tc superconductor films using conventional dielectric[1] and ferroelectric[2] material as a gate oxide.

In the case of manganites the situation is not so clear. So far electrostatic modulation of resistance by ferroelectric field effect has been presented in $La_{0.8}Sr_{0.2}MnO_3$[3,4] and $La_{0.67}Ca_{0.33}MnO_3$ [5]. Metal-insulator transition was induced by ferroelectric polarization in ultra-thin film of about 10 monolayers thick [6]. This suggests a screening length of a few

unit cells (u.c.) in manganites. In fact, resistance modification in thin manganite layer has also been interpreted as strain effect driven by the piezoelectric response from the underlying ferroelectric.[7]

Despite these preliminary successes there are three main drawbacks in these manganite based all-perovskite structures. First, the ferroelectrics do not seem to have high enough polarization (30-50 $\mu C/cm^2$) to induce significant modulation.[3,6] There is no report on leakage current measurement whose high value can also lead to low performance. Second, very short retention time of several hours[5] measured in these structures prevents them from becoming reliable memory storage devices. The third difficulty is the fairly low mobility of the transition metal oxides at room temperature, which is most of the time less than 1 cm^2/Vs. The low mobility is attributed to the strong electron-lattice coupling in the form of polarons.[8,9] At low temperatures, in the metallic phase, mobility improves to a few tens of cm^2/Vs, but it varies with thickness of thin films, which is probably due to the strain state of the thin films.[10]

The goal of this work is to study the ferroelectric field effect in doped manganites employing highly polar PZT gate oxide. I utilize PZT thin film gates with the highest ever reported remanent polarization above 80 $\mu C/cm^2$. I demonstrate sharp switching in the semiconductor at the metal-insulator transition (MIT). Also, I show a new way to speed up the transition metal oxide (TMO) channel by approaching the low temperature MIT critical concentration by means of field effect and using the non-linear response in the LSMO mobility.

5.2 Field Effect in Correlated Electron Systems

Correlated electron systems, mostly transition metal oxides, exhibit strong interplay between spin, charge, orbital, and lattice degrees of freedom. These complex interactions lead to rich and unexpected electronic-magnetic phases which can be stabilized by doping, pressure, temperature or applied magnetic field. V_2O_3 undergoes metal-to-insulator transition when doped by Cr, Ti or simply under external pressure.[11] So do certain optimally doped manganites ($La_{1-x}Ca_xMnO_3$, $La_{1-x}Sr_xMnO_3$) when cooling, while the transition temperature and resistivity can be varied by applied magnetic field. The field may suppress the resistivity by several orders of magnitude, hence the name: colossal magnetoresistive (CMR) oxides.[12] Superconductors with the highest transition temperatures turned out to be doped cuprates ($YBa_2Cu_3O_{6+x}$, $La_{2-x}Sr_xCuO_4$).[13] In fact, these materials are often not even single phase materials. The strong competition between these forces induces two or more co-existing phases.[14]

Sr and Ca doped $LaMnO_3$ (LSMO and LCMO respectively) have very rich phase diagrams due to the complex interplay between different degrees of freedom (Figure 5-1). Strong electron-phonon coupling leads to Jahn-Teller (JT) polaron formation which causes insulating ground state in $LaMnO_3$. Substitution of La by Sr/Ca dopes holes into the system, not only eliminating the trapped and immobile e_g electrons but also inducing local ferromagnetic correlation. The magnetic interaction is mostly mediated by the oxygen ions and is a function of relative orbital ordering and how those orbits are

occupied. The competition between all these local forces induces local electronic/magnetic inhomogeneity in the oxide semiconductors of interest (for review see Ref. [14]).

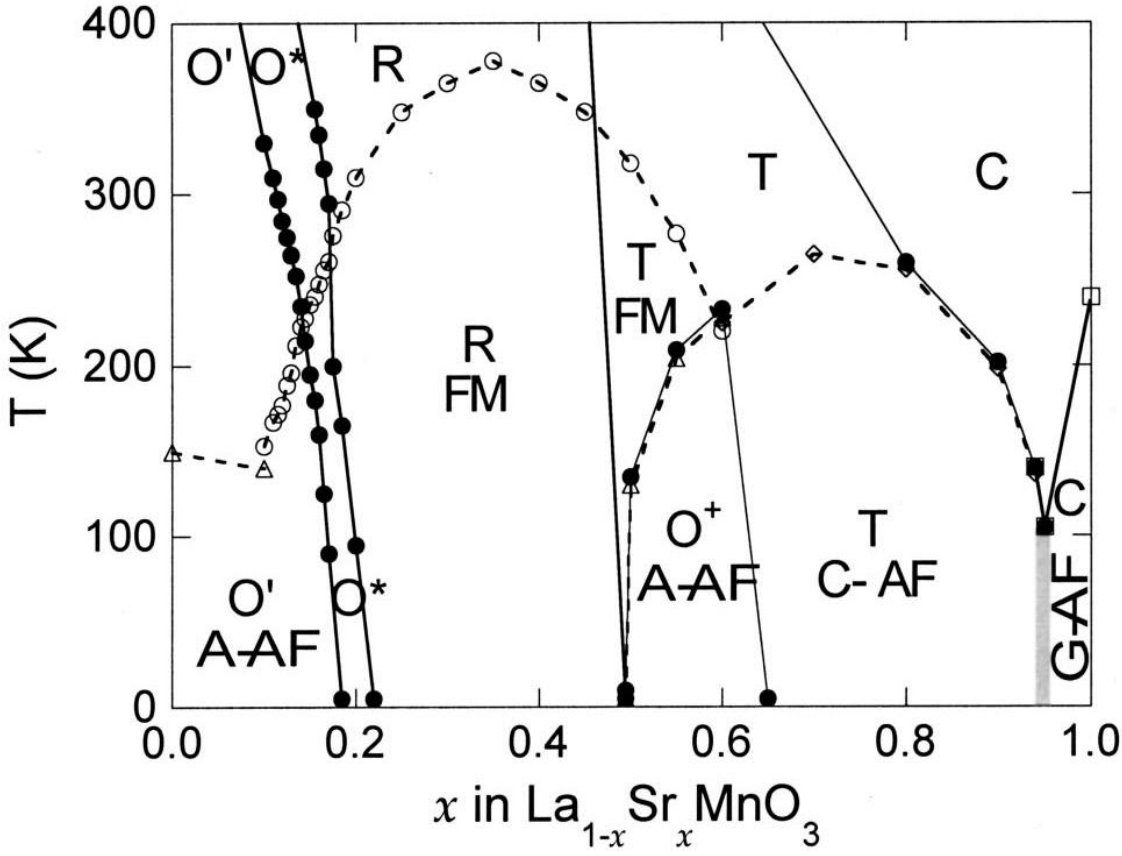

Figure 5-1 Schematic LSMO phase diagram from Ref. [40]. Further phase diagram works include Ref. [15] and [16].

This phase separation or phase co-existence has a characteristic size of a couple of nanometers.[14] Conduction and magnetism are described mostly by a percolation picture. When the created conducting network percolates, the material undergoes insulator-to-

metal transition. The percolation can be triggered by doping, temperature, magnetic field or sometimes pressure. There exists a threshold concentration (x = 0.17) above which a ferromagnetic metallic ground state is stabilized. In this composition region the resistivity can be suppressed dramatically by applied magnetic field (CMR manganites).

One of the most widely used phase diagram of LSMO was composed using an extensive electric, magnetic and structural study on single crystal samples.[15] If we have a closer look at the temperature dependent resistivity data, there is something unusual to recognize. Plotting the low temperature conductivity (σ) data as the function of the doping level (n) we get unexpected square-root dependence:

$$\sigma \propto \left(n - n_C\right)^{1/2} \tag{5-1}$$

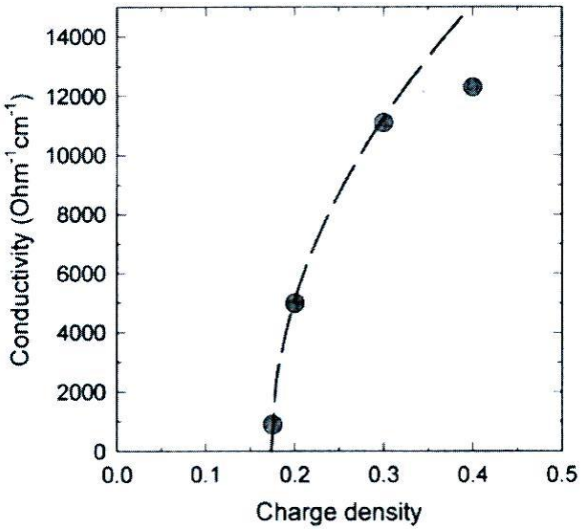

Figure 5-2 Transport measurement results extracted from [15] show that low temperature conductivity approaches the critical concentration according to a square-root law.

The nature of the percolation is thought of as being three dimensional; although there are neutron studies (Mn-O bond count) suggesting percolation in two dimensions.[17] Nevertheless, the ½ exponent indicates one-dimensional conduction, which cannot be explained by Anderson localization picture driven by the doping induced disorder. Such one dimensional filamentary conduction model was derived for doped semiconductors by Phillips.[18] It was also suggested to be relevant in the case of complex electron systems.[19]

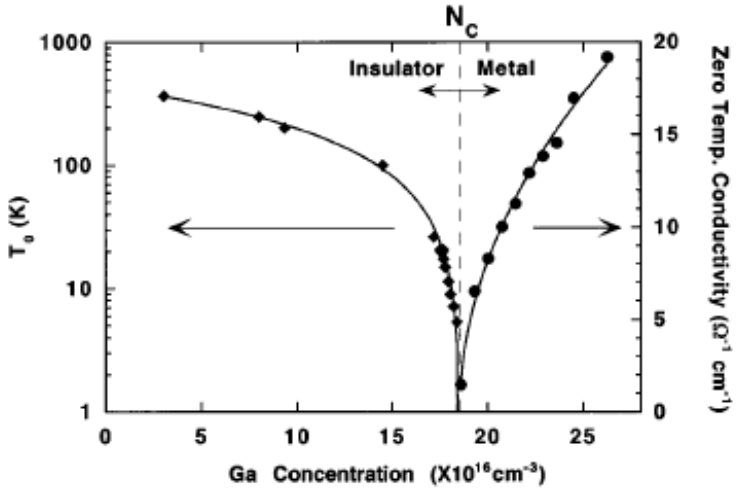

Figure 5-3 Similar square-root type behavior is followed by the extrapolated zero Kelvin conductivity of Ga doped Ge [20].

A part of this work is aiming at demonstrating the existence of the proposed filamentary nature of the conduction by imaging the conductive network. The other interesting point this work is designed to reveal is how this non-linear feature alters the mobility. If we consider the charge carrier mobility as the conductivity change, it is easy to see how the slope of the low T conductivity curve diverges close to the metal-insulator

transition. We propose to use another definition of mobility which describes the above non-linear behavior.

$$\mu = \frac{1}{e}\frac{\partial \sigma}{\partial n} \tag{5-2}$$

One has to realize that this quantity increases as we approach the low temperature metal-to-insulator transition. In order to explore the mobility as a function of doping level around the critical doping, we need to move along the charge carrier concentration axis. The most common way to do so is chemical doping. However, chemical doping induces disorder or alters the existing disorder level. Furthermore, it is not tunable. To study different compositions, always new samples must be prepared. Changing the charge carrier density in manganite thin films offers flexible way to explore new properties or access more detailed description of known states.

One way to tune the charge carrier density is by incorporating the manganite into a field-effect transistor device (Figure 5-4). Such a structure consists of a semiconductor whose conduction we want to control. On the top there is an insulator layer, called the gate (G) oxide with an electrode attached to it. On both sides of the gate there are the so-called source (S) and drain (D) electrodes. When biasing the gate (V_G), there are charges induced on the oxide-semiconductor interface which modifies the charge carrier density in the semiconductor close to the interface. This region is referred to as the active

channel. Depending on the bias (charge carrier density - n) the conductivity is tuned, which is read out by the source-drain current after applying small V_{DS}.

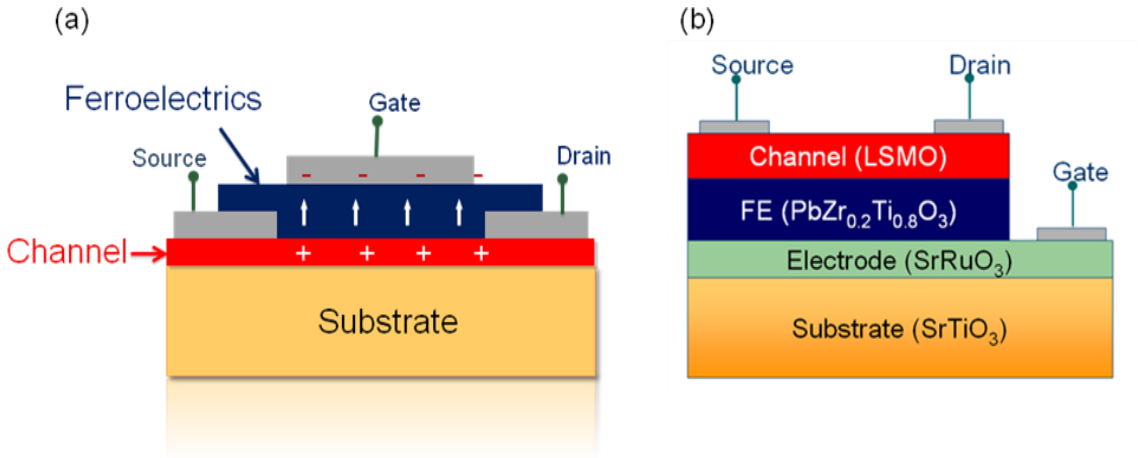

Figure 5-4 The basic structure of a metal-oxide-semiconductor ferroelectric field effect transistor (a) had to be modified to a reverse structure (b) to modulate the high charge carrier density and so the conductivity of the correlated electron oxide semiconductor channel. It was favored by available fabrication methods.

The concept of (ferroelectric) field effect device, as materials research tools, has already proved to be an effective one. Many groups have tried to switch between certain electronic and magnetic states using field effect. Previously high temperature superconductors' transition temperatures were modified by using linear dielectric as a gate oxide.[21] Using, though, such dielectrics requires huge voltages to be applied on the

structures, which may result in hot carrier injection through the gate and will alter the measurement. It also degrades the dielectric oxide via breakdown.

However, ferroelectrics do an excellent job in applications like this. One can bias the structure with usually lower voltages and use the remanent polarization to modulate the oxide semiconductor or superconductor (Figure 5-5). One advantage is that fairly high polarizations can be gained using practical voltages and that voltage does not need to be applied constantly to make the device work. In fact, only about a millisecond is enough to fully switch and preserve the device from fatigue.

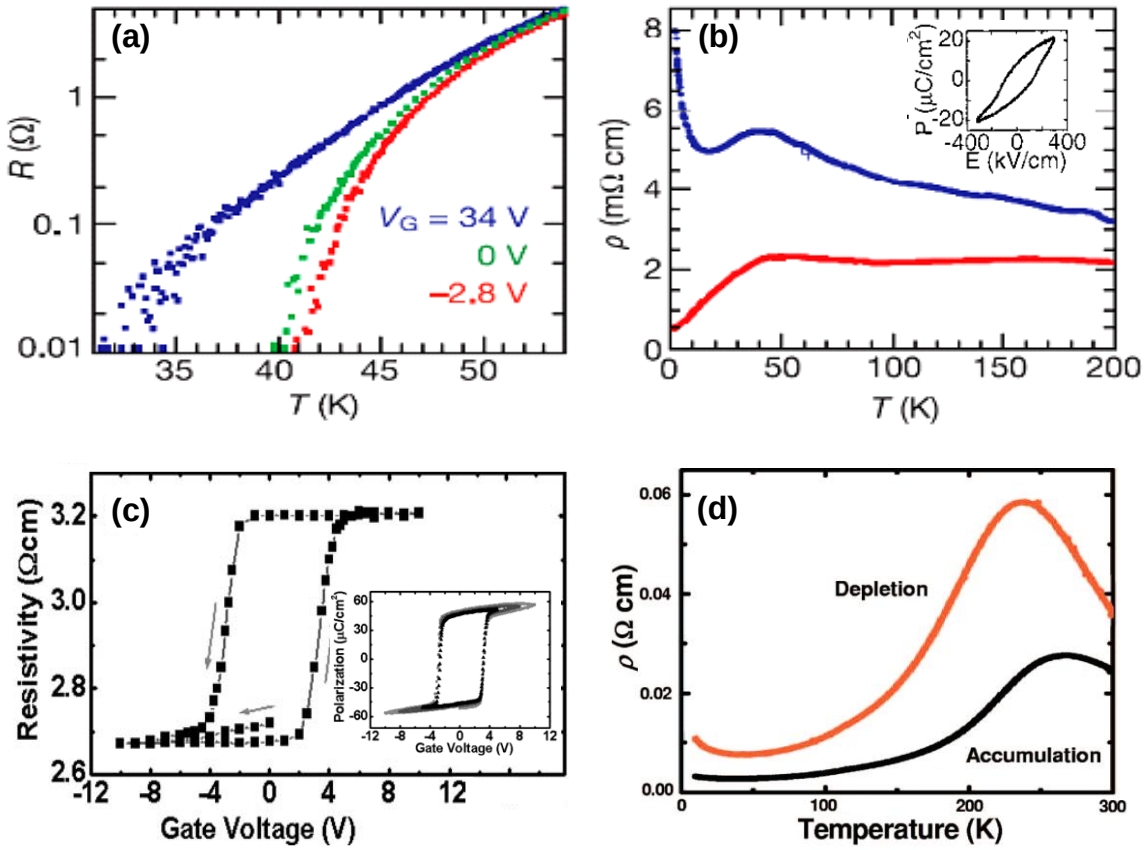

Figure 5-5 Field effect works on various correlated electron systems such as high T_c cuprates: (a) $YBa_2Cu_3O_{7-\delta}$ / $Ba_{0.15}Sr_{0.85}TiO_3$ [21], (b) $GdBa_2Cu_3O_{7-\delta}$ / $Pb(Zr_{0.2}Ti_{0.8})O_3$ [2] and CMR manganites: (c) $La_{0.8}Ca_{0.2}MnO_3$ / $Pb(Zr_{0.2}Ti_{0.8})O_3$ [22] and (d) $La_{0.67}Sr_{0.33}MnO_3$ / $Pb(Zr_{0.2}Ti_{0.8})O_3$ [23].

Although previous works demonstrated the concept of ferroelectric field effect in manganites through transition temperature shift[2] or the resistivity scaling with PZT polarization at the metal-insulator transition temperature, the effects do not exceed one order of magnitude, which is not good enough for practical applications such as memory devices. It can be a reason of a few things.

(i) Earlier experiments did not focus on the low temperature features but rather what happens around the high temperature MIT.

(ii) Quite thick PZT films were used (~ 100 – 300 nm), in which case the dielectric breakdown can be suppressed but surface roughness and inhomogeneous field induced by different ferroelectric domains make the data difficult to interpret.

(iii) Consideration is the ferroelectric polarization used. The highest polarization reported at that time was about 60 $\mu C/cm^2$. It can have to be further improved in order to demonstrate more dramatic effects in manganese oxide thin films.

For most of my studies I did not use the conventional field effect structure but kept the manganite layers on the top, while had the ferroelectric and gate electrode at the bottom. Since manganites can be selectively etched and defined certain devices on but PZT cannot, it seemed to be a convenient design to utilize (Figure 5-4).

5.3 Heterostructure Synthesis

There are quite a few delicate issues to work out in order to get convincing field effect and reliable tunability in a thin film, in which the charge carrier concentration is so high. Even if the charge distribution is highly non-uniform and the doped charges are not as mobile as in conventional metals, the screening length is thought to be a few nanometers.[6] It means one needs to use thin manganite films and/or high polarization

induced on the semiconductor-ferroelectric interface. The flawless PZT layer and high degree of epitaxy throughout the entire heterostructure are crucial points of this project.

In order to establish nice epitaxy, we used single crystal $SrTiO_3$ (STO) substrate, which already has the perovskite structure. The different oxide layers are deposited by pulsed laser deposition (PLD) technique after special substrate preparation.[24] KrF excimer laser was used to ablate the target while the substrate was kept on a constant and uniform growth temperature in the 600-700°C range. The target material controls the exact cation ratio in the film while the oxygen pressure is responsible for the degree of oxidation. The oxygen pressures we use are a couple of hundreds of mTorr.

5.4 Heterostructures Studied

5.4.1 $La_{0.8}Sr_{0.2}MnO_3$ / $Pb(Zr_{0.2}Ti_{0.8})O_3$ / $SrRuO_3$ / $SrTiO_3$

First, conducting $SrRuO_3$ (SRO) was chosen as bottom electrodes. The SRO deposition is a critical step in order to grow ferroelectric and magnetic layers thereon. The growth of atomically flat, metallic SRO films with high degree of crystallinity has already been established (Figure 5-6 (d)). The thickness has a dramatic effect on the physical properties of such metallic oxides. In the case of $SrRuO_3$, it has been reported[25] that very thin films (< 5 u.c.) exhibit an insulating nature due to the strongly reduced thickness. It was also confirmed by the samples I grew (Figure 5-6 (a-c)). Thicker films

are conducting, but probably contain defects and dislocations when grown rather thick as a consequence of strain relaxation due to the lattice mismatch between the film and substrate. Moreover, SRO is also known to be rather instable under reduced conditions due to thermal decomposition.[26] Therefore, in this work, the growth condition for other films thereon is chosen careful to avoid such problems.

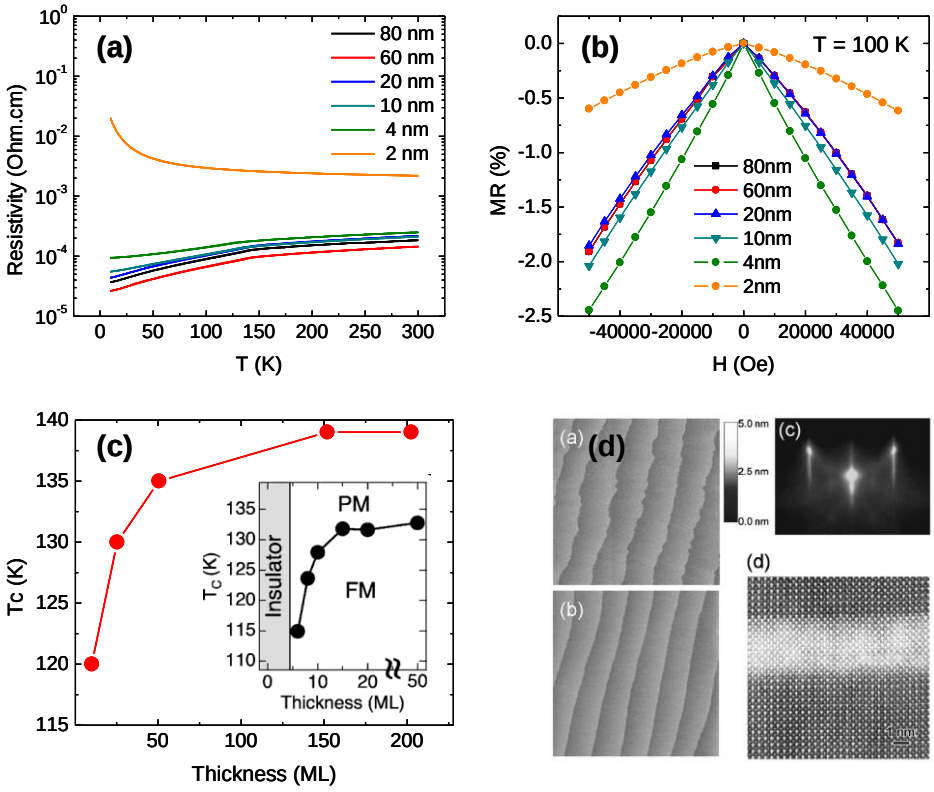

Figure 5-6 Thickness dependent transport (a) and magnetoresistance (b) on thin SRO. The thickness effect on magnetic transition temperatures agrees with previously data reported by D.Toyota et al. [25]. (d)AFM images taken from our atomically-flat SRO film on a $SrTiO_3$ substrate – scan size is 3×3 μm^2, RHEED pattern and cross-sectional Z-STEM reveal the high quality and sharp surface [26].

High quality ferroelectric thin films especially with a high polarization are also significant part of the structure and play a role as passive layers. Tetragonal lead zirconate titanate is the material of choice due to its high polarization and to a good lattice mismatch to the STO substrate. The CMR manganites, as active materials in the FE field-effect, have as high as ~10^{19}-10^{22} cm^{-3} carrier densities. This means that as many as tens of μC per each cm^2 polarization is necessary in order to significantly modify the manganite doping level (Figure 5-7).

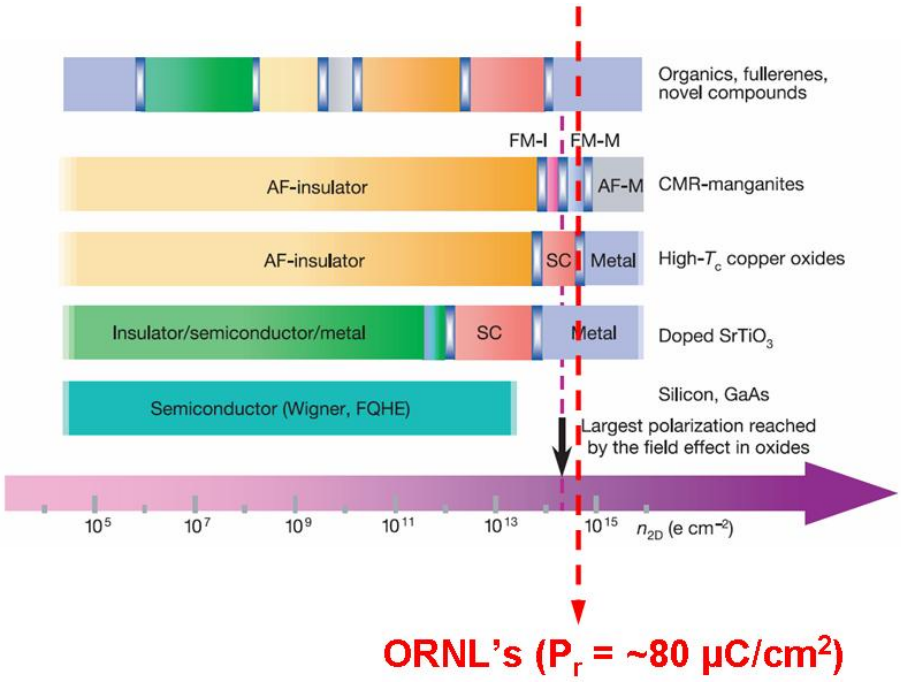

Figure 5-7 Charge carrier sheet density of different correlated systems [27]. It illustrates the polarization of about 80 μC/cm^2 we can induce is above the ones reported so far [29].

The highly polar PZT we are able to deposit has an exceptional remanent polarization of about 80 μC/cm^2, which is amongst the highest ever reported. These ferroelectric films are grown epitaxially on SRO electrodes with almost free of defects and dislocations due to the coherent growth. The coercive voltage is low enough for FET operations. It makes the polarization convenient to switch. The extraordinary improvement in the quality, compared to other reports on PZT by PLD,[28] is the constant saturation polarization independent of the thickness.

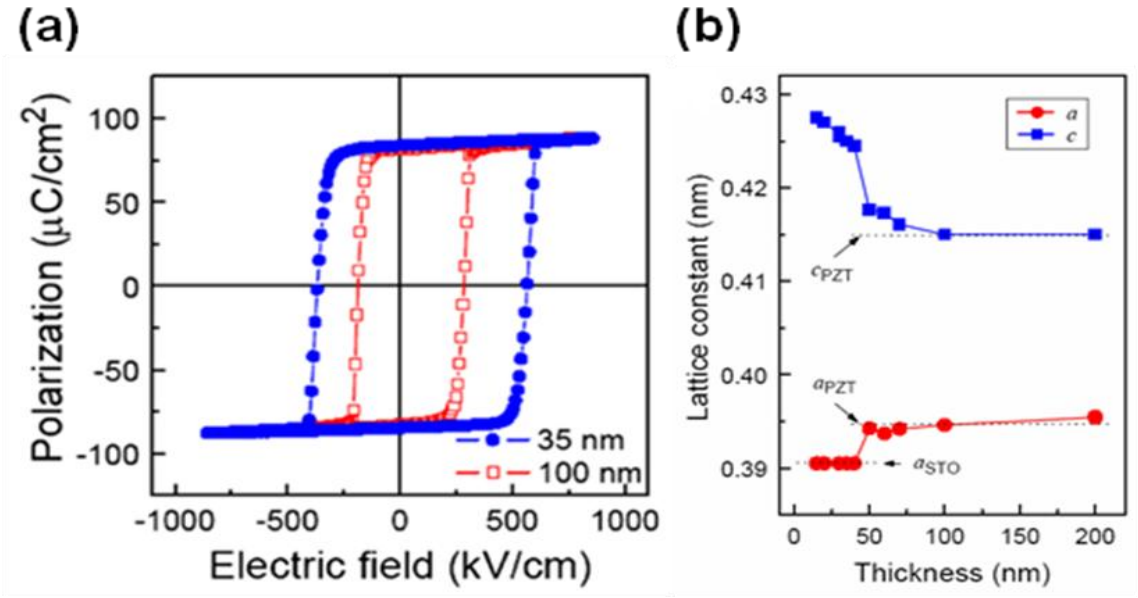

Figure 5-8 Ferroelectric polarization loops measured at 100 Hz. The remanent polarization remains the same with thickness regardless of the strain state (b) [29].

Adjusting the ferroelectric film thickness can modify the switching voltage. However, just as in the case of SRO, ferroelectric thin films get also altered when reducing their

dimension. It has often been reported that ferroelectrics and linear insulators[30] fail to reach their bulk dielectric constant in the form of thin film. It is partially due to the incomplete screening in the metallic layer used for the capacitor structure. The other reason is what is called the dead-layer which refers to an electrically inactive portion in the insulator. The nominal dielectric constant is reached in the middle of the film resulting in strongly reduced dielectric response measured.[31] This phenomenon also results in reduced saturation polarization in thin ferroelectric films which was demonstrated experimentally after the theoretical prediction.[32] Although this problem has not shown up in our PZT films we need to verify it if later scaling down the devices becomes an issue.

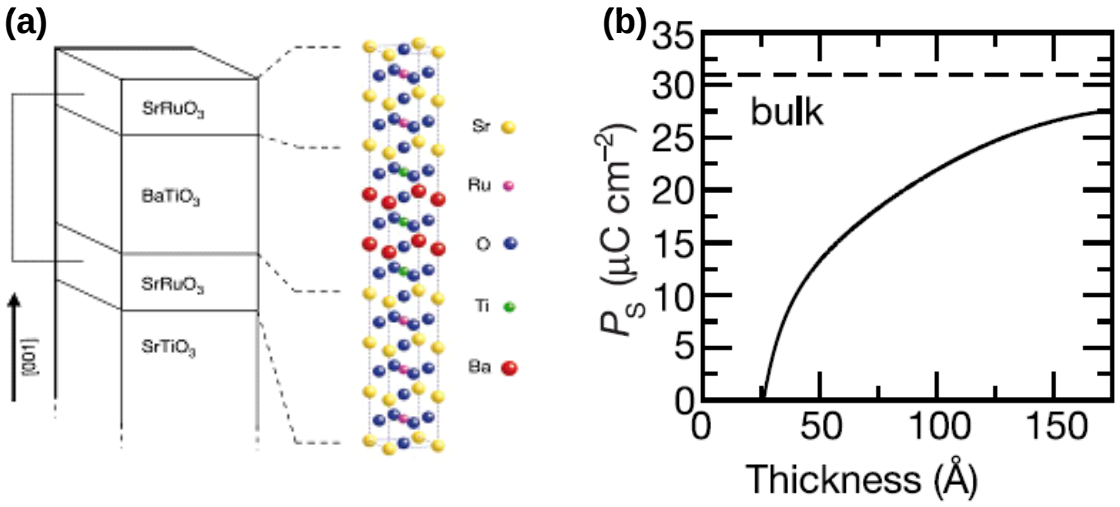

Figure 5-9 Calculations in ultra thin $BaTiO_3$ films show reduction in the saturation polarization due to a strong depolarizing field created by oxide metal-ferroelectric interface [32].

The manganite on the top of the structure is supposed to be as close to the critical 0.17 doping as possible. While a whole range of compositions was tested as channel layers, we first focused on x = 0.2, whose target for the PLD deposition is commercially available.

In the form of thin film, the phase diagram can become strongly modified or completely changed. New critical parameters coming into play are strain[33], thickness,[34,35] or off-stochiometry induced by oxygen vacancies.[36] In fact, these parameters themselves are already coupled. Thickness influences whether the film is strained or relaxed. Vacancies modify the average lattice constant and so the internal stress which strongly alters the magnetic coupling or the conducting state.

I grew several LSMO films to find the right growth conditions as well as to see the thickness effect on magnetic and transport properties. X-ray diffraction, conduction and magnetic measurements helped find the right growing conditions. Figure 5-10 shows how the increasing growing pressure flips the film from insulator to metallic at low temperatures. It is also found that the thickness effect is very strong as well.

The manganite films show an insulating behavior at low temperature when they are grown rather thin as shown in Figure 5-10(b). A similar metal to insulator transition has been reported[35] but not explicitly explained. More interestingly, in our case, this transition temperature is not constant as in Ref. [35] but varies with the thickness. It may be due to charge ordering tendency, which has not been found in bulk materials (Figure 5-1). Therefore, the effect of thickness on the magnetic and transport properties in ultrathin films needs further study.

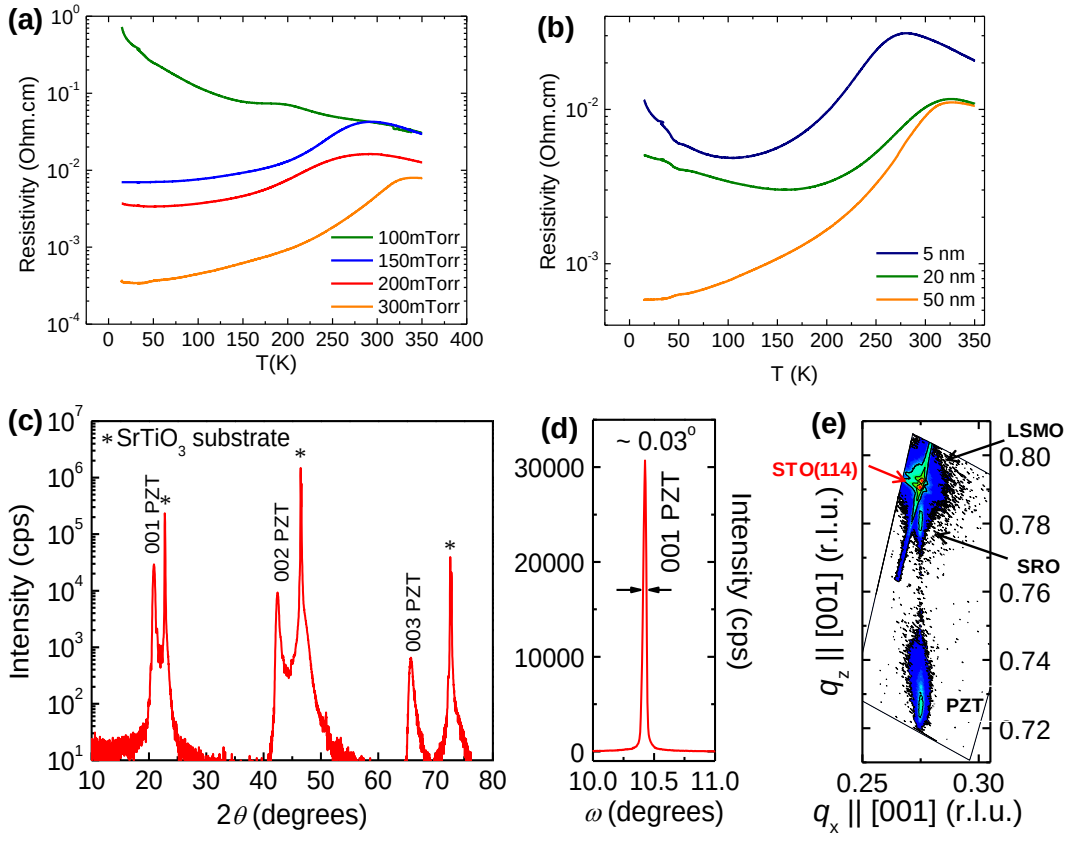

Figure 5-10 100 nm thick LSMO films grown at different oxygen pressures show insulator-to-metal switching at low temperature (a). Thickness effect shows up a different way from that reported by Jin [35]. The heterostructures I grew exhibit perfect epitaxial feature I verified by *θ-2θ* (c), *ω* rocking curve (d) and reciprocal space scans by X-ray (e).

By using these thin films, we have grown heterostructures of LSMO/PZT/SRO on a $SrTiO_3$ substrate. As shown in Figure 5-10(c-e), the resulting structure is of high quality with coherent in-plane lattices, verified by reciprocal space X-ray mapping. The

crystallinity of the heterostructure is also as high as the substrate one with full-width at half maxima below 0.04º in ω scan).

First, I wanted to find out what if a structure similar to that shown in Figure 5-4 is grown to measure ferroelectric field effect like in Ref. [22]. I used 100 nm PZT film as gate ferroelectric, and instead of 50 nm LSMO, I grew only 20 nm. It was necessary because of the short screening length predicted from Thomas-Fermi screening calculations (1-2 u.c.). The thinner the LSMO film is the bigger effect we expect. On the other hand, to keep bulk-like physical properties, the thickness should not be too small, since it shifts the high temperature insulator-to-metal transition temperature as well as introduces a low temperature metal-to-insulator transition while cooling as depicted in Figure 5-10 (b).

I deposited 20 nm $La_{1-x}Sr_xMnO_3$/100 nm PZT/10 nm SRO/STO heterostructures with compositions of x = 0.12, 0.16 and 0.45 by co-deposition of the commercially available targets. Then I fabricated 100 μm×400 μm devices with platinum electrodes connected to the PPMS puck by using wedge wire bonder technique. This technique involves a wedge pushing down the aluminum wire onto the platinum pad before applying ultrasound through the wedge. The ultrasound locally melts the wire and makes the metallic bond. However, the combination of strong pressure and intense ultrasound seem to damage the sample surface in our case as Figure 5-11 depicts.

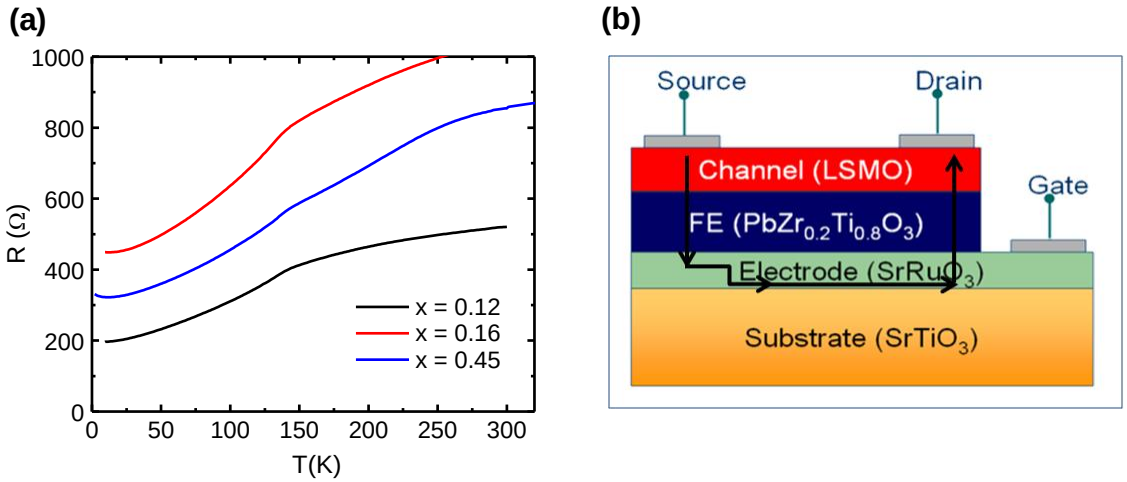

Figure 5-11 Electronic transport data on LSMO/PZT/SRO/STO structures show mainly contribution from the bottom electrode ruthenate with a tiny feature coming from the LSMOs on the top (a). It indicates that the measurement current flows through the bottom electrode (b).

The current goes straight through the PZT and SRO giving us the typical SRO resistance-temperature dependence (*cf.* Figure 5-6).

5.4.2 $La_{0.8}Sr_{0.2}MnO_3$ / $Pb(Zr_{0.2}Ti_{0.8})O_3$ / $La_{0.875}Sr_{0.125}MnO_3$ / $SrTiO_3$

In order to prevent the current from going through the entire heterostructure, I needed to pattern and etch the bottom electrode so that it does not interfere with the measurement of the top layer's resistivity. However, $SrRuO_3$ cannot be etched; also wet etching treatment would degrade its superior conduction properties. I needed to use a material which is conducting enough to be used as bottom electrode but also easy to etch.

Low doped LSMOs are widely used electrodes. So that I avoid the complication mentioned above I needed x < 0.2 composition. I deposited 10 nm $La_{0.875}Sr_{0.125}MnO_3$ (LSMO-0.125), which has much less conduction than the x = 0.2 composition and can be used as bottom electrode. I had defined and etched stripes of LSMO-0.125, before the PZT and LSMO-0.2 layers were grown. Using a contact aligner I fabricated clover shaped van der Pauw structure on the upper layer as shown in Figure 5-12.

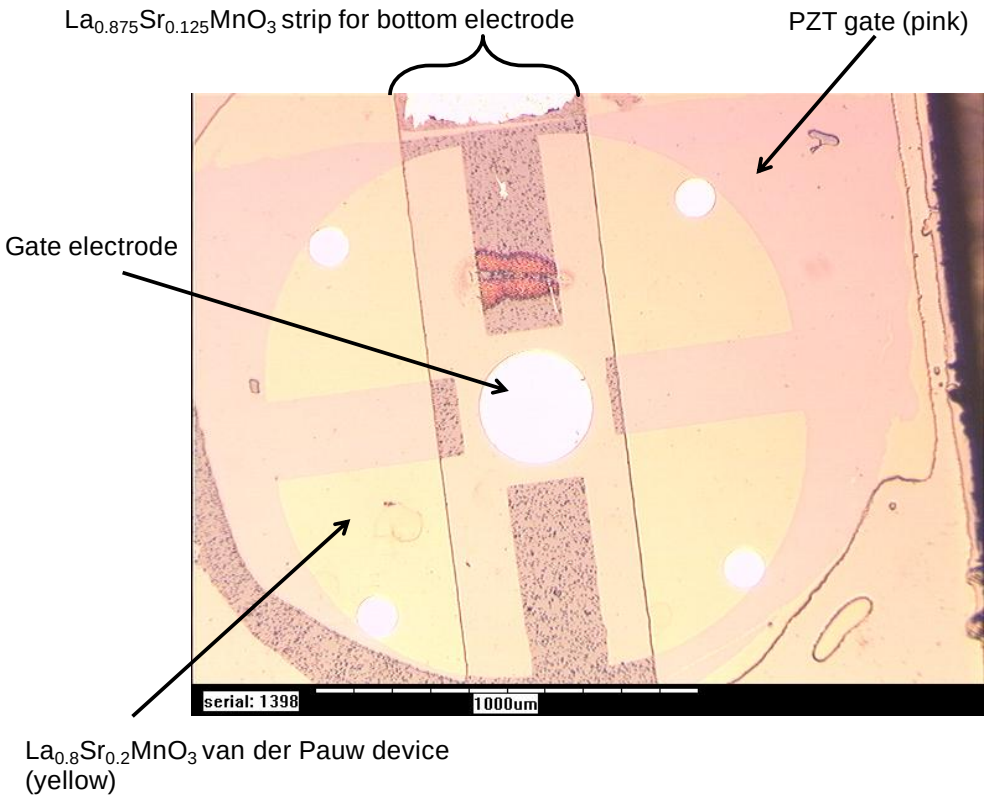

Figure 5-12 Optical microscope image of the clover shaped van der Pauw structure used to carry out ferroelectric field effect experiments on a $La_{0.8}Sr_{0.2}MnO_3$ / $Pb(Zr_{0.2}Ti_{0.8})O_3$ / $La_{0.875}Sr_{0.125}MnO_3$ / $SrTiO_3$ heterostructure.

In the middle of the structure I created a circular top electrode with the diameter of 100μm to be able to pole the ferroelectric. This design completely eliminated the possibility of shorting the device through the bottom electrode but made possible to bias a big portion of it which was going to let us see a ferroelectric field effect induced change in the resistance of the top LSMO layer. The results are shown in Figure 5-13.

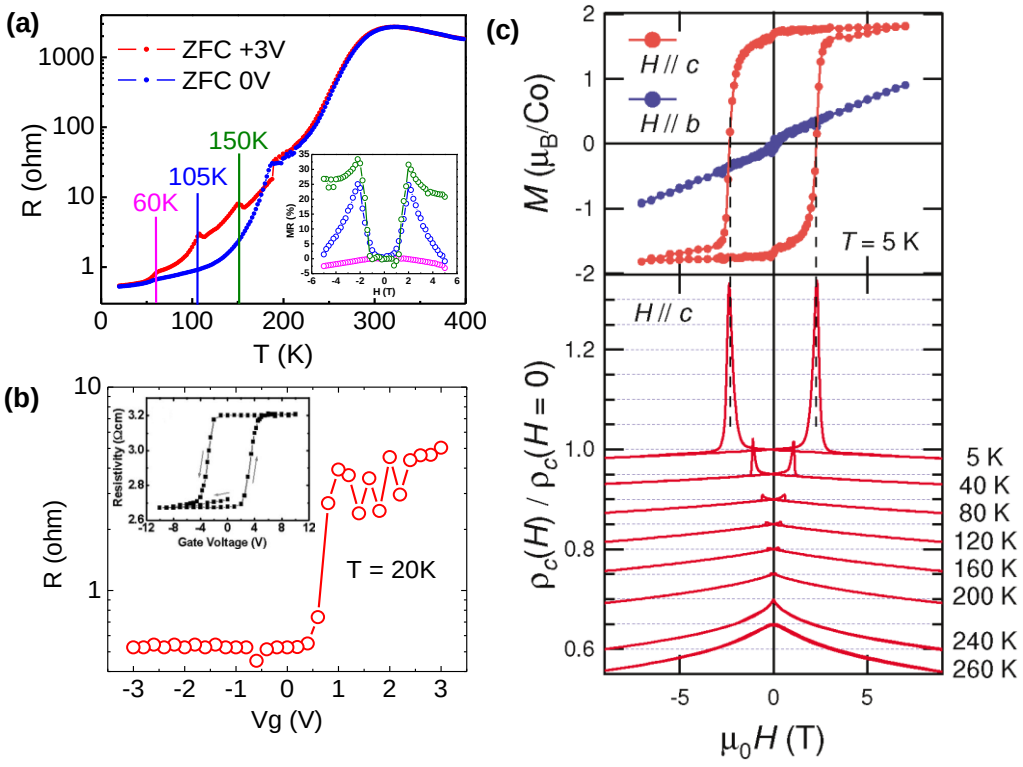

Figure 5-13 Transport data on the 20 nm LSMO / 100 nm PZT/ 10 nm SRO heterostructure (a) shows a structural transition at 200K occurring in the unbiased and biased film as well. The inset displays magnetoresistance plots at 60 (magenta), 105 (blue) and 150K (green), which are similar to those (c) seen in Sr_2CoO_4 films [37]. Gate poling voltage scan at 20K (b) provided us with a significant one order of magnitude change compared to room temperature data (see inset, Ref. [22]).

The as-grown sample shows the normal insulator to metal transition, while it was cooled down. There is a probably structural transition at 200K, which is expected at a lower temperature of about 100K at x = 0.2 strontium doping level. The difference can be associated to thickness induced strain. After cooling down the structure unbiased, I switched on the biasing gate voltage of +3V for about 1 millisecond to pole the ferroelectric gate, then swept the temperature back up while taking transport data on the manganite film. As one can see, in the biased measurement there are three extra transitions showing up at 60, 105 and 150K. Also, at least at lower temperatures, the biased and unbiased curves are fairly different, which must have been caused by the ferroelectric field effect. I took magnetoresistance data at the anomalous peaks. The MR features seem quite unique and shown by the inset of Figure 5-13 (a). At 105K and 150K the MR scans have two distinct peaks at around 2 Tesla and a magnetic gap in-between, where the MR is close to zero. The low temperature anomalous dip at 60K shows a normally expected negative magnetoresistance.

This behavior has not been understood yet but similar features were recorded in epitaxial (001) Sr_2CoO_4 grown on (001) $LaSrAlO_4$ substrate by pulsed laser deposition (Figure 5-13 (c)) at low temperatures.[37] It showed up in the out-of-plane magnetotransport measurement and was interpreted as the result of inter-domain tunneling. In the case of Sr_2CoO_4, the MR anomaly occurs exactly at the coercive field; however, the coercive field of our 20 nm LSMO-0.2 film is about 0.5 Tesla and the unique peaks show at 2 Tesla.

5.4.3 $La_{0.8}Sr_{0.2}MnO_3$ / $Pb(Zr_{0.2}Ti_{0.8})O_3$ / $SrTiO_3$

At this point it is clear, that we need to refrain from using SRO bottom electrode for demonstration purposes of the ferroelectric field effect, otherwise the current passes through the lowest resistive path and reads out the SRO's conduction state with a tiny LSMO signal superimposed on it.

However, there is a phenomenon observed in tetragonal PZT thin films, like our $Pb(Zr_{0.2}Ti_{0.8})O_3$, which can be helpful. It was found that as-grown PZT has a very strong and stable built-in polarization.[38,39] This self-polarization effect does not manifest, though, in the rhombohedral phase.

If this effect exists in the PZT films we grow then one can simply exclude the switching part of the ferroelectric field effect. A stable and well-defined built-in polarization after growth means, that we can grow LSMO on the top and below the PZT layer exposing it to interfaces, which are positively or negatively charged. This way we can map the changes in the LSMO electronic transport when the hole accumulation and hole depletion regions.

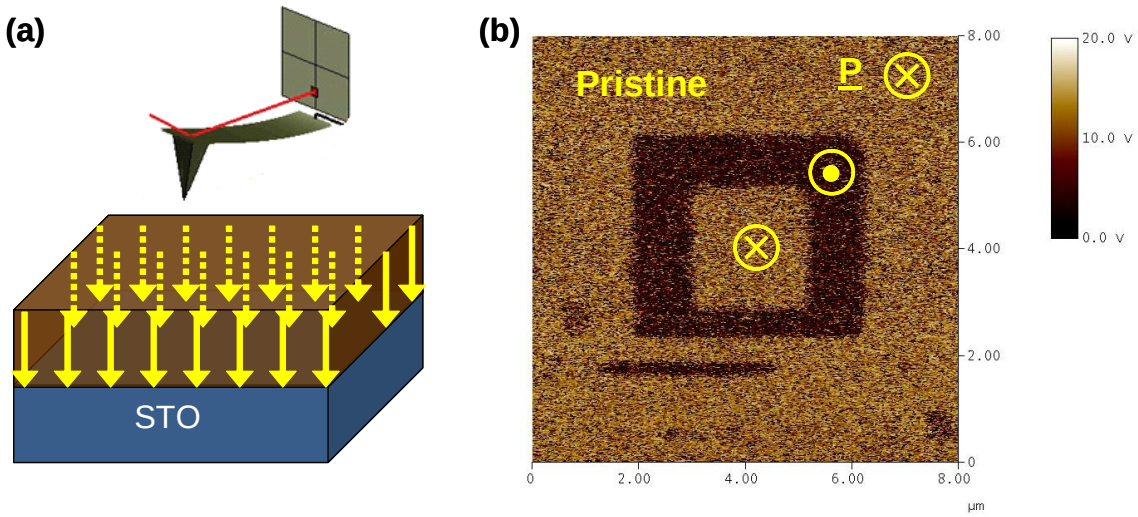

Figure 5-14 Schematics of the PFM experimental setup (a) and the actual scan on an area of 8μm×8μm (b). The pristine sample shows the same contrast the positively biased tip induced on the surface indicating that the as-grown PZT has intrinsic downward polarization.

In order to verify the self-polarizing effect, I grew 30 nm PZT / 5 nm LSMO-0.2 / STO bilayer for piezoresponse force microscopy studies. The LSMO was used as bottom electrode while the PFM's tip served as top electrode. A small alternating voltage was applied on the tip while the tip deflection phase was imaged to get information about the polarization of the PZT film (for more details see Section 3.3.2). First the sample was scanned on a 8μm×8μm area without any DC bias on the tip (see Figure 5-14 (b)). Then -3.5V was used on the tip to pole the ferroelectric polarization pointing upwards on a 4μm×4μm area in the middle, before again scanned without DC bias. The phase image is dark brown and corresponds to polarization pointing up. In the middle of the dark brown square again a +3.5V was put on the tip and it flipped the polarization pointing down.

The unbiased phase image showed up as light brown, exactly the same as the pristine sample. This allowed us to conclude, that the as-grown sample, indeed, has a built-in polarization pointing down. Several scans on different areas of the sample confirmed, that it is the case along the entire 5 mm × 5 mm sample.

In order to test if the concept works, I synthesized 5nm test films of LSMO-0.2 and LSMO-0.5 alone on STO, as well as on and below 30nm PZT film.

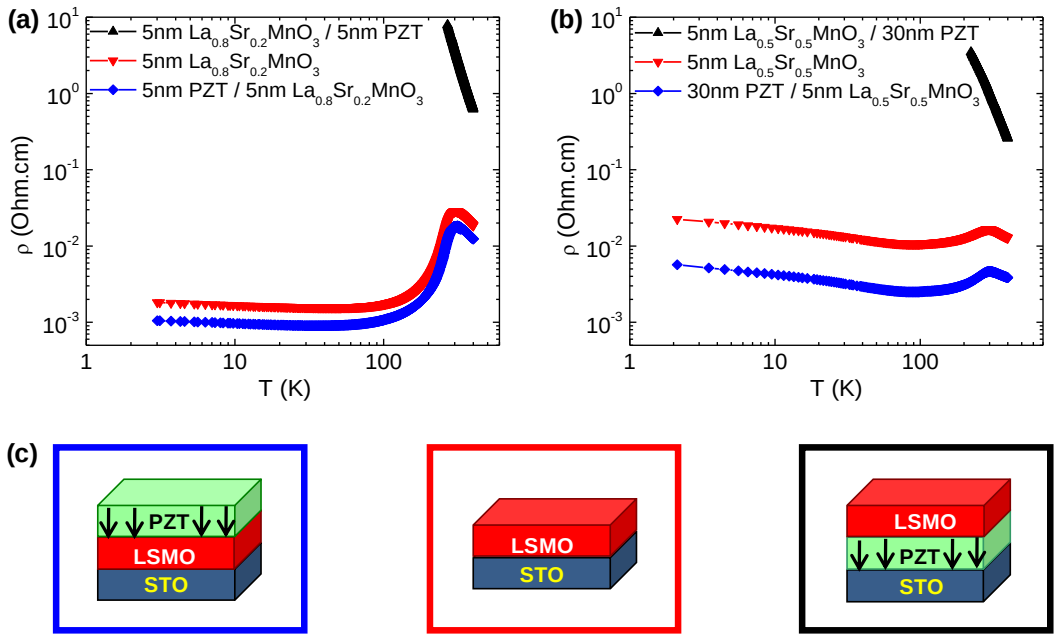

Figure 5-15 Resistivities of LSMO, LSMO/PZT/STO and PZT/LSMO/STO structures with Sr doping level of (a) x = 0.2 and (b) x = 0.5. The investigated structures are sketched on (c). The frames' colors correspond to the data points' colors on (a) and (b).

As Figure 5-15 shows, whenever the ultrathin 5nm LSMO film is grown on the top of 30 nm PZT, it turns into completely insulating, while below the PZT and on its own it

displays the normally expected metal-to-insulator behavior. It is known, that the surface of PZT is getting rougher as thickness is increased and above about 100 nm even domain boundary formation makes this effect stronger. In order to deal with much smoother interfaces, I needed to go down with the PZT thickness, so that it stays well strained as well as mimics the substrate surface.

Based on this observation several sets of three samples using different LSMO compositions were deposited on (001) single crystalline $SrTiO_3$ substrates: a reference single film of 5 nm LSMO, 5 nm LSMO below 5 nm PZT (PZT/LSMO) and 5 nm LSMO on 5 nm PZT (LSMO/PZT) as drawn in Figure 5-15 (c).

In the case of x = 0.125 and x = 0.33 strontium doping some differences can be resolved between the structures. The 1/8 doped film shows clear metal-to-insulator transition when grown under PZT while the pristine 5nm LSMO shows low band gap insulator nature. The one put on the top of PZT turns out to be entirely insulating (Figure 5-16 (a)). Since this situation is supposed to be the hole accumulation region, the measurement outcome is quite puzzling. Also the x = 0.33 sample turns into insulating when grown on PZT, while not much effect is gained in the hole accumulation scenario as Figure 5-16 (b) depicts.

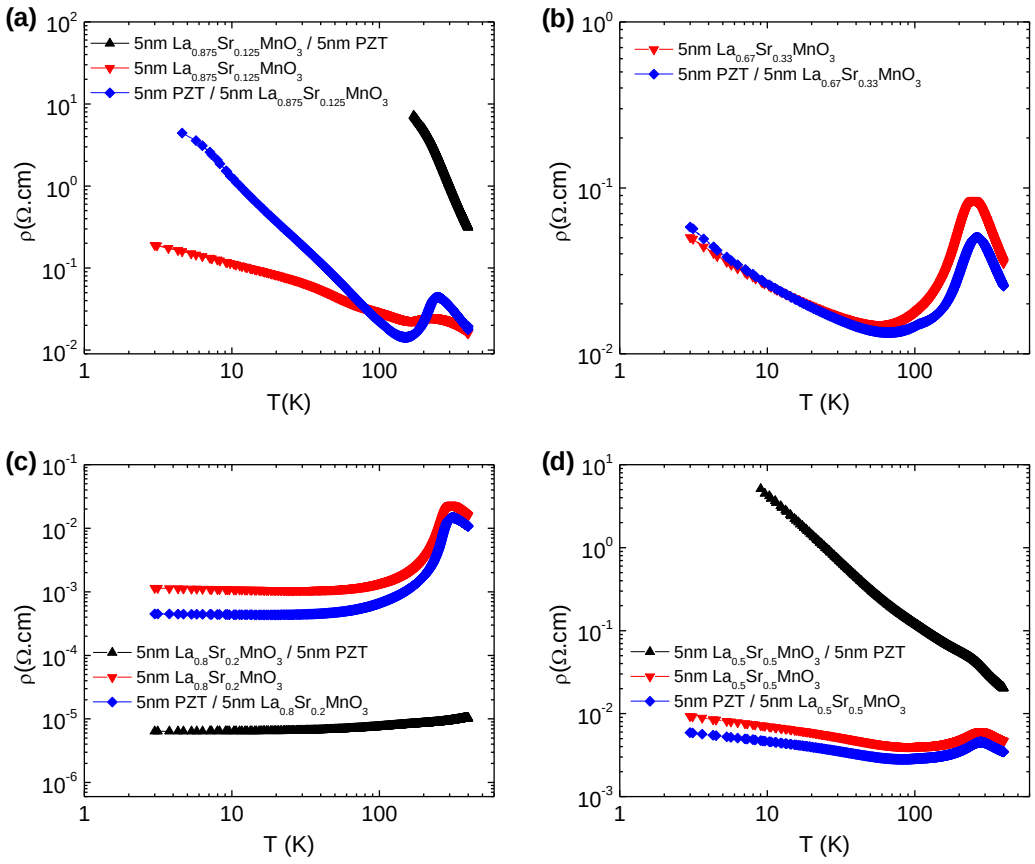

Figure 5-16 Resistivities of pure LSMO, LSMO/PZT/STO and PZT/LSMO/STO structures with Sr doping level of (a) x = 0.125, (b) x = 0.33, (c) x = 0.2 and (d) x = 0.5. In these cases 5nm PZT and 5nm LSMO were tested. The x = 0.33 sample grown on PZT was too insulating to measure.

The x = 0.2 and 0.5 samples were of special interest since they are in the vicinity of low temperature metal-to-insulator transitions, where the most pronounced effects are expected. As Figure 5-16 (c) shows, we have a huge change in the conductivity of LSMO-0.2 induced by the PZT. The single LSMO film and the PZT/LSMO structure

with the presumably hole depleted interface have very similar behavior. However, grown as a top layer (hole accumulated interface), the resistivity drops to an incredible 7×10^{-6} Ω·cm at low temperature, which is the lowest value ever reported in this material. At the high temperature MIT the modulation is as high as three orders of magnitude. Also, the hole accumulated manganite film has an unprecedented metal-to-insulator transition at around 398K, which has never been seen on the bulk phase diagram. Its T_c is closest to that of x = 0.35 doping level.

Figure 5-16 (d) demonstrates that the field effect does work very well on the other side of the phase diagram, nearby the critical x = 0.5 doping, beyond which the doped manganese oxide transforms into anti-ferromagnetic metallic, then at around x = 0.55 into anti-ferromagnetic insulator at low temperature, like shown in Figure 5-17.

The x = 0.55 doped bulk shows a kink at around 200K, which also shows up in our electrostatically modified layer. It is the Curie temperature of this composition. So one can conclude that based on the electronic transport data, the field effect tuned our initial x = 0.5 manganite to x = 0.55. The magnitude of the modulation is again enormous: three orders of magnitude at low temperature and a factor of ten at room temperature, at the same time.

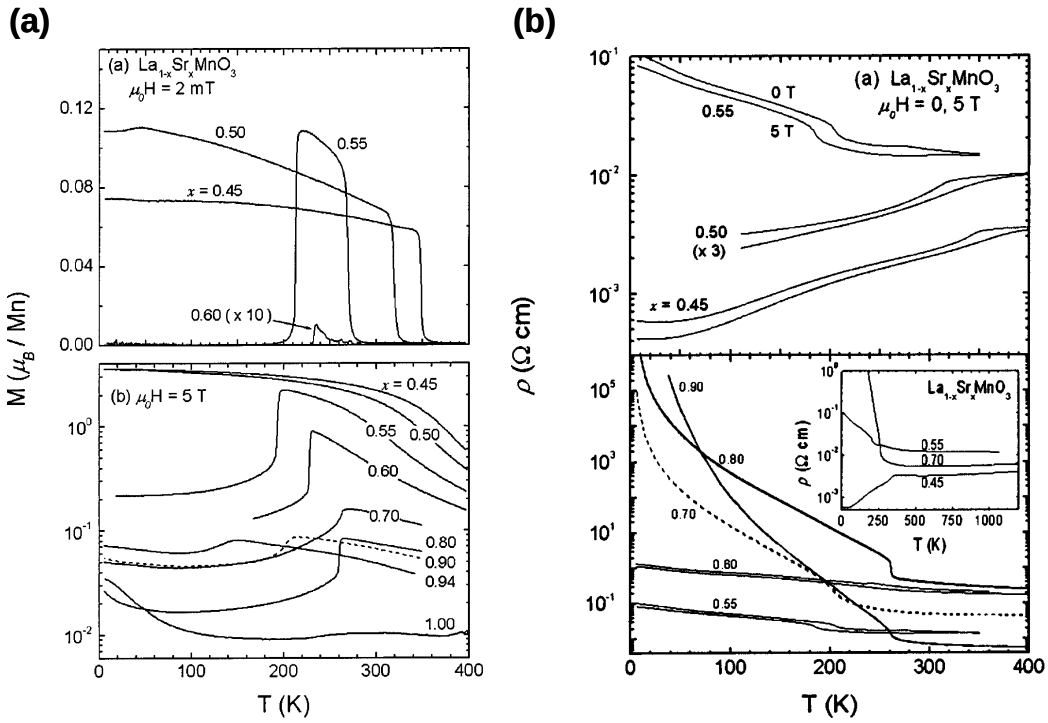

Figure 5-17 Magnetism (a), ZFC on the upper panel, FC in 5 Tesla on the lower one, and electronic transport data on LSMO in the doping range of 0.45 < x < 0.90 from Ref.[40].

The sets of three samples with x = 0.2 and 0.5 were tested in the SQUID as well to find out more about their magnetic properties. The *M*(T) curves of the 5nm $La_{0.8}Sr_{0.2}MnO_3$ and the 5nm $Pb(Zr_{0.2}Ti_{0.8})O_3$ / 5nm $La_{0.8}Sr_{0.2}MnO_3$ heterostructure are very similar with a ferromagnetic T_C of about 300K, while the hole accumulated film shows very high T_c of 390K matching the unusually large MIT temperature (Figure 5-18 (a)). Surprisingly however, the net magnetic moment at low temperatures drops about 30% compared to the two other samples and the difference grows with temperature to about 250% at T_c. Since internal magnetism enhances the charge carrier density in this

material, we can speculate that the mobility was enhanced by ferroelectric field effect by creating a very pure metallic interface between the PZT and the LSMO. In order to conclude it, though, further experiments are needed. All the samples preserve the typical low temperature soft ferromagnetic nature as verified by *M*(H) loops in Figure 5-18 (b).

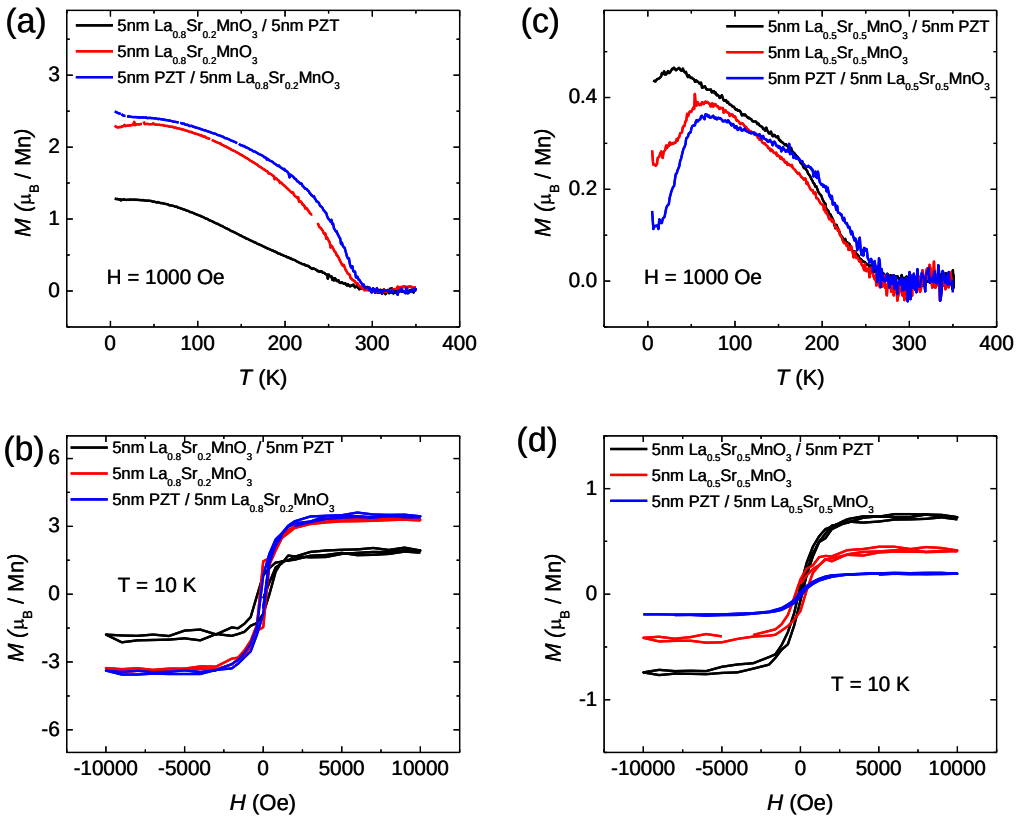

Figure 5-18 Magnetic data as a function of temperature and applied magnetic field on x = 0.2 (a)-(b) and x = 0.5 (c)-(d). The cooling was done in H = 1000 Oe to enhance the signal.

Similarly *M*(T) and *M*(H) curves were taken on the $La_{0.5}Sr_{0.5}MnO_3$ heterostructure family as well. The 5nm $La_{0.5}Sr_{0.5}MnO_3$ and the 5nm $Pb(Zr_{0.2}Ti_{0.8})O_3$ / 5nm $La_{0.5}Sr_{0.5}MnO_3$ had the same T_c of about 300K, but the hole accumulated manganite layer on the top had a lower 250K ferromagnetic order temperature. Upon further cooling, all samples went through a presumably anti-ferromagnetic transition. While the LSMO-0.5 and PZT/LSMO-0.5 had the same Néel temperature of 65K, the LSMO-0.5/PZT had a magnetization peak at 35K. If one compares these magnetic data with the ZFC measurements done on single crystalline LSMOs shown by the upper panel of Figure 5-17 (a), it support the picture, that the LSMO-0.5 film grown on the top of the PZT behaves like the x = 0.55 doped LSMO.

Recent first principle calculation[41] on $La_{0.5}A_{0.5}MnO_3/BaTiO_3$ (LAMO/BTO) interfaces claim, that the ferroelectric field in the manganite induces Mn-O displacement to screen the field, which leads to anti-ferromagnetic correlations in the 1-2 u.c vicinity of the interface, when the manganite is "hole accumulated" but stays magnetically intact in the opposite state. The BTO polarization was assumed to be 50 $\mu C/cm^2$. This result contradicts my results on LSMO-0.5, since I observe a little net magnetic moment enhancement at low temperature in the hole accumulated regime as well as sinking Néel temperature, *e.g.* weaker tendency for forming anti-ferromagnetic correlations.

Nevertheless, other experimental works, such as magneto-optical Kerr effect[42] or near edge x-ray absorption spectroscopy (XANES)[43] show the same effect (dropping interfacial magnetic moment, when holes are accumulated at the interface) in the case of

LSMO-0.2/PZT heterostructures. These data were also modeled by spin order modification directly at the interface. In the LSMO-0.2 case, I also recorded magnetic moment drop but it is way more than reported in Refs. [42] and [43]. At low temperature the change I measured was 30%, which cannot be explained by magnetic reconstruction in 1 unit cell.

I think the key point to arrive at a more reasonable model is the fact, that although these manganites have huge charge carrier densities, they are still spatially distributed a non-uniform way. As mentioned above, the doped charges percolate rather on a one dimensional path, as conduction sets in. Thus the doped charges in the mixed-valent manganites can be rather imagined as a network of conducting filaments on separate Mn-O planes, than a uniformly doped piece of metal sheet. It means that the ferroelectric field may penetrate even more, than a unit cell into the LSMO modifying much larger portion on the thin film, than previously thought. For this purpose, further model calculations are needed to be carried out.

5.5 Summary and Outlook

In this chapter the high degree of resistance modulation in doped manganites by ferroelectric field effect was demonstrated. A low temperature metal-to-insulator transition occurs when about 17% and 50% of the La is replaced by Sr (or Ca in

$La_{1-x}Ca_xMnO_3$) in bulk materials. The non-linear change of conduction by supplying additional carriers from ferroelectric polarization in the vicinity of MIT of manganite layers expected to give rise to a dramatic mobility change. High quality epitaxial LSMO/PZT heterostructures on SRO coated STO and pure STO substrates have been prepared for this study. The PZT's exceptionally high polarization was able to largely modulate the resistivity and magnetization in LSMO.

I aimed at tuning LSMO thin films around the low temperature ferromagnetic metallic-to-ferromagnetic insulator phase transition by using ferroelectric field-effect and see how conduction and magnetism change in the critical region. One of the challenges was to establish a reliable way to demonstrate an effect on such high charge carrier density with a relevant magnitude. I succeeded in measuring an effect of three orders of magnitude, which has never been seen before.

In the future, the demonstration of switching between the different conductions states is needed. All the properties are planned to be examined as a function of strain state by growing on different substrates; of thickness to gain information about the true screening length and dopant composition in these doped manganites as well as high temperature superconductors.

A further goal of the research is to set up an experiment to image the doped holes' network on the surface of the manganite under planar bias, using scanning tunneling microscopy (STM). There has been successful work on imaging hole-states on doped manganite surface by STM technique.[44]

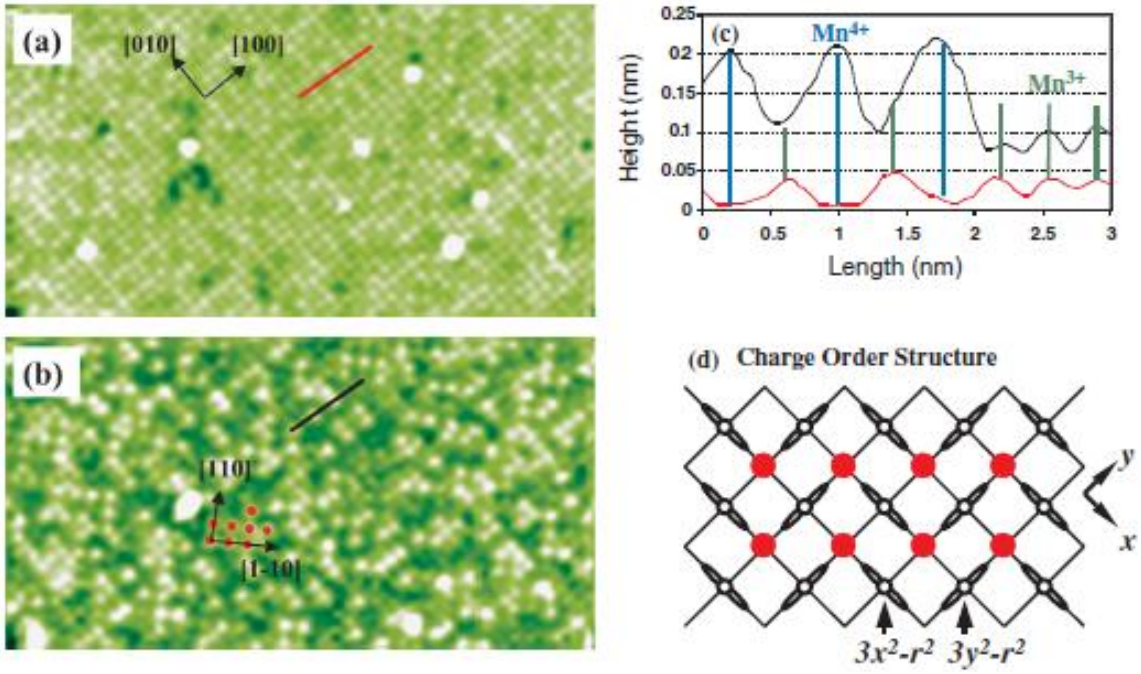

Figure 5-19 Visualization of doped holes in $(La_{5/8-0.3}Pr_{0.3})Ca_{3/8}MnO_3$ thin film by scanning tunneling microscopy from Ref. [44].

Visualization of doped chains between metallic contacts would be a great result to support the filamentary conduction picture.

The ferroelectric field effect technique may be useful tool for switching between different conduction states in oxide superlattices, which offer a new template in oxide electronics. Ever since high mobility conduction was discovered on the interface between the two insulators $LaAlO_3$ (LAO) and $SrTiO_3$ (STO), the system has been extensively studied by many groups.[45,46,47] Correlation studies between optical and *dc* mobility

measurements suggest that there are two types of carriers contributing to the interfacial properties.[48]

Interfacial electronics of these materials can be studied by growing superlattices and measuring the interfacial conduction. A shown in Figure 5-20, these artificial lattices switch between conductive states, based on periodicity and the thickness of the building blocks.

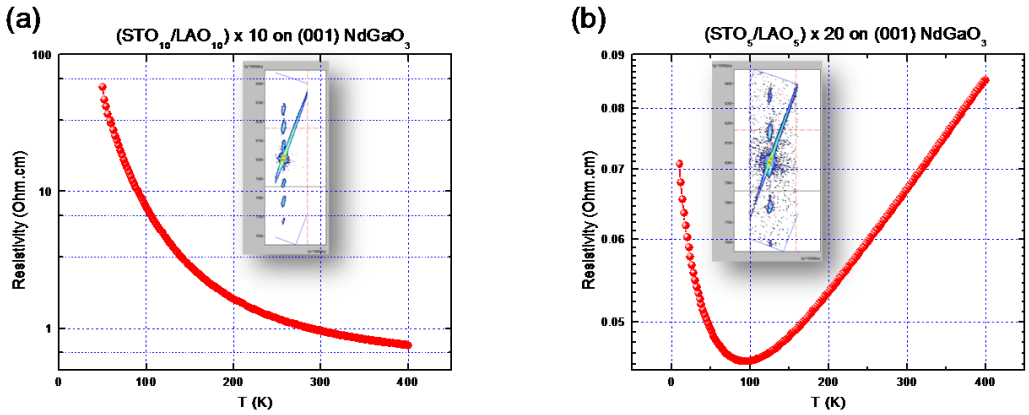

Figure 5-20 STO/LAO superlattices of different stacking on (001) $NdGaO_3$ substrate show dissimilar conduction as a function of temperature. The insets are reciprocal space maps revealing perfect epitaxial nature by clear superlattice reflections aligned with the STO (114) peak.

Ferroelectric field effect applied on these structures by PZT would be another interesting direction to see emerging interfacial phenomena in perovskite oxide heterointerfaces.

References

[1] A. Cassinesse, G.M. De Luca, A. Prigiobbo, M. Salluzzo, and R. Vaglio, Appl. Phys. Lett. **84** (19), 3933 (2004).

[2] C.H. Ahn, S. Gariglio, P. Paruch, T. Tybell, L. Antognazza, and J.M. Triscone, Science **284**, 1152 (1999).

[3] X. Hong, A. Posadas, A. Lin, and C.H. Ahn, Phys. Rev. B **68** (13), 134415 (2003).

[4] T. Zhao, S.B. Ogale, S.R. Shinde, R. Ramesh, R. Droopad, J. Yu, K. Eisenbeiser, and J. Misewich, Appl. Phys. Lett. **84** (5), 750 (2004).

[5] S. Mathews, R. Ramesh, T. Venkatesan, and J. Benedetto, Science **276**, 238 (1997).

[6] X. Hong, A. Posadas, and C.H. Ahn, Appl. Phys. Lett. **86**, 142501 (2005).

[7] C. Thiele, K. Dorr, O. Bilani, J. Rodel, and L. Schultz, Phys. Rev. B **75**, 054408 (2007).

[8] M.F. Hundley, M. Hawley, R.H. Heffner, Q.X. Jia, J.J. Neumeier, J. Tesmer, J.D. Thompson, and X.D. Wu, Appl. Phys. Lett. **67**, 860 (1995).

[9] G. Jakob, F. Martin, W. Westerburg, and H. Adrian, Phys. Rev. B **57**, 10252 (1998).

[10] T. Kanki, T. Yanagida, B. Vilquin, H. Tanaka, and T. Kawai, Appl. Surf. Sci. **244**, 481 (2005).

[11] D.B. McWhan, T.M. Rice, and J.P. Remeika, Phys. Rev. Lett. **23** (24), 1384 (1969).

[12] S. Jin, T.H. Tiefel, M. McCormack, R.A. Fastnacht, R. Ramesh, and L.H. Chen Science **264**, 413 (1994).

[13] J.G. Bednorz and K.A. Muller, Zeitschrift fur Physik B, **64** (2), 189 (1986).

[14] E. Dagotto, T. Hotta, and A. Moreo, Phys. Rep. **344**, 1 (2001).

[15] A. Urushibara, Y. Moritomo, T. Arima, A. Asamitsu, G. Kido, and Y. Tokura Phys. Rev. B **51** (20), 14103 (1995).

[16] Y. Moritomo, A. Asamitsu, Y. Tokura, Phys. Rev. B **56** (19), 12190 (1997).

[17] D. Louca and T. Egami, Phys. Rev. B **59**, 6193 (1999).

[18] J.C. Phillips, Proc. Natl. Acad. Sci. USA **94**, 10528 (1997).

[19] J.C. Phillips, Phys. Rev. B **71** (18), 184505 (2005).

[20] K.M. Itoh, E.E. Haller, J.W. Beeman, W.L. Hansen, J. Emes, L.A. Reichertz, E. Kreysa, T. Shutt, A. Cummings, W. Stockwell, B. Sadoulet, J. Muto, J.W. Farmer, and V.I. Ozhogin, Phys. Rev. Lett. **77** (19), 4058 (1996).

[21] J. Mannhart, Supercond. Sci. Technol. **9**, 49-67 (1996).

[22] R. Ramesh et al., APL 84, 750 (2004).

[23] C.H. Ahn et al., PRB 74, 174406 (2006).

[24] M. Kawasaki, K. Takahashi, T. Maeda, R. Tsuchiya, M. Shinohara, O. Ishiyama, T. Yonezawa, M. Yoshimoto, and H. Koinuma, Science **266**, 1540 (1994).

[25] D. Toyota, I. Ohkubo, H. Kumigashira, M. Oshima, T. Ohnishi, M. Lippmaa, M. Kawasaki, and H. Koinuma, J. Appl. Phys. **99**, 08N505 (2006).

[26] H.N. Lee, H.M. Christen, M.F. Chisholm, C.M. Rouleau, and D.H. Lowndes, Appl. Phys. Lett. **84** (20), 4107 (2004).

[27] C.H. Ahn, A. Bhattacharya, M. Di Ventra, J.N. Eckstein, C. Daniel Frisbie, M.E. Gershenson, A.M. Goldman, I.H. Inoue, J. Mannhart, A.J. Millis, A.F. Morpurgo, D. Natelson, and J. Triscone, Rev. Mod. Phys. **78**, 1185 (2006).

[28] M. Lisca, L. Pintilie, M. Alexe, and C.M. Teodorescu, Appl. Surf. Sci. **252**, 4549 (2006).

[29] H.N. Lee, S.M. Nakhmanson, M.F. Chisholm, H.M. Christen, K.M. Rabe, and D. Vanderbilt, Phys. Rev. Lett. **98**, 217602 (2007).

[30] C.A. Mead, Phys. Rev. Lett. **6**, 545 (1961).

[31] M. Stengel and N.A. Spaldin, Nature **443** (7112), 679 (2006).

[32] J. Junquera and P. Ghosez, Nature **422**, 506 (2003).

[33] V. Pena, Z. Sefrioui, D. Arias, C. Leon, J. Santamaria, M. Varela. S.J. Pennycook, M. Garcia-Hernandez, J.L. Martinez, J. Phys. Chem. Sol. **67**, 472 (2006).

[34] T. Kanki, T. Yanagida, B. Vilquin, H. Tanaka, and T. Kawai, Appl. Surf. Sci. **244**, 481 (2005).

[35] S. Jin, W. Wu, H.M. Weng, B.J. Ye, and X.Y. Zhou, J. Phys. D: Appl. Phys. **39**, 4125 (2006).

[36] J. Sakai, N. Ito, and S. Imai, J. Appl. Phys. **99**, 08Q318 (2006).

[37] J. Matsuno, Y. Okimoto, Z. Fang, X. Z. Yu, Y. Matsui, N. Nagaosa, M. Kawasaki and Y. Tokura, Phys. Rev. Lett. **93**, 167202 (2004).

[38] V.P.Afanasjev, A. A. Petrov, I. P. Pronin, E. A. Tarakanov, E. Ju. Kaptelov and J. Graul, J. Phys.: Condens. Matter **13**, 8755 (2001).

[39] R. Kochler, N. Neumann, Z. He, R. Bruchhaus, W. Wersing and M. Simon, Ferroelectrics **201**, 83 (1997).

[40] O. Chmaissem, B. Dabrowski, S. Kolesnik, J. Mais, J. D. Jorgensen and S. Short, Phys. Rev. B **67**, 094431 (2003).

[41] J.D. Burton and E. Y. Tsymbal, Phys. Rev. B **80**, 174406 (2009).

[42] H. J. A. Molegraaf et. al., Adv. Mater. **21**, 1-5 (2009).

[43] C. A. F. Vaz, J. Hoffman, Y. Segal, J. W. Reiner, R. D. Grober, Z. Zhang, C. H. Ahn, F. J. Walker, arXiv:1003.1752v1 [cond-mat.mtrl-sci]

[44] J. X. Ma, D. T. Gillaspie, E. W. Plummer, and J. Shen, Phys. Rev. Lett. **95** (23), 237210 (2005).

[45] A. Ohtomo and H. Y. Hwang, Nature (London) **427**, 423 (2004).

[46] S. Thiel, G. Hammerl, A. Schmehl, C. W. Schneider, and J. Mannhart,Science **313**, 1942 (2006).

[47] A. Brinkman, M. Huijben, M. van Zalk, J. Huijben, U. Zeitler, J. C. Maan,W. G. van der Wiel, G. Rijnders, D. H. A. Blank, and H. Hilgenkamp, Nature Mater. **6**, 493 (2007).

[48] S. S. A. Seo, Z. Marton, W. S. Choi, G. W. J. Hassink, D. H. A. Blank, H. Y. Hwang, T. W. Noh, T. Egami, and H. N. Lee, Appl Phys. Lett. **95**, 082107 (2009).

6. Giant Dielectric Permittivity and Magnetocapacitance in $La_{0.875}Sr_{0.125}MnO_3$ Single Crystals

This chapter is about the observation of unusually high dielectric permittivity exceeding 10^9 and magnetocapacitance of the order of 10^4% in $La_{0.875}Sr_{0.125}MnO_3$ single crystal. The phenomenon is measured below 270 K around a magnetic phase transition. This effect may be the consequence of strong competition and interplay among charge, orbital, and spin degrees of freedom, resulting in nanoscale charge and spin dynamic inhomogeneities in the pre-percolation regime of the phase segregation.

6.1 Introduction

The fascinating magnetic and transport phenomena observed in manganites is thought to be originated from the complex interplay and competition among charge, spin, orbital, and lattice degrees of freedom. One of these phenomena is the colossal magnetoresistance (CMR).[1,2,3] The perovskite $La_{1-x}Sr_xMnO_3$ have been actively studied in the past, and $La_{1-x}Sr_xMnO_3$ crystals became the model object for the investigations of CMR.[4,5,6,7,8,9,10] Recent study[11] of anomalous magnetoelectric and magnetocapacitive effects in $RMnO_3$ (where *R*=rare-earth ion) type manganites renewed interest in these materials. While the quest for magnetocapacitive materials has mostly focused on insulating multiferroic materials,[11,,12] it thought be possible to induce such effects through

manipulation of intrinsic electronic inhomogeneity, which is often observed in doped manganites.[13] In order to prove this, an extensive investigation was done on dielectric properties and the magnetocapacitance effect in a single crystal of the manganite $La_{0.875}Sr_{0.125}MnO_3$.[14,15]

$La_{0.875}Sr_{0.125}MnO_3$ has a complex behavior and undergoes numerous transitions when cooled.[6–10] At $T_{RO} \approx 450$ K a rhombohedral to weakly distorted orthorhombic (*O*) structural phase transition occurs. At temperature $T_{JT} \approx 270$ K, structural transition from a weakly distorted orthorhombic phase to a strongly distorted Jahn-Teller orthorhombic (*O'*) phase takes place. Magnetism sets in at $T_{CA} \approx 180$ K, but the exact nature of the magnetic order is still not determined [5–10] and will be discussed later. Below $T_P \approx 140$ K the system turns into an insulating ferromagnet and displays orbital ordering in the orthorhombic (*O''*) phase.[6,10] This phase's behavior is still unclear and researched actively.[3,6,10]

Furthermore, the $La_{1-x}Sr_xMnO_3$ compound set exhibits a very complex phase diagram, especially at a low Sr doping.[3] Moreover, the experimental evidence for electronic inhomogeneity in manganites is overwhelming.[3,9,16,17,18] These inhomogeneities show up even beyond the Curie temperature. That is why a new temperature scale, *T** should be introduced, similar to the case of high temperature superconductors.[3] Below *T** the metallic domains start forming and percolate, which leads to long-range order as well as CMR effect. In the experiments carried out in this chapter, an attempt for characterizing *T** was made in the regime where the percolation is incomplete. The low-frequency dielectric properties of doped manganites have been under heavy study lately.[19,20,21] In some of these works, two-point probe method was used for dielectric measurements,[19,20]

resulting in contact induced effects.[22] In polycrystalline films they found the effect of a barrier-layer capacitor microstructure created during deposition and oxidation of grain-boundary regions. It forms an insulating coating on semiconducting grains.[21] In order to determine the intrinsic dielectric properties of the manganites in this work, the effect of external magnetic field on the low-frequency dielectric response, four-point probe method was used.[14,15]

The low-frequency dielectric and magnetic measurements show indications that charge separation in $La_{0.875}Sr_{0.125}MnO_3$ occurs. It was also found that the dielectric permittivity displays a non-ergodic behavior and is dependent on how the magnetic field is applied and that giant dielectric permittivity up to 10^9 and magnetocapacitance up to 10^4% were observed.

6.2 Experimental Details

The dielectric measurements were done on a good quality right-angled-parallelepiped $La_{0.875}Sr_{0.125}MnO_3$ single crystal with the dimensions of 5.13×5.13×7.50 mm^3. The *c* axis was parallel to the long axis. The magnetic measurements were carried out on cylindrical shaped single crystals with a diameter 2.47 mm and with length 1.77 mm. These crystals were fully characterized in earlier works done by the group providing the crystals.[6,10]

Complex dielectric permittivity data were taken by the four-point probe method on an Agilent 4294A impedance analyzer and a Quantum Design Physical Properties Measurement System 6100 (PPMS 6100) in the temperatures interval of 80–350 K and at frequencies from 10 Hz to 10 MHz. The electric field was applied parallel to the polar *c*

axis. Two electrodes were attached to the square surfaces to apply the ac voltage, and two small electrodes were attached on one of the other surfaces. The small electrodes were separated by 5–3.5 mm. The magnetic measurements were made on a Quantum Design Magnetic Properties Measurement System (MPMS) in the temperatures range of 80–350 K.

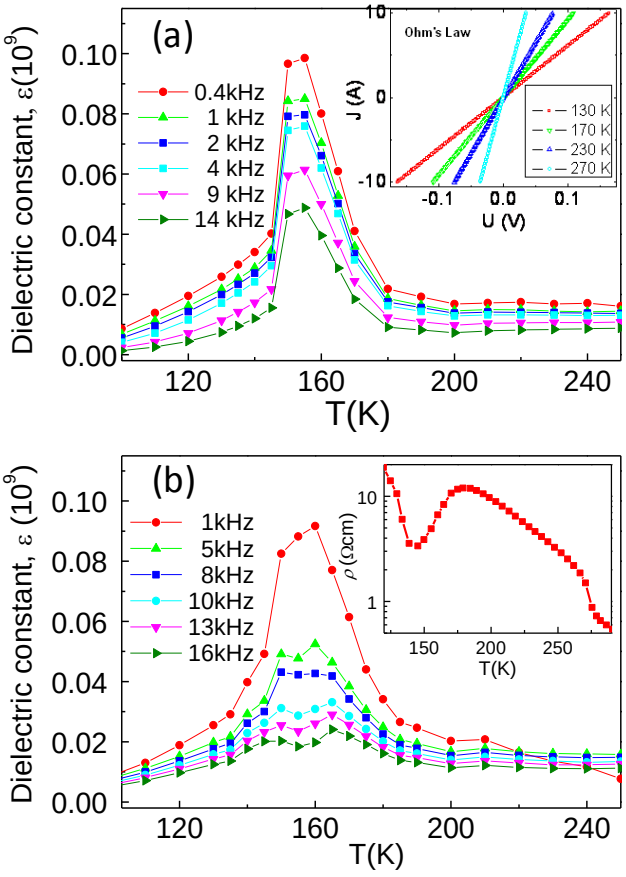

Figure 6-1 Temperature dependence of the dielectric permittivity $\varepsilon(T)$ at different frequencies f at zero external magnetic field: (a) ZFC and (b) ZFHaFC regimes; the insets show the I-V characteristics at 130, 170, 230, and 270 K and the temperature dependence of the dc resistivity, $\rho(T)$. Adopted from Ref. [14].

6.3 Results

The dielectric permittivity as a function of temperature, $\varepsilon(T)$, on cooling without applied magnetic field [zero-field cooled (ZFC)] is shown in Figure 6-1(a) and the same quantity at zero external magnetic field after field cooling in 2T (ZFHaFC) is depicted in Figure 6-1(b). $\varepsilon(T)$ was calculated from the measured capacitance. The inset in Figure 6-1(a) shows the *I-V* characteristics at some temperatures. They indicated good Ohmic contacts.

The temperature dependence of the *dc* resistivity $\rho(T)$ is shown by the inset in Figure 6-1(b). The low-frequency *ac* resistivity coincides with its *dc* resistivity and rises slowly at high frequencies. It was found that for the case of ZFC, $\varepsilon(T)$ increases up to 10^7 below $T \sim 270$ K and does not change much between 180K and 270 K, but it quickly increases below ~ 180 K. It forms a peak at temperature ~ 150 K. It should be noted that the highest value of $\varepsilon(T)$ corresponds to the minimum in the resistivity, as shown in the inset of Figure 6-1(b)). The sudden drop in the dielectric permittivity at T_P is an evidence of the sample's superior quality. Below T_P = 140 K, $\varepsilon(T)$ decreases continuously with temperature. The peak in $\varepsilon(T)$ is somewhat suppressed for the ZFHaFC measurement.

Figure 6-2(a) and (b) show the temperature dependence of $\varepsilon(T)$ upon cooling in an externally applied magnetic field of 4T (field cooled - FC) and upon heating in the same field after field cooling (field heating after field cooling - FHaFC). A minimum was observed in the FC state at a temperature of ~ 165 K (Figure 6-2(a)), while a quite large peak was obtained in the FHaFC process at the same temperature (Figure 6-2(b)).

Without the presence of applied magnetic field, this peak in $\varepsilon(T)$ during FHaFC shows at T_P = 140 K as demonstrated by Figure 6-1(b).

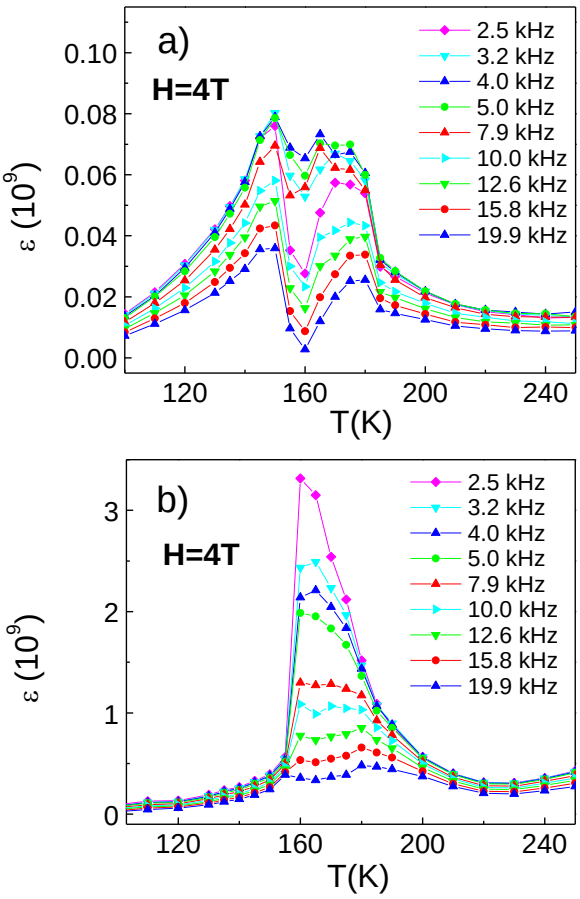

Figure 6-2 Temperature dependence of the dielectric permittivity ε in external field of 4 T: (a) FC and (b) FHaFC regimes [14].

The magnetic field pushes the peak to a higher temperature by a significant rate of $\Delta_H T_p \cong 5$ K per Tesla. $\varepsilon(T)$ at the peak increases rapidly with the increasing magnetic field. Therefore, the magnetocapacitance $\Delta\varepsilon/\varepsilon(0) = [\varepsilon(H) - \varepsilon(0)] / \varepsilon(0)$ at the external

field H = 4 T in the FHaFC state (***H*** || c-axis) shows very large values as shown in Figure 6-3.

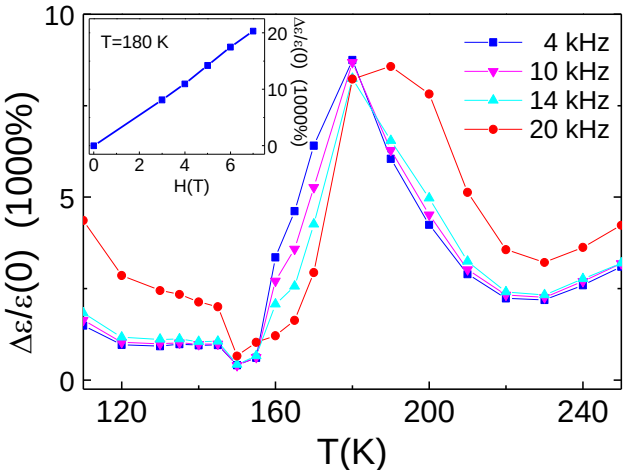

Figure 6-3 Temperature dependence of the magnetocapacitance $\Delta\varepsilon/\varepsilon(0) = [\varepsilon(H) - \varepsilon(0)] / \varepsilon(0)$ at in H=4 T external field, in the heating regime (H || c-axis); the inset shows field dependence of the magnetocapacitance $\Delta\varepsilon/\varepsilon(0)$ at T=180 K. See Ref. [14].

For comparison, the field dependent magnetocapacitance $\Delta\varepsilon/\varepsilon(0)$ is shown in the case of the magnetic field perpendicular to the c axis at T = 180 K (inset of Figure 6-3). It is easy to see that a colossal magnetocapacitance effect is manifested in the $La_{0.875}Sr_{0.125}MnO_3$ single crystal.

Saturation magnetization $M_S(T)$ and magnetic susceptibility $\chi(T)$ are plotted in Figure 6-4. Below about 200 K the magnetization displays a non-linear change with the applied field. The value of $M_S(T)$ was determined by the extrapolated the intercept with H = 0 for the linear portion of the magnetization and $\chi(T)$ was measured by its slope between 1 and 5 T (see the inset in Figure 6-4). The steeply growing magnetization at small magnetic

fields is another piece of evidence of the high quality of the sample. The global maximum in $\chi(T)$ and the rise of $M_S(T)$ signifies a magnetic transition in the vicinity of 200 K. In addition $\chi(T)$ shows small anomalies at the structural phase transition at 270 K. Similar anomalies at 270 K are also observed in *ac* magnetic susceptibility.[23]

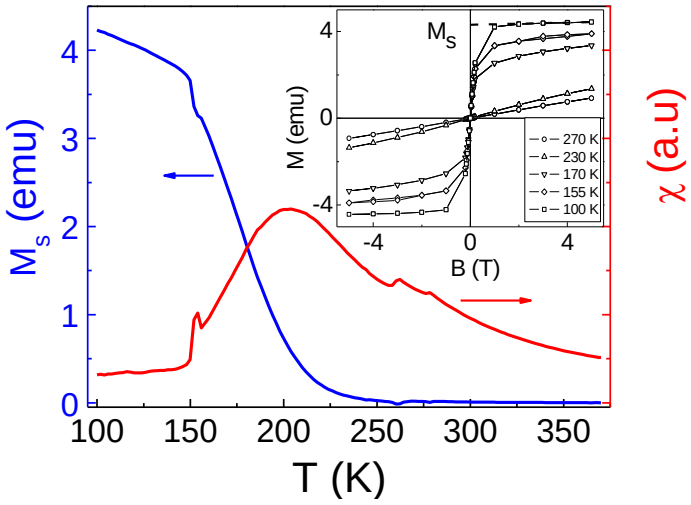

Figure 6-4 Temperature dependence of the saturation spontaneous magnetization *Ms* and of the static magnetic susceptibility (H || *c*-axis); the inset shows the field dependence of the magnetization at different temperatures [14].

6.4 Discussion

The temperature dependent dielectric and magnetic data show that the $La_{0.875}Sr_{0.125}MnO_3$ has large dielectric permittivity and magnetocapacitance below 270 K. These effects are especially pronounced in the temperature range of $140 < T < 185$ K, where the permittivity is strongly dependent on the history of applied magnetic field. The enormous magnetocapacitance and the field hysteretic nature are indication of the strong

interplay between capacitance and magnetism, as well as spin-glass-like behavior in the range of $140 < T < 185$ K. Below T=140 K an antiferromagnetic long-range orbital order sets in, which makes the in-plane superexchange interaction positive following the Goodenough-Kanamori-Anderson rules (see Section 2.2.3.1 for details), thus defining a ferromagnetic insulator, in which charges are localized due to spin polaronic features. In the temperature range of $140 < T < 185$ K, the system is magnetic without orbital order setting in. Thus the superexchange interaction can be positive or negative depending on the mutual orientation of the *d* orbitals on Mn ions, and this is most likely the origin of the spin-glass behavior.

Attempts were made to directly detect the spin-glass behavior by magnetic measurements. However, strong ferromagnetic components made the hysteresis in the susceptibility very weak and the results were inconclusive. But some evidence of spin-glass nature was found in *ac* and *dc* magnetic measurements.[23] According to pulsed neutron pair-density function (PDF) analysis in $La_{0.875}Sr_{0.125}MnO_3$ a doped hole is delocalized over three Mn sites even when it is considered to be localized as polaron.[16] The insulator-to-metal transition occurs at $x = 0.17$ by percolation,[16,24,25,26,27,28] and the $La_{0.875}Sr_{0.125}MnO_3$ studied in this chapter is fairly close to the percolation threshold. Thus holes are not totally confined to a single polaron, and there should be a high density of locally connected filaments or patches of polarons within which holes can move relative easily. This state can be interpreted as the state with nanoscale phase and charge segregation. Since the metallic patches are surrounded by FM or spin-glass insulators, they do not contribute to the *dc* conductivity; however, they do have an influence on the *ac* conductivity, which leads to the high dielectric constant. Thus the giant dielectric

permittivity observed could be called the intrinsic Maxwell-Wagner behavior, because charge dynamics of the metallic areas produce high permittivity. On the $La_{1-x}Sr_xMnO_3$ phase diagram, increasing Sr concentration results in a metallic state with ferromagnetic order. Therefore, regardless of the phase segregation mechanism (such as double-exchange interaction,[29] ferrons,[30] bipolarons,[31] or other models[3,32]), the following may be concluded: Relatively large patches or filaments with multiple holes should be ferromagnetic or superparamagnetic metal. External magnetic field will thus promote the formation of such coagulated holes and will influence the distribution of holes in various ways depending on the topology and geometry of the patches. In this line of argument, it is not difficult to see how the applied magnetic field could modify the dielectric response of the system. It is possible that upon cooling in a high magnetic field, holes coagulate more favorably and form a higher density of ferromagnetic metal than in the case of the zero-field cooling, which increases the dielectric response. This scenario describes the strong magnetocapacitance effect in this system.

These observations suggest that the charge segregation happens at temperature below 270 K, where the structural transition from a weakly distorted orthorhombic (pseudo-cubic) phase to the strongly distorted Jahn-Teller orthorhombic phase occurs. An extra increment of the resistivity below 270 K could be modeled by the charge segregation. In fact the resistivity is expected to increase when charge segregation sets in without percolation of metallic areas. Thus it lowers conductivity, as shown in the inset of Figure 6-1(b) and increases the dielectric response. It should be pointed out that the extreme dielectric permittivity measured could also show up due to interfacial polarization and an external Maxwell-Wagner relaxation process.[22] Particularly, within this scenario, the

CMR effect can lead to a high value of magnetocapacitance coefficient.[33] However, there are numerous reasons to believe that the giant permittivity is an intrinsic effect rather than caused by the contact areas.

First of all, the temperature dependence of the *ac* resistivity of the sample has weak frequency dependence and the value at low-frequency range agrees with the *dc* resistivity.

The second reason is that very dissimilar values of the dielectric permittivity were measured at different temperatures even when the value of the conductivity is the same (for example, at 135, 160, and 210 K).

Furthermore, the anomalous dielectric permittivity was detected only in a limited temperature range ($T < 270$ K).

The last argument arguing against contact effects in the usage of four-point probe method was used for the measurements. High values of dielectric response were consistent with the thickness of the insulated areas of $\Delta l \approx 1 \sim 20$ nm ($\Delta l \approx A\varepsilon\, l\, /\varepsilon_0$, where ε_0 is the dielectric permittivity in the absence of the charge separation, $\varepsilon_0 = 60$; A is the unknown coefficient, which takes into account that we have a series of capacitances and the real surface of the metallic region is larger than the sample cross section).

This estimate is also consistent with the characteristic dispersion frequency ($\omega_0 \sim 10^4$–10^5 Hz). Assuming dynamic Maxwell- Wagner (MW) effect, the characteristic frequency can be calculated by $\omega_{MW} = 1/RC$ (in this case $R = 1\ \Omega$, C=10^{-4}–10^5 F). As a result, the low-frequency response of the dielectric properties is consistent with the charge dynamics of nano-regions. Nevertheless, it is hard to explain such an extreme dielectric permittivity value by only the presence of thin insulated areas; their number should be

large, which would suppress the effect. Therefore, it is unavoidable to take into account the dynamics of metallic domains and their weak interaction with the lattice. Thus, if the motion of the charged metallic regions was considered as a hole in an external electric field, it should help to explain extremely high values of dielectric permittivity. However, further calculations are needed before drawing any final conclusion about the effectiveness of such a mechanism.

6.5 Conclusions

The temperature dependence of the dielectric and magnetic properties of the $La_{0.875}Sr_{0.125}MnO_3$ single crystals were studied in a broad temperature range and applied magnetic field. An anomalous dielectric permittivity was observed below 270 K. The features of these properties are explained by the nanoscale dynamic electronic inhomogeneities in the pre-percolation regime of charge ordering. The external magnetic field effectively modifies the charge segregation leading to the colossal magnetocapacitance effect. These results can be modeled by spin and charge inhomogeneities and their coupling in doped manganites. Even though contact effects seem unlikely, the question if intrinsic Maxwell-Wagner effect, segregated charge dynamics or both of them causes the measured giant dielectric permittivity remains to be further studied.

References

[1] S. Jin, T. H. Tiefel, M. McCormack, R. A. Fastnacht, R. Ramesh,and L. H. Chen, Science 264, 413 (1994).

[2] Y. Tokura and N. Nagaosa, Science 288, 462 (2000).

[3] E. Dagotto, T. Hotta, and A. Moreo, Phys. Rep. 344, 1 (2001).

[4] A. Urushibura, Y. Moritomo, T. Arima, A. Asamitsu, G. Kido,and Y. Tokura, Phys. Rev. B 51, 14103 (1995).

[5] Y. Moritomo, A. Asamitsu, and Y. Tokura, Phys. Rev. B 56, 12190 (1997).

[6] V. Yu. Ivanov, V. D. Travkin, A. A. Mukhin, S. P. Lebedev, A. A. Volkov, A. Pimenov, A. Loidl, A. M. Balbashov, and A. V. Mozhaev, J. Appl. Phys. 83, 7180 (1998); M. Paraskevopoulos, F. Mayr, C. Hartinger, A. Pimenov, J. Hemberger, P. Lunkenheimer, A. Loidl, A. A. Mukhin, V. Yu. Ivanov, and A. M. Balbashov, J. Magn. Magn. Mater. 211, 118 (2000).

[7] H. Kawano, R. Kajimoto, M. Kubota, and H. Yoshizawa, Phys.Rev. B 53, R14709 (1996).

[8] Y. Yamada, O. Hino, S. Nohdo, R. Kanao, T. Inami, and S. Katano,Phys. Rev. Lett. 77, 904 (1996).

[9] Y. Endoh, K. Hirota, S. Ishihara, S. Okamoto, Y. Murakami, A. Nishizawa, T. Fukuda, H. Kimura, H. Nojiri, K. Kaneko, and S. Maekawa, Phys. Rev. Lett. 82, 4328 (1999).

[10] F. Mayr, C. Hartinger M. Paraskevopoulos, A. Pimenov, J. Hemberger, A. Loidl, A. A. Mukhin, and A. M. Balbashov, Phys. Rev. B 62, 15673 (2000).

[11] T. Kimura et al., Nature London 426, 55 (2003);T. Goto, T. Kimura, G. Lawes, A. P. Ramirez, and Y. Tokura, ibid. 92, 257201 (2004).

[12] S. Weber, P. Lunkenheimer, R. Fichtl, J. Hemberger, V. Tsurkan,and A. Loidl, Phys. Rev. Lett. 96, 157202 (2006).

[13] A. L. Efros and B. I. Shklovskii, Phys. Status Solidi B 76, 475 (1976).

[14] R. F. Mamin, T. Egami, Z Marton and S. A. Migachev, Phys. Rev. B **75**(11), 115129 (2007).

[15] R. F. Mamin, T. Egami, Z Marton and S. A. Migachev, Ferroelectrics, **348**, 409 (2007).

[16] D. Louca, T. Egami, E. L. Brosha, H. Röder, and A. R. Bishop, Phys. Rev. B 56, R8475 (1997).

[17] R. V. Demin, L. I. Koroleva, and A. M. Balbashov, JETP Lett. 70, 314 (1999).

[18] J. Deisenhofer, D. Braak, H.-A. Krug von Nidda, J. Hemberger, R. M. Eremina, V. A. Ivanshin, A. M. Balbashov, G. Jug, A. Loidl, T. Kimura, and Y. Tokura, Phys. Rev. Lett. 95, 257202 (2005).

[19] N. Biskup, A. de Andres, J. L. Martinez, and C. Perca, Phys. Rev. B 72, 024115 (2005).

[20] M. P. Gutiérrez, J. Mira, and J. Rivas, Phys. Lett. A 323, 473 (2004).

[21] J. L. Cohn, M. Peterca, and J. J. Neumeier, J. Appl. Phys. 97, 034102 (2005).

[22] P. Lunkenheimer, V. Bobnar, A. V. Pronin, A. I. Ritus, A. A. Volkov, and A. Loidl, Phys. Rev. B 66, 052105 (2002). P. Lunkenheimer, R. Fichtl, S. G. Ebbinghaus, and A. Loidl, ibid. 70, 172102 (2004).

[23] J. Nogues, V. Skumkyev, J. S. Munoz, B. Martinez, J. Fontcuberta, L. Pinsard, and A. Revcolevschi, Phys. Rev. B 64, 024434 (2001); B. Martinez, V. Laukhin, J. Fontcuberta,

J. Nogues, V. Skumryev, J. S. Munoz, L. Pinsard, and A. Revcolevschi, J.Appl. Phys. 89, 6633 (2001).

[24] S. Yunoki, J. Hu, A. L. Malvezzi, A. Moreo, N. Furukawa, and E. Dagotto, Phys. Rev. Lett. 80, 845 (1998).

[25] S. Yunoki, A. Moreo, and E. Dagotto, Phys. Rev. Lett. 81, 5612 (1998).

[26] M. Mayr, A. Moreo, J. A. Vergés, J. Arispe, A. Feiguin, and E. Dagotto, Phys. Rev. Lett. 86, 135 (2001).

[27] T. Egami, in Structure and Bonding edited by J. B. Goodenough (Springer-Verlag, Berlin, 2001), Vol. 98, p. 115.

[28] M. Yu. Kagan and K. I. Kugel, Phys. Usp. 44, 553 (2001).

[29] C. Zener, Phys. Rev. B 82, 403 (1951).

[30] E. L. Nagaev, Phys. Rev. B 60, R6984 (1999).

[31] A. S. Alexandrov, A. M. Bratkovsky, and V. V. Kabanov, Phys. Rev. Lett. 96, 117003 (2006).

[32] A. J. Millis, P. B. Littlewood, and B. I. Shraiman, Phys. Rev. Lett. 74, 5144 (1995).

[33] G. Catalan, Appl. Phys. Lett. 88, 102902 (2006).

7. Conclusions

Chemically doped, perovskite rare earth manganites exhibit numerous electronic and magnetic phases. These phases seem to organize, coexist and compete in the form of nano to micron scale domains. This phase separation picture is getting more and more attention and various experimental results can be explained by assuming electronic inhomogeneities in complex oxides. Such phenomena are the colossal magnetoresistance in certain manganites, or high temperature superconductivity observed in several cuprates.

The first part of my research was growing these materials in a thin film form by pulsed laser deposition technique and incorporating them in functional field-effect devices, which could be useful, on the one hand, in materials research. The large number of coupled phases, these manganites exhibit, can be mapped by chemical doping; however the synthesis of new compositions is fairly time consuming and means only a handful discrete set of points on a phase diagram. Field effect structures with manganite channels can be utilized to dope manganites without creating chemical disorder and to explore a whole range of the phase diagram a quasi-continuous way. On the other hand, this approach is also implementable into prospective semiconductor technology, whose central attention is interfacial charge carrier modulation.

The perovskite oxide thin films and heterostructures were deposited by pulsed laser epitaxy method. After carefully studying the correlation between structural, magnetic and optical properties and growth parameters through the example of $LaMnO_3$, I was aiming at demonstrating field effect in high charge carrier density epitaxial thins films of doped

manganites. The short screening length of a couple of unit cells made it a challenging task. Using highly polar $Pb(Zr_{0.2}Ti_{0.8})O_3$ (PZT) with remnant polarization of about $80\mu C/cm^2$, however, I succeeded in showing large modification of the electronic and magnetic properties of $La_{1-x}Sr_xMnO_3$ (LSMO) probably due to the penetrating electrostatic polarization field, which influenced the interface.

This technique can be used in the future to induce phase transitions in high temperature superconductors, such as $La_{1-x}Sr_xCuO_4$. Their charge carrier density is comparable to that of manganites and the field effect may result in even higher on/off ratio due to prospective switching between metallic and superconducting phases at low temperature.

Certain superlattices also display anomalous interfacial behaviors depending on periodicity and the thickness of the building layers. One of the most intriguing and studied is the $LaAlO_3/SrTiO_3$ systems, which can be insulating, metallic or even superconducting. Optical studies found multiple carriers being responsible for these emerging phenomena on the heterointerface. To study the nature and the tunability of those carriers would be a perfect platform to further demonstrate the power of ferroelectric field effect as materials research tool.

The second part of my research was a contribution to the electronic phase separation picture by studying magnetocapacitance in single crystalline $La_{7/8}Sr_{1/8}MnO_3$. This insulating composition can be imagined, in the frame work of phase separation, as ferromagnetic metallic domains dispersed in a non-conducting matrix. The purpose of this research was to see, if the intrinsic ferromagnetic domain structure can be manipulated by applied magnetic field and can be used to enhance the dielectric response.

Eventually a huge magnetocapacitive effect was demonstrated. It also shed some light on the fundamental nature of phase transitions in these strongly correlated materials.

Later other compositions of single crystals and thin films of correlated and phase separated manganites can be studied with the same technique. It would be interesting to see how other factors like strain and thickness impact the magnetocapacitance once it is shown in such systems.